TRABAJO FIN DE GRADO

Grado en Ingeniería Electrónica Industrial

UNIVERSIDAD DE ALMERIA

ESCUELA SUPERIOR DE INGENIERÍA

Advanced control techniques for industrial overhead cranes

Curso 2016/2017

Alumno/a:

Marco Giacomelli

Director/es:

Dr. D. Antonio Visioli

Dr. D. Manuel Berenguel Soria

UNIVERSIDAD DE ALMERÍA
Escuela Superior de Ingeniería

Trabajo Fin de Grado
Ingeniería Electrónica Industrial

UNIVERSITÀ DEGLI STUDI DI BRESCIA
Dipartimento di Ingegneria Meccanica Industriale
Corso di Laurea Magistrale in Ingegneria dell'Automazione Industriale

ADVANCED CONTROL TECHNIQUES FOR INDUSTRIAL OVERHEAD CRANES

Técnicas de control avanzadas para grúas industriales

Doble Título UNIBS-UAL
Mechatronics for Industrial Automation

Autor: Marco Giacomelli

Director: Dr. D. Antonio Visioli
Codirector: Dr. D. Manuel Berenguel Soria

Almería (España), Diciembre 2017
Curso 2016-2017

Contents

Introduction

One of the main problem when facing motion control, and in control in general, is the presence of undesired oscillations. These oscillations, which characterize every mechanical system, leads to problems like error in positioning and difficulty in controlling the sway.

In this thesis, the problem of oscillations is addressed using a very diffused industrial system for which oscillations are the leading problem: the overhead crane.

This system, presenting the same configuration of a pendulum, is characterized by oscillations with very low damping ratios. The presence of this persistent oscillation during and after the movement makes difficult the manual control, decreases the accuracy and increases the overall positioning time. Moreover, considering the fact that most of the payloads moved by gantry cranes are heavy, a safety hazard is posed by payload pendulation, in particular in cluttered workspaces.

Various advanced control techniques have been proposed to reduce the presence of residual oscillations on industrial cranes, and most of them can be applied to general oscillating systems.

The aim of this thesis is to devise new techniques and to discuss their applicability with industrial off-the-shelf components, focusing in particular on input-output inversion-based techniques and comparing them with the well known input-shaping ones, also investigating their applicability in industrial processes. The importance of an accurate model is also addressed, comparing the results obtained with a simple pendulum model of the overhead crane and with a more complex double pendulum model. For example, the technique of dynamic inversion for industrial crane modelled with the double pendulum model is here presented for the first time.

In Chapter 1, a review of the available techniques for the control of industrial cranes will be presented. In Chapter 2, both simple and double pendulum models are derived, along with the analytical form of natural frequencies and dampenings necessary for the implementation of Input Shaping technique. In Chapter 3 the Input Shaping techniques formulation is presented, paying particular attention to robust IS techniques. In Chapter 4 an input-output inversion technique is presented for both simple and double pendulum models of the crane. In Chapter 5 simulations are made using Simscape™ Multibody™ in order to test the performance of both input shaping and dynamic inversion techniques in terms of residual oscillations reduction and robustness. The differences in the results using simple and double pendulum models are also investigated through simulations. In Chapter 6 the setup of the physical system on which the techniques have been tested is presented, and in Chapter 7 it is explained how the techniques discussed have been implemented on off-the-shelf industrial components. In Chapter 8 the results obtained on the physical system are presented. Finally, in Chapter 8.3 the results obtained through simulations and with the physical system are analyzed.

Chapter 1

Review of existing control techniques

In this chapter a review of the existing control techniques for gantry cranes is presented. For a complete review of the techniques not described below, refer to [2] and [12]. All the techniques described below take into account planar movements of gantry cranes and inertial forces only. Control techniques for gantry cranes can be divided in two main categories: Open-Loop and Closed-Loop techniques.

1.1 Open-Loop techniques

The main advantage of open-loop techniques is the fact that no sensor is needed to check the state of the system. As gantry cranes are industrial MHS (Materials Handling Systems), it is unlikely to find sensors already mounted on the crane, and this is why most of the industrial cranes use open-loop techniques for the reduction of residual oscillations. A limit to open-loop techniques is that they rely only on the model of the system, and they are consequently very sensitive to variations in parameter values about nominal values and to variations in initial conditions and external disturbances. Also, they usually rely on linearized models of the crane, and the uncertainties introduced with the process of modellization and the linearization introduce residual oscillations that cannot be compensated. Moreover, input shaping

and input-output inversion are based on models that consider a constant length of the cable, therefore their performance degrades when horizontal movements and hoisting are combined at the same time.

Input Shaping

The most widely used open-loop technique for residual oscillation reduction is Input Shaping. The reason for this diffusion is the simplicity of the technique, as it requires only a basic modelling of the crane, consisting in the measure of the natural pulses ω_n and damping ratios ξ of the crane, values that are easy to be measured. The controller accelerates the crane in steps of constant acceleration, and compensates for the oscillation when the sway angle reaches 0. The payload then keeps constant velocity without oscillation until the final position, and the same acceleration profile is used to decelerate the crane in order to obtain zero residual oscillation. The technique can be easily extended to systems with multiple modes, like in the case of double-pendulum like overhead cranes, as reported in [30].

The main drawback of input shaping techniques is the high value of the minimum time required, that has to be greater than half of the period of the system.

Optimal Control

Optimal control is a model based technique that calculates the inputs in order to guarantee optimality over parameters like hoisting time and travel time while avoiding obstacles along the path. The first attempts of using optimal control on gantry cranes did not address the problem of residual oscillations [8],[5]. [4] a minimization of both residual sway and final time is considered, but the measurement of the states of the crane is required.

Input Output Inversion

An innovative approach to overhead cranes control is represented by input-output inversion control . The method is based on the transfer function from the force applied to the cart (or the position of the cart) to the position of the payload. A desired trajectory of the payload is then defined, by satisfying

some constraints on the order of continuity. The transfer function is then inverted, and the input corresponding to the desired payload trajectory is defined. A limit of this approach is that it is not possible to impose constraints on the input (e.g. limit the acceleration or maximum velocity of the cart), problem that has been solved in [21] using a the bisection method to find the optimal duration of the movement that satisfies actuators limits.

1.2 Closed-Loop techniques

Closed-Loop techniques , with respect to Open-Loop techniques, have the advantage of being more robust with respect to model parameters errors. While errors in open-loop techniques inevitably bring to residual oscillations that cannot be compensated, Closed-Loop techniques can counteract the insurgence of residual oscillations, guaranteeing for most of the cases a steady state with no residual oscillations at all. The drawback of Closed-Loop techniques is that they require a feedback of the states of the system, which requires the presence of sensors to measure the oscillations of the crane. The presence of this kind of sensors is not common on industrial cranes, therefore the use of Closed-Loop techniques, for most of the cases, require an *ad hoc* hardware setup.

Linear Control

Linear Control has been the first feedback approach to the control of residual oscillation of the crane. The system is usually modelled as a simple pendulum, so that the oscillation is fully described by the evolution of the angle between the vertical and the rope. The angle of oscillation is measured and a linear controller compensate the oscillations. Feedback control of the oscillations can lead to errors in the correct positioning of the payload. Various solutions for this problem have been proposed, like the one in [18] where, to bring the payload to a stop, the trolley decelerates in two stages. The first deceleration stage is a part of the feedback control phase, to suppress oscillations. The second deceleration stage is an input shaping technique used to bring the load to rest over the target point. In [15] a strategy composed of

a PI controller to track the trolley position and a PD controller to dampen the payload oscillations using the motion of the trolley.

Adaptive Control

Adaptive control techniques have been proposed for the feedback control of cranes oscillations. In particular, gain-sheculing techniques have been developed in order to take into account the different operative states of the crane. In particular, in [3] a robust gain-scheduling technique is proposed in order to compensate the oscillations in emergency situations. In [17, 27, 34] a gain-scheduling technique is used to compensate oscillations while explicitly taking into consideration the variable length of the cable.

Fuzzy Logic Control

Fuzzy logic is widely used in machine control. Its main advantage with respect to other alternative control strategies is that the solution to the problem can be cast in terms that human operators can understand, using words instead of numbers to describe a solution to be taken in a particular operating condition of the system. This mean that operators experience can be used to automatize tasks that are already well performed by humans. Fuzzy logic control has been applied to the control of overhead cranes. In [19, 36, 37] a predictive fuzzy control strategy to minimize payload oscillations and travel time is proposed, while moving towards a target point and maneuvering to avoid obstacles along the paths. The strategy breaks the crane operation into seven stages and decides which fuzzy control rule to use in each of them, based on simplified models of the trolley and payload motion. Fuzzy logic strategies are specially difficult to tune. The control input is either too high, which produces cycles of overshoot-undershoot around the target point, or too low, which produces a very slow and time-consuming approach to the target point, increasing operating costs. Furthermore, all strategies in the literature restrict crane operation to a pre-defined path [2].

Model Predictive Control

Thanks to the increasing computational power of modern CPUs in the last years it has been possible to apply Model Predictive Control (MPC) for the control of systems with relative rapid dynamics, like overhead cranes. This techniques is based on the calculation of the input signal by optimizing a cost function respecting the limits imposed by the model of the system and by the actuators. The cost function takes into account, with different weights that have to be set, the contribute of oscillations, transient time and energy cost. The tune of the weights of the different components of the cost function is crucial. Unlike optimal control, the optimization process takes place at every cycle of the control system, and only the first value of the input vector calculated is actually given to the system. On the next control cycle, the initial conditions are updated with the measured states of the system, and the optimization process re-executed. For this reason MPC is robust with respect to errors in model parameters, unlike open-loop techniques like optimal control. Recently, MPC has been applied to the anti-swing control of overhead cranes in [13, 28, 35].

Chapter 2

Model of the crane

In this chapter the models of the crane will be presented. First, the crane will be schematized as a simple pendulum connected with a cart, neglecting the existence of the hook or the presence of a distributed payload. Then the equations for the system schematized as a double pendulum will be written.

From the dynamics equations of the nonlinear models a linear state-space representation will be calculated for both simple and double pendulum models in order to have easy-to-manage tools for control purposes. The response of the linearised models will be analyzed and compared with the nonlinear models in Chapter 5.2.

From the linear model natural frequencies and damping coefficients will then be calculated, as they will be used in order to implement Input Shaping control techniques in Chapter 3.

Finally, from the state space description a series of transfer function will be written for both simple and double pendulum, giving the mathematical tools needed in Chapter 4 for the implementation of input-output inversion techniques.

2.1 Simple pendulum model

An overhead crane, with a first approximation, can be schematized as a single pendulum and a moving cart, as showed in Figure 2.1.

The symbols refer to:

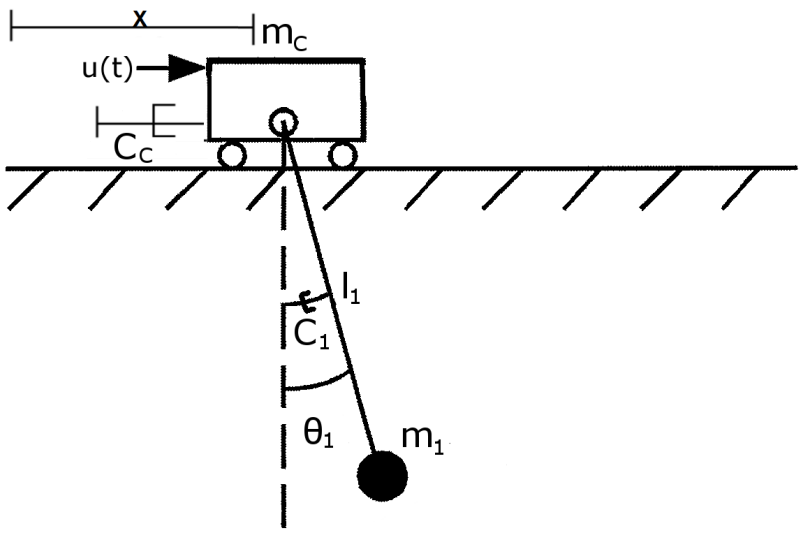

Figure 2.1: Scheme of a overhead crane seen as a simple pendulum connected to a sliding cart. Figure adapted from [24].

$u(t)$: force applied to the cart;

m_C : mass of the cart;

C_C : viscous friction coefficient of the cart;

θ_1 angle between the vertical and the cable; between cart and payload;

C_1 : viscous friction coefficient of the first cable;

l_1 : length of the first cable;

m_1 : mass of the payload.

In this model the hook and the payload are considered as a single mass point. Some other approximations that have to be made to ensure a simple mathematical description of the model are:

- the rope is considered as an inflexible rod;
- compared to the mass of the payload, the mass of the cable can be neglected;

- the system moves only on a $x - y$ plan.

The Lagrangian method can be used to find the differential equations of the system in Figure 2.1.

The potential energy of the system is a function of the position of the payload, that is

$$P = m_1 g l_1 (1 - \cos\theta_1) \tag{2.1}$$

Under the assumption that the payload is a material particle, the kinetic energy of the system is given by

$$K = \frac{1}{2} m_C \dot{x}^2 + \frac{1}{2} m_1 v_1^2 \tag{2.2}$$

where $\dot{x}$ is the velocity of the cart and v_1 is the velocity of the payload, that is

$$v_1^2 = v_{1x}^2 + v_{1y}^2 \tag{2.3}$$

where

$$v_{1x} = \dot{x} + l_1 \dot{\theta_1} \cos(\theta_1) \quad \text{and} \quad v_{1y} = -l_1 \dot{\theta_1} \sin(\theta_1) \tag{2.4}$$

Given (2.1) and (2.2), the Lagrangian of the system is

$$L = K - P = \frac{1}{2} m_C \dot{x}^2 + \frac{1}{2} m_1 l_1 v^2 - m_1 g l_1 (1 - cos(\theta_1)) \tag{2.5}$$

The equations of the system dynamics can be calculated using the Lagrangian method, that states that

$$\frac{d}{dt}\left(\frac{\partial L}{\partial \dot{q}_i}\right) - \frac{\partial L}{\partial q_i} = Q_i \tag{2.6}$$

where q_i, $i = [1...N]$ are the variables that represent the N free way of moving of the system and Q_i is the vector of the generalized external forces, which includes the dissipative forces through Rayleigh dissipation function [9].

The two variables that describe the free ways of moving of the system are x and θ_1. Differentiating L with respect to $\dot{x}$ in (2.5) we find

$$\frac{\partial L}{\partial \dot{x}} = m_C \dot{x} + m_1 (\dot{x} + l_1 \dot{\theta_1} \cos\theta_1) \tag{2.7}$$

Differentiating (2.7) with respect to time t yields

$$\frac{d}{dt}\left(\frac{\partial L}{\partial \dot{x}}\right) = m_C\ddot{x} + m_1(\ddot{x} + l_1\ddot{\theta_1}\cos\theta_1 - l_1\dot{\theta_1}^2\sin\theta_1) \tag{2.8}$$

The potential energy of the system does not depend on x, therefore we have

$$\frac{\partial L}{\partial x} = 0 \tag{2.9}$$

The generalized external forces for the variable x depend on the external force $u(t)$ and the frictional force, thus

$$Q_x = u(t) - C_C\dot{x} \tag{2.10}$$

In the same way, differentiating (2.5) with respect to $\dot{\theta_1}\theta_1$ yields

$$\begin{aligned}\frac{\partial L}{\partial \theta_1} &= m_1[(\dot{x} + l_1\cos\theta_1)l_1\cos\theta_1 + (-l_1\dot{\theta_1}\sin\theta_1)(-l_1\dot{\theta_1}\sin\theta_1)] \\ &= m_1l_1\dot{x}\cos\theta_1 + m_1l_1^2\dot{\theta_1}\end{aligned} \tag{2.11}$$

and differentiating (2.11) with respect to time we obtain

$$\frac{d}{dt}\left(\frac{\partial L}{\partial \theta_1}\right) = m_1l_1\ddot{x}\cos\theta_1 - m_1l_1\dot{x}\dot{\theta_1}\sin\theta_1 + m_1l_1^2\ddot{\theta_1} \tag{2.12}$$

Further, differentiating (2.5) with respect to θ_1 can have

$$\begin{aligned}\frac{\partial L}{\partial \theta_1} &= m_1[(\dot{x} + l_1\dot{\theta_1}\cos\theta_1)(-l_1\sin\theta_1) + (l_1\dot{\theta_1}\sin\theta_1)(l_1\dot{\theta_1}\cos\theta_1)] - m_1gl_1\sin\theta_1 \\ &= -m_1l_1\dot{x}\dot{\theta_1}\sin\theta_1 - m_1gl_1\sin\theta_1\end{aligned} \tag{2.13}$$

Finally, generalized external forces for the variable θ_1 depends on the frictional force, thus

$$Q_{\theta_1} = -\frac{C_1}{l_1}\dot{\theta_1} \tag{2.14}$$

Considering (2.8), (2.9) and (2.10) and (2.12), (2.13) and(2.14), from (2.6) the two equations that describe the dynamics of the system are

$$\begin{cases}(m_1 + m_C)\ddot{x} + m_1l_1(\ddot{\theta_1}\cos\theta_1 - \dot{\theta_1}^2\sin\theta_1) = u(t) - C_C\dot{x} \\ m_1\ddot{x}\cos\theta_1 + m_1l_1\ddot{\theta_1} + m_1g\sin\theta_1 = -\dfrac{C_1}{l_1}\dot{\theta_1}\end{cases} \tag{2.15}$$

2.1.1 Linearized single pendulum model

The model can now be linearized around its sole stable equilibrium point, that is for $\theta_1 = 0$. With the approximations

$$\begin{aligned} \cos\theta_1 &= 1 \\ \sin\theta_1 &= \theta_1 \\ \dot{\theta_1}^2 &= 0 \end{aligned} \tag{2.16}$$

(2.15) become

$$\begin{cases} (m_1 + m_C)\ddot{x} + m_1 l_1 \ddot{\theta_1} + C_C \dot{x} = u(t) \\ m_1 \ddot{x} + m_1 l_1 \ddot{\theta_1} + \dfrac{C_1}{l_1}\dot{\theta_1} + m_1 g \theta_1 = 0 \end{cases} \tag{2.17}$$

Finally, equation (2.17) can be rearranged in a matrix form that is well known for mechanical systems as

$$\mathcal{M}\ddot{\boldsymbol{x}} + \mathcal{C}\dot{\boldsymbol{x}} + \mathcal{K}\boldsymbol{x} = \boldsymbol{F} \tag{2.18}$$

where

$$\mathcal{M} = \begin{pmatrix} m_1 + m_C & m_1 l_1 \\ m_1 & m_1 l_1 \end{pmatrix}, \mathcal{C} = \begin{pmatrix} C_C & 0 \\ 0 & \dfrac{C_1}{l_1} \end{pmatrix}, \mathcal{K} = \begin{pmatrix} 0 & 0 \\ 0 & m_1 g \end{pmatrix} \tag{2.19}$$

while

$$\boldsymbol{x} = \begin{pmatrix} x \\ \theta_1 \end{pmatrix}, \boldsymbol{F} = \begin{pmatrix} u(t) \\ 0 \end{pmatrix} \tag{2.20}$$

2.1.2 Linearized state-space representation

Defining

$$\boldsymbol{x_{ss}} = \begin{pmatrix} x \\ \dot{x} \\ \theta_1 \\ \dot{\theta_1} \end{pmatrix} \tag{2.21}$$

the state-space representation of the system (2.18) is in the form

$$\begin{cases} \dot{\boldsymbol{x}}_{\boldsymbol{ss}}(t) = \mathcal{A}\boldsymbol{x}_{\boldsymbol{ss}}(t) + \mathcal{B}u(t) \\ \boldsymbol{y}(t) = \mathcal{C}\boldsymbol{x}_{\boldsymbol{ss}}(t), \end{cases} \tag{2.22}$$

with

$$\mathcal{A} = \begin{pmatrix} 0 & 1 & 0 & 0 \\ 0 & -\dfrac{C_C}{m_C} & \dfrac{gm_1}{m_C} & \dfrac{C_1}{m_C} \\ 0 & 0 & 0 & 1 \\ 0 & \dfrac{C_C}{l_1 m_C} & -\dfrac{g(m_1+m_C)}{l_1 m_C} & -\dfrac{C_1(m_1+m_C)}{l_1^2 m_1 m_C} \end{pmatrix} \tag{2.23}$$

$$\mathcal{B} = \begin{pmatrix} 0 \\ \dfrac{1}{m_C} \\ 0 \\ -\dfrac{1}{l_1 m_C} \end{pmatrix} \tag{2.24}$$

The output of the system is the position of the payload, that is given by

$$x_p = x + l_1 \sin\theta \tag{2.25}$$

With the approximation $\sin\theta = \theta$ and (2.25) the matrix $\mathcal{C}$ in (2.22) is

$$\mathcal{C} = \begin{pmatrix} 1 & 0 & l_1 & 0 \end{pmatrix} \tag{2.26}$$

2.2 Double pendulum model

For an overhead crane carrying a payload with a hook with not negligible mass connected to the payload by mean of a cable of a certain length, a model based on the simple pendulum in Figure 2.1 could be not appropriate for control purposes. Another situation for which the simple pendulum is not sufficient is the case of distributed mass payloads, for which the simplification of the payload as a single mass point hides the presence of a second way of vibrating of the system.

A system like the one just described can be schematized as the double pendulum on a cart in Figure 2.2. The symbols in Figure 2.2 have the same meaning of the simple pendulum model, except for:

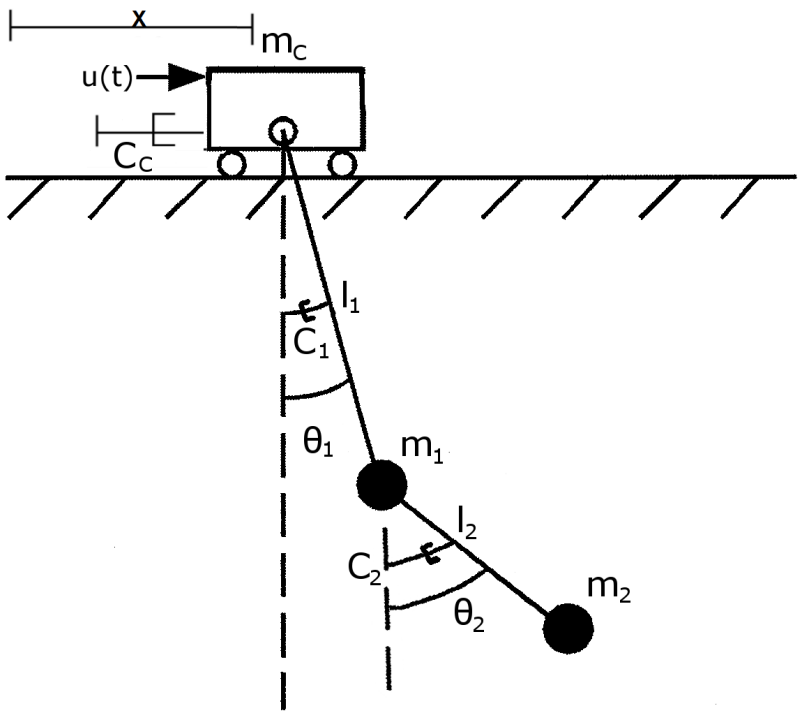

Figure 2.2: Scheme of an overhead crane, seen as a double pendulum connected to a sliding cart. Figure adapted from [24].

m_1: mass of the hook;

θ_2: angle between the vertical and the cable between hook and payload;

C_2: viscous friction coefficient of the second cable;

l_2: length of the second cable;

m_2: mass of the payload.

Following the same scheme of the simple pendulum case, the potential energy of the system is

$$P = m_1 g l_1(1 - \cos\theta_1) + m_2 g[l_2(1 - \cos\theta_2) + l_1(1 - \cos\theta_1)] \tag{2.27}$$

while the kinetic energy is given by

$$K = \frac{1}{2} m_C \dot{x}^2 + \frac{1}{2} m_1 v_1^2 + \frac{1}{2} m_2 v_2^2 \tag{2.28}$$

where $\dot{x}$ is the velocity of the cart, v_1 is the velocity of the hook, that is,

$$v_1^2 = v_{1x}^2 + v_{1y}^2 \tag{2.29}$$

where

$$v_{1x} = \dot{x} + l_1\dot{\theta}_1 \cos(\theta_1) \quad \text{and} \quad v_{1y} = -l_1\dot{\theta}_1 \sin(\theta_1) \tag{2.30}$$

and v_2 is the velocity of the payload, that is

$$v_1^2 = v_{2x}^2 + v_{2y}^2 \tag{2.31}$$

where

$$\begin{aligned} v_{2x} &= \dot{x} + l_1\dot{\theta}_1 \cos(\theta_1) + l_2\dot{\theta}_2 \cos\theta_2 \\ v_{1y} &= -l_1\dot{\theta}_1 \sin(\theta_1) - l_2\dot{\theta}_2 \sin\theta_2 \end{aligned} \tag{2.32}$$

The Lagrangian of the system therefore is

$$\begin{aligned} L = K - P = &\frac{1}{2} m_C \dot{x}^2 + \frac{1}{2} m_1 v_1^2 + \frac{1}{2} m_2 v_2^2 - m_1 g l_1(1 - \cos\theta_1) \\ &- m_2 g[l_2(1 - \cos\theta_2) - l_1(1 - \cos\theta_1)] \end{aligned} \tag{2.33}$$

The three variables that describes the kinematic of the system are x, θ_1 and θ_2. The Lagrangian of the system does not depend on the position of the cart, thus

$$\frac{\partial L}{\partial x} = 0 \tag{2.34}$$

Differentiating (2.33) with respect to $\dot{x}$ yields

$$\frac{\partial L}{\partial \dot{x}} = (m_C + m_1 + m_2)\ddot{x} + (m_1 + m_2)l_1\dot{\theta}_1 \cos\theta_1 + m_2 l_2 \dot{\theta}_2 \cos\theta_2 \tag{2.35}$$

and, further differentiating with respect to time, we have

$$\begin{aligned} \frac{d}{dt}(\frac{\partial L}{\partial \dot{x}}) =& (m_C + m_1 + m_2)\ddot{x} + (m_1 + m_2)l_1\ddot{\theta}_1 \cos\theta_1 \\ & - (m_1 + m_2)l_1 \dot{\theta_1}^2 \sin\theta_1 + m_2 l_2 \ddot{\theta}_2 \cos\theta_2 \\ & - m_2 l_2 \dot{\theta_2}^2 \sin\theta_2 \end{aligned} \tag{2.36}$$

The generalized external forces for the cart are

$$Q_x = u(t) - C_C \dot{x} \tag{2.37}$$

From (2.6), (2.34), (2.36) and (2.37) the first equation of the dynamics of the system is

$$\begin{aligned} & (m_C + m_1 + m_2)\ddot{x} + (m_1 + m_2)l_1\ddot{\theta}_1 \cos\theta_1 + m_2 l_2 \ddot{\theta}_2 \cos\theta_2 \\ & - (m_1 + m_2)l_1 \dot{\theta_1}^2 \sin\theta_1 - m_2 l_2 \dot{\theta_2}^2 \sin\theta_2 = u(t) - C_C \dot{x} \end{aligned} \tag{2.38}$$

Considering now the second variable θ_1, differentiating (2.33) with respect to θ_1 yields

$$\begin{aligned} \frac{\partial L}{\partial \theta_1} =& -(m_1 + m_2)l_1 \dot{x}\dot{\theta}_1 \sin\theta_1 - m_2 l_1 l_2 \dot{\theta}_1 \dot{\theta}_2 \sin(\theta_1 - \theta_2) \\ & - (m_1 + m_2) g l_1 \sin\theta_1 \end{aligned} \tag{2.39}$$

Differentiating (2.33) with respect to $\dot{\theta}_1$ leads to

$$\frac{\partial L}{\partial \dot{\theta}_1} = (m_1 + m_2)(l_1 \dot{x}\cos\theta_1 + l_1^2 \dot{\theta}_1) + m_2 l_1 l_2 \dot{\theta}_2 \cos(\theta_1 - \theta_2) \tag{2.40}$$

and subsequently with respect to time

$$\begin{aligned} \frac{d}{dt}\left(\frac{\partial L}{\partial \dot{\theta}_1}\right) =& (m_1 + m_2)(l_1 \ddot{x}\cos\theta_1 - l_1 \dot{x}\dot{\theta}_1 \cos\theta_1 + l_1^2 \ddot{\theta}_2) \\ & + m_2 l_1 l_2 \ddot{\theta_2}^2 \cos(\theta_1 - \theta_2) - m_2 l_1 l_2 \dot{\theta}_1 \dot{\theta}_2 \sin(\theta_1 - \theta_2) \\ & + m_2 l_1 l_2 \dot{\theta_2}^2 \sin(\theta_1 - \theta_2) \end{aligned} \tag{2.41}$$

The generalized forces for the variable θ_1 are

$$Q_{\theta_1} = -\frac{C_1}{l_1}\dot{\theta}_1 \tag{2.42}$$

From (2.6), (2.39), (2.41) and (2.42) the second equation of the dynamics of the system is

$$\begin{aligned}&(m_1+m_2)l_1\ddot{x}\cos\theta_1 + (m_1+m_2)l_1^2\ddot{\theta_1} + m_2l_1l_2\ddot{\theta}_2 cos(\theta_1-\theta_2)\\&+ m_2l_1l_2\dot{\theta_2}^2\sin(\theta_1-\theta_2) + (m_1+m_2)gl_1\sin\theta_1 = -\frac{C_1}{l_1}\dot{\theta}_1\end{aligned} \tag{2.43}$$

Consider the last variable θ_2. Differentiating (2.33) with respect to θ_2 yields

$$\frac{\partial L}{\partial \theta_2} = -m_2l_1\dot{x}\dot{\theta}_2\sin\theta_2 + m_2l_1l_2\dot{\theta}_1\dot{\theta}_2\sin(\theta_1-\theta_2) - m_2gl_2\sin\theta_2 \tag{2.44}$$

Differentiating (2.33) with respect to $\dot{\theta}_2$ leads to

$$\frac{\partial L}{\partial \dot{\theta}_2} = m_2l_1\dot{x}\cos\theta_1 + m_2l_2^2\dot{\theta}_2 + m_2l_1l_2\dot{\theta}_1\cos(\theta_1-\theta_2) \tag{2.45}$$

and further differentiating with respect to time, we have

$$\begin{aligned}\frac{d}{dt}\left(\frac{\partial L}{\partial \dot{\theta}_2}\right) =& m_2l_2\ddot{x}\cos\theta_2 - m_2l_2\dot{x}\dot{\theta}_2\cos\theta_2 + m_2l_2^2\ddot{\theta}_2\\&+ m_2l_1l_2\ddot{\theta_1}\cos(\theta_1-\theta_2) - m_2l_1l_2\dot{\theta_1}^2\sin(\theta_1-\theta_2)\\&+ m_2l_1l_2\dot{\theta}_1\dot{\theta}_2 sin(\theta_1-\theta_2)\end{aligned} \tag{2.46}$$

The generalized forces for the variable θ_2 are

$$Q_{\theta_2} = -\frac{C_2}{l_2}\dot{\theta}_2 \tag{2.47}$$

From (2.6), (2.44), (2.46) and (2.47) the third equation of the dynamics of the system is

$$\begin{aligned}&m_2l_2\ddot{x}\cos\theta_2 + m_2l_2^2\ddot{\theta}_2 + m_2l_1l_2\ddot{\theta_1}\cos(\theta_1-\theta_2)\\&- m_2l_1l_2\dot{\theta_1}^2\sin(\theta_1-\theta_2) + m_2gl_2\sin\theta_2 = -\frac{C_2}{l_2}\dot{\theta}_2\end{aligned} \tag{2.48}$$

The system of equations composed by (2.38), (2.43) and (2.48) fully describes the dynamic of the system:

$$\begin{cases} (m_C + m_1 + m_2)\ddot{x} + (m_1 + m_2)l_1\ddot{\theta_1}\cos\theta_1 + m_2 l_2\ddot{\theta_2}\cos\theta_2 \\ -(m_1 + m_2)l_1\dot{\theta_1}^2\sin\theta_1 - m_2 l_2\dot{\theta_2}^2\sin\theta_2 = u(t) - C_C\dot{x} \\ (m_1 + m_2)l_1\ddot{x}\cos\theta_1 + (m_1 + m_2)l_1^2\ddot{\theta_1} + m_2 l_1 l_2\ddot{\theta_2}cos(\theta_1 - \theta_2) \\ + m_2 l_1 l_2\dot{\theta_2}^2\sin(\theta_1 - \theta_2) + (m_1 + m_2)gl_1\sin\theta_1 = -\dfrac{C_1}{l_1}\dot{\theta_1} \\ m_2 l_2\ddot{x}\cos\theta_2 + m_2 l_2^2\ddot{\theta_2} + m_2 l_1 l_2\ddot{\theta_1}\cos(\theta_1 - \theta_2) \\ - m_2 l_1 l_2\dot{\theta_1}^2\sin(\theta_1 - \theta_2) + m_2 g l_2\sin\theta_2 = -\dfrac{C_2}{l_2}\dot{\theta_2} \end{cases} \tag{2.49}$$

2.2.1 Linearized double pendulum model

The model can now be linearized around its sole stable equilibrium point, that is for $\theta_1 = 0$ and $\theta_2 = 0$. With the approximations

$$\begin{aligned} \cos\theta_1 = \cos\theta_2 = \cos(\theta_1 - \theta_2) &= 1 \\ \sin\theta_1 &= \theta_1 \\ \sin\theta_2 &= \theta_2 \\ \sin(\theta_1 - \theta_2) &= \theta_1 - \theta_2 \\ \dot{\theta_1}^2 = \dot{\theta_2}^2 &= 0 \end{aligned} \tag{2.50}$$

(2.49) become

$$\begin{cases} (m_C + m_1 + m_2)\ddot{x} + (m_1 + m_2)l_1\ddot{\theta_1} + m_2 l_2\ddot{\theta_2} + C_C\dot{x} = u(t) \\ (m_1 + m_2)l_1\ddot{x} + (m_1 + m_2)l_1^2\ddot{\theta_1} + m_2 l_1 l_2\ddot{\theta_2} + \dfrac{C_1}{l_1}\dot{\theta_1} + (m_1 + m_2)gl_1\theta_1 = 0 \\ m_2 l_2\ddot{x} + m_2 l_1 l_2\ddot{\theta_1} + m_2 l_2^2\ddot{\theta_2} + m_2 g l_2\theta_2 + \dfrac{C_2}{l_2}\dot{\theta_2} = 0 \end{cases} \tag{2.51}$$

The system (2.51) can be written in the form

$$\mathcal{M}\ddot{\boldsymbol{x}} + \mathcal{C}\dot{\boldsymbol{x}} + \mathcal{K}\boldsymbol{x} = \boldsymbol{F} \tag{2.52}$$

where

$$\mathcal{M} = \begin{pmatrix} m_C + m_1 + m_2 & (m_1 + m_2)l_1 & m_2 l_2 \\ (m_1 + m_2)l_1 & (m_1 + m_2)l_1^2 & m_2 l_1 l_2 \\ m_2 l_2 & m_2 l_1 l_2 & m_2 l_2^2 \end{pmatrix}$$

$$\mathcal{C} = \begin{pmatrix} C_C & 0 & 0 \\ 0 & \frac{C_1}{l_1} & 0 \\ 0 & 0 & \frac{C_2}{l_2} \end{pmatrix} \tag{2.53}$$

$$\mathcal{K} = \begin{pmatrix} 0 & 0 & 0 \\ 0 & (m_1 + m_2)gl_1 & 0 \\ 0 & 0 & m_2 g l_2 \end{pmatrix}$$

and

$$\boldsymbol{x} = \begin{pmatrix} x \\ \theta_1 \\ \theta_2 \end{pmatrix}, \boldsymbol{F} = \begin{pmatrix} u(t) \\ 0 \\ 0 \end{pmatrix} \tag{2.54}$$

2.2.2 Linearized state-space representation

Defining

$$\boldsymbol{x_{ss}} = \begin{pmatrix} x \\ \dot{x} \\ \theta_1 \\ \dot{\theta}_1 \\ \theta_2 \\ \dot{\theta}_2 \end{pmatrix} \tag{2.55}$$

the state-space representation of the system (2.51) is in the form

$$\begin{cases} \dot{\boldsymbol{x}}_{\boldsymbol{ss}}(t) = \mathcal{A}\boldsymbol{x}_{\boldsymbol{ss}}(t) + \mathcal{B}u(t) \\ \boldsymbol{y}(t) = \mathcal{C}\boldsymbol{x}_{\boldsymbol{ss}}(t), \end{cases} \tag{2.56}$$

with

$$\mathcal{A} = \begin{pmatrix} 0 & 1 & 0 & 0 & 0 & 0 \\ 0 & -\dfrac{C_C}{m_C} & \dfrac{(m_1+m_2)g}{m_C} & \dfrac{C_1}{l_1^2 m_C} & 0 & 0 \\ 0 & 0 & 0 & 1 & 0 & 0 \\ 0 & \dfrac{C_C}{l_1 m_C} & -\dfrac{g(m_1+m_2)(m_1+m_c)}{l_1 m_1 m_C} & -\dfrac{C_1(m_1+m_C)}{l_1^3 m_1 m_C} & \dfrac{gm_2}{l_1 m_1} & \dfrac{C_2}{l_1 l_2^2 m_1} \\ 0 & 0 & 0 & 0 & 0 & 1 \\ 0 & 0 & \dfrac{g(m_1+m_2)}{l_2 m_1} & \dfrac{C_1}{l_1^2 l_2 m_1} & -\dfrac{g(m_1+m_2)}{l_2 m_1} & -\dfrac{C_2(m_1+m_2)}{l_2^3 m_1 m_2} \end{pmatrix} \tag{2.57}$$

$$\mathcal{B} = \begin{pmatrix} 0 \\ \dfrac{1}{m_C} \\ 0 \\ -\dfrac{1}{l_1 m_C} \\ 0 \\ 0 \end{pmatrix} \tag{2.58}$$

The output of the system is the position of the payload, that is given by

$$x_p = x + l_1 \sin\theta_1 + l_2 \sin\theta_2 \tag{2.59}$$

With the approximation $\sin\theta = \theta$ and (2.59) the matrix $\mathcal{C}$ in (2.56) is

$$\mathcal{C} = \begin{pmatrix} 1 & 0 & l_1 & 0 & l_2 & 0 \end{pmatrix} \tag{2.60}$$

2.2.3 Two-masses equivalent system for rigid body payloads

Even if until this moment the double pendulum has been referred to as a model of a crane where both payload and hook have not negligible mass, it is also a useful model for the study and the control of cranes without hooks but with payloads with not negligible mass moment of inertia. This kind of

payload, in fact, can be modeled for control purposes as a two-masses system. The first mass is positioned on the upper extremity of the payload, where it is attached to the cable, and the other one is opportunely positioned. The number of variables to be found to correctly develop an equivalent system is three, corresponding to the mass of both masses and the distance l_2 of the second mass m_2 with respect to the first mass m_1.

For the purpose of this thesis, but without loss of generality, a cylindrical body with uniformly distributed mass M and length L will be used. The three equations that permit the calculation the above mentioned variables are

$$\begin{cases} m_1 + m_2 = M \\ m_1 \frac{L}{2} = m_2(l_2 - \frac{L}{2}) \\ m_1(\frac{L}{2})^2 + m_2(l_2 - \frac{L}{2})^2 = \frac{1}{12}ML^2 \end{cases} \tag{2.61}$$

The first equation of system (2.61) ensures that the equivalent system has the same total mass of the cylindrical body, the second one places the center of gravity at the center of the body and the third one ensures an equivalence of the centroidal moment of inertia.

By solving system (2.61) the characterizing values for the two-masses equivalent system are given by

$$\begin{cases} m_1 = \frac{1}{4}M \\ m_2 = \frac{3}{4}M \\ l_2 = \frac{7}{12}L \end{cases} \tag{2.62}$$

It is to be noted that, by changing second and third equations in (2.61), a two-masses equivalent system can always be found for a generic rigid body.

2.3 Natural frequencies and dampenings

The pendulum described in previous chapters is a two degrees of freedom system in the case of simple pendulum and a three degrees of freedom system in the case of double pendulum. This is a consequence of considering the cart as free to be moved on the rail, and to be controlled with an applied

force. This consideration is not valid for the case of industrial cranes, where external velocity control loops are always present. The systems described in previous chapters thereby would be useful models when interested in the control of cart motion. Nevertheless, for the study of natural frequencies and dampenings the cart will be considered to be perfectly controlled in position, and therefore the dynamics of the cart will not influence the single or double pendulum (in particular, natural frequencies will not depend on the mass of the cart).

If the cart is controlled in position, the system loses a degree of freedom and the differential equations of single and double pendulum models can be simplified. For the simple pendulum, (2.18) becomes

$$m_1 l_1 \ddot{\theta}_1 + \frac{C_1}{l_1}\dot{\theta}_1 + m_1 g \theta_1 = 0 \tag{2.63}$$

From (2.63) the natural frequency of the double pendulum is

$$\omega_n = \sqrt{\frac{g}{l}} \tag{2.64}$$

The undamped period is therefore

$$T = \frac{2\pi}{\omega_n} = 2\pi\sqrt{\frac{l}{g}} \tag{2.65}$$

which is known as Christiaan Huygens law for the period [11]. In order to find the damping ratio of the system, we consider the general solution for (2.63)

$$\theta_1(t) = Ce^{\lambda t} \tag{2.66}$$

Substituting (2.66) in (2.63) leads to

$$Ce^{\lambda t}\left(m_1 l_1 \lambda^2 + \frac{C_1}{l_1}\lambda + m_1 g\right) = 0 \tag{2.67}$$

As $Ce^{\lambda t}$ is never equal to zero, (2.67) is satisfied if

$$m_1 l_1 \lambda^2 + \frac{C_1}{l_1}\lambda + m_1 g = 0 \tag{2.68}$$

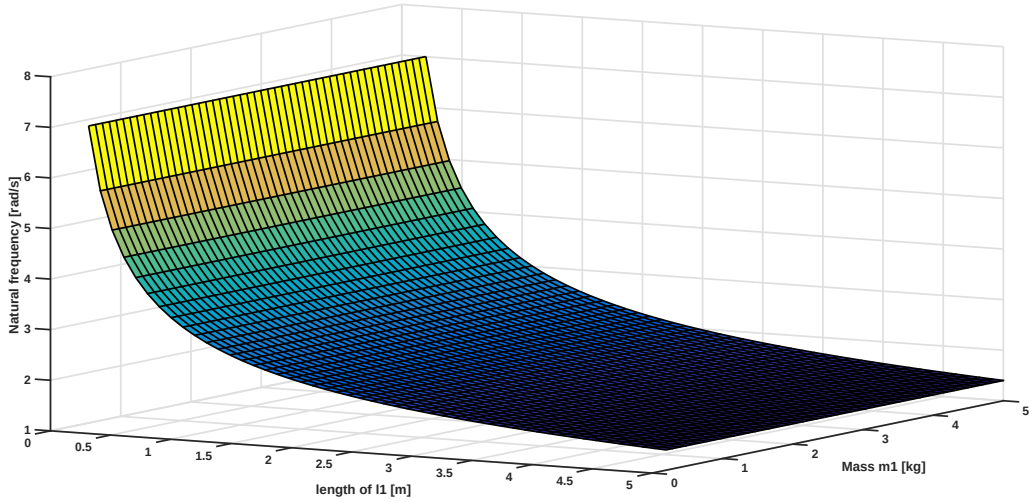

Figure 2.3: Natural frequency of the simple pendulum model with respect to variations of cable length l_1 and mass m_1.

.

The solutions of the characteristic equation (2.68) are

$$\lambda_{1,2} = \frac{-\dfrac{C_1}{l_1} \pm \sqrt{\dfrac{C_1^2}{l_1^2} - 4l_1 m_1^2 g}}{2m_1 l_1} \tag{2.69}$$

The value of C_1 for which the discriminant of (2.69) is equal to zero is the critical damping, and is given for

$$C_{1_c} = 2m_1 l_1 \sqrt{g l_1} \tag{2.70}$$

The damping ratio is finally given by the ratio between the damping coefficient of the system and its critical damping, that is

$$\xi = \frac{C_1}{C_{1_c}} = \frac{C_1}{2m_1 l_1 \sqrt{g l_1}} \tag{2.71}$$

The dependence of ω_n and ξ from l_1 and m_1 is shown in Figure 2.3 and 2.4.

Regarding the double pendulum model, under the assumption of a position controlled cart and for the study of its natural frequencies and damping ratios, the system loses a degree of freedom and (2.52) becomes

$$\mathcal{M}_\nabla \ddot{\boldsymbol{x}} + \mathcal{C}_\nabla \dot{\boldsymbol{x}} + \mathcal{K}_\nabla \boldsymbol{x} = \boldsymbol{F} \tag{2.72}$$

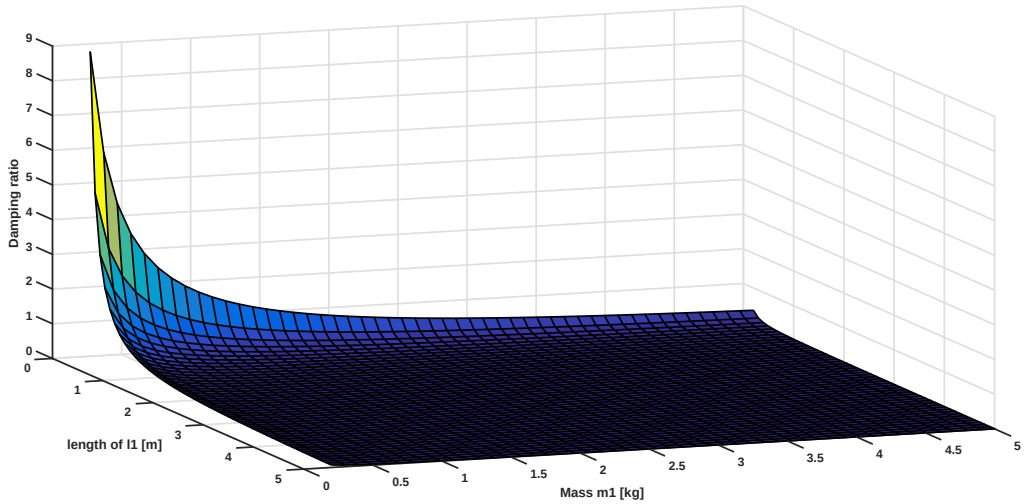

Figure 2.4: Damping ratio ξ of the simple pendulum with respect to variations of the mass m_1 and the cable length l_1.

.

where

$$\mathcal{M}_\nabla = \begin{pmatrix} (m_1+m_2)l_1^2 & m_2 l_1 l_2 \\ m_2 l_1 l_2 & m_2 l_2^2 \end{pmatrix}$$

$$\mathcal{C}_\nabla = \begin{pmatrix} \frac{C_1}{l_1} & 0 \\ 0 & \frac{C_2}{l_2} \end{pmatrix} \tag{2.73}$$

$$\mathcal{K}_\nabla = \begin{pmatrix} (m_1+m_2)gl_1 & 0 \\ 0 & m_2 g l_2 \end{pmatrix}$$

and

$$\boldsymbol{x} = \begin{pmatrix} \theta_1 \\ \theta_2 \end{pmatrix} \quad , \quad \boldsymbol{F} = \begin{pmatrix} 0 \\ 0 \end{pmatrix} \tag{2.74}$$

In order to find the natural frequencies, consider the undamped system

$$\mathcal{M}_\nabla \ddot{\boldsymbol{x}} + \mathcal{C}_\nabla \dot{\boldsymbol{x}} + \mathcal{K}_\nabla \boldsymbol{x} = \boldsymbol{F} \tag{2.75}$$

Natural frequencies are given by the solution of

$$det(\mathcal{K}_\nabla - \omega_n^2 \mathcal{M}_\nabla) = det \begin{pmatrix} (m_1+m_2)gl_1 - \omega_n^2(m_1+m_2)l_1^2 & -\omega_n^2 m_2 l_1 l_2 \\ -\omega_n^2 m_2 l_1 l_2 & m_2 g l_2 - \omega_n^2 m_2 l_2^2 \end{pmatrix} = 0 \tag{2.76}$$

that is finding the solution to

$$a{\omega_n}^4 + b{\omega_n}^2 + c = 0 \tag{2.77}$$

where

$$\begin{aligned} a =& {l_1}^2 {l_2}^2 m_1 m_2, \\ b =& -l_1 l_2 m_2 (g l_1 m_1 + g l_1 m_2 + g l_2 m_1 + g l_2 m_2) \\ c =& l_1 l_2 m_2 (g^2 m_1 + g^2 m_2) \end{aligned}$$

To (2.77) it can be associated

$$a\gamma^2 + b\gamma + c = 0 \tag{2.78}$$

whose solutions are

$$\gamma_{1,2} = \frac{-b \pm \sqrt{b^2 - 4ac}}{2a} \tag{2.79}$$

Consequently, considering only the positive solutions, the natural frequencies of the pendulum are

$$\begin{aligned} \omega_1 =& \sqrt{\gamma_1} = \sqrt{\frac{-b + \sqrt{b^2 - 4ac}}{2a}} \\ \omega_2 =& \sqrt{\gamma_1} = \sqrt{\frac{-b - \sqrt{b^2 - 4ac}}{2a}} \end{aligned} \tag{2.80}$$

The dependence of the natural frequencies of the double pendulum (2.51) on the masses m_1 and m_2 and cable length l_1 and l_2 is shown in Figure 2.5. Here the lengths l_1 and l_2 vary while the total length $l_1 + l_2$ is kept constant to 6 $[m]$, and also the masses varies varies, keeping the sum of m_1 and m_2 constant and equal to 20 $[kg]$.

As observed in [25], due to the low dependence on the mass and the strong dependence on the cable length, the low frequency of the double pendulum system is comparable to the natural frequency of a simple pendulum with mass $m_1 = m_1 + m_2$ and length $l_1 = l_1 + l_2$, as shown by Figure 2.6.

In Figure 2.7 the dependence of the two natural periods of the system is shown.

The calculation of the damping ratios of a multi-modal system requires the solution of a complex eigenvalues problem. Given the model of the system in the form

$$\mathcal{M}\ddot{\boldsymbol{x}} + \mathcal{C}\dot{\boldsymbol{x}} + \mathcal{K}\boldsymbol{x} = 0$$

assume a solution in the form

$$\boldsymbol{x}(t) = ue^{\lambda t}$$

The values of λ and u that describe the solution of the system satisfy

$$(\lambda_i^2\mathcal{M} + \lambda_i\mathcal{C} + \mathcal{K})u_i = 0 \tag{2.81}$$

In the case of underdamped systems, which is always the case of cranes, there are $2n$ values of λ_i, where n corresponds to the number of natural frequencies of the system, occurring in complex conjugate pairs in the form

$$\lambda_{i,i+1} = -\xi_i\omega_i \pm j\omega_i\sqrt{1-\xi_i^2} \tag{2.82}$$

where ξ_i is the ith modal damping ratio and ω_i is the ith undamped natural frequency.

In particular, expressing λ_i as

$$\lambda_i = \alpha_i + j\beta_i$$

then

$$\omega_i = \sqrt{\alpha_i^2 + \beta_i^2} \tag{2.83}$$

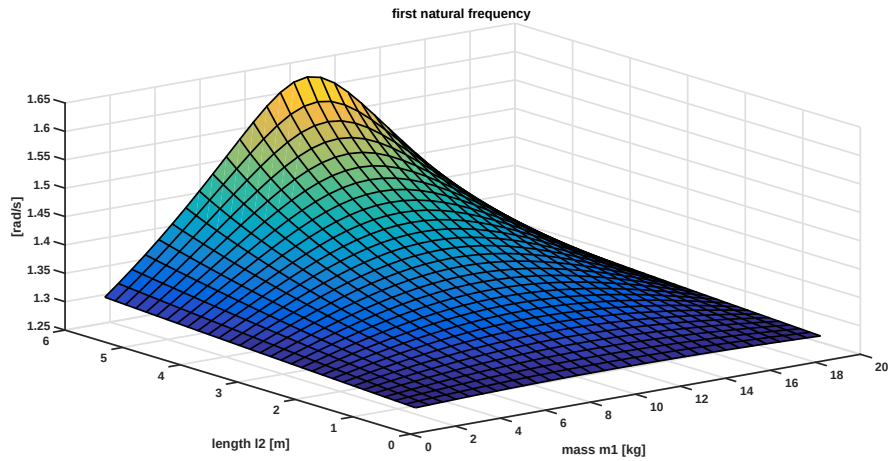

(a) First natural frequency

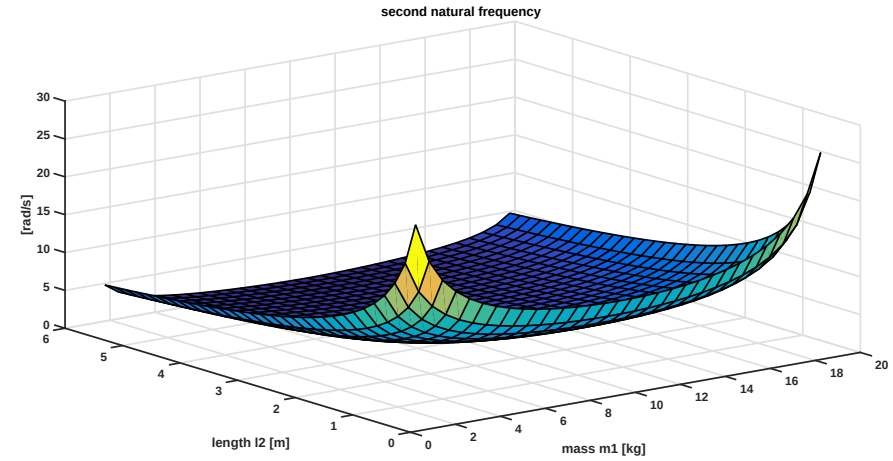

(b) Second natural frequency

Figure 2.5: The two undamped natural frequencies of the double pendulum model with respect to variations of cable length l_2 and masses ratio R.

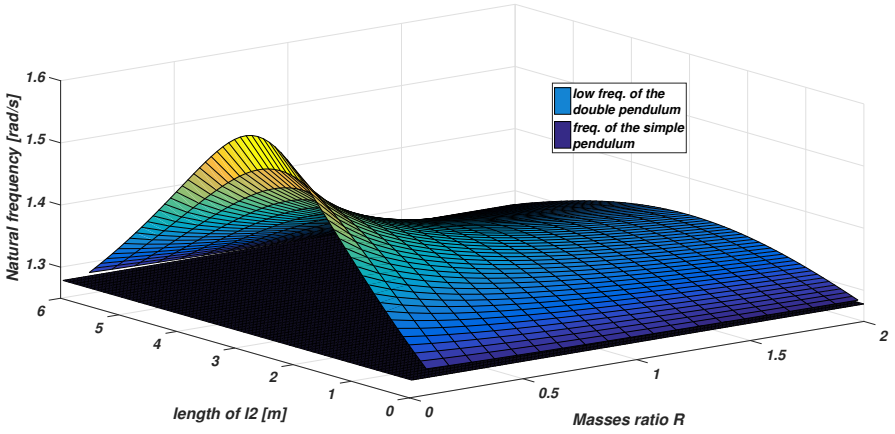

Figure 2.6: The low natural frequency of the double pendulum model compared to the frequency of the simple pendulum model with same total cable length.

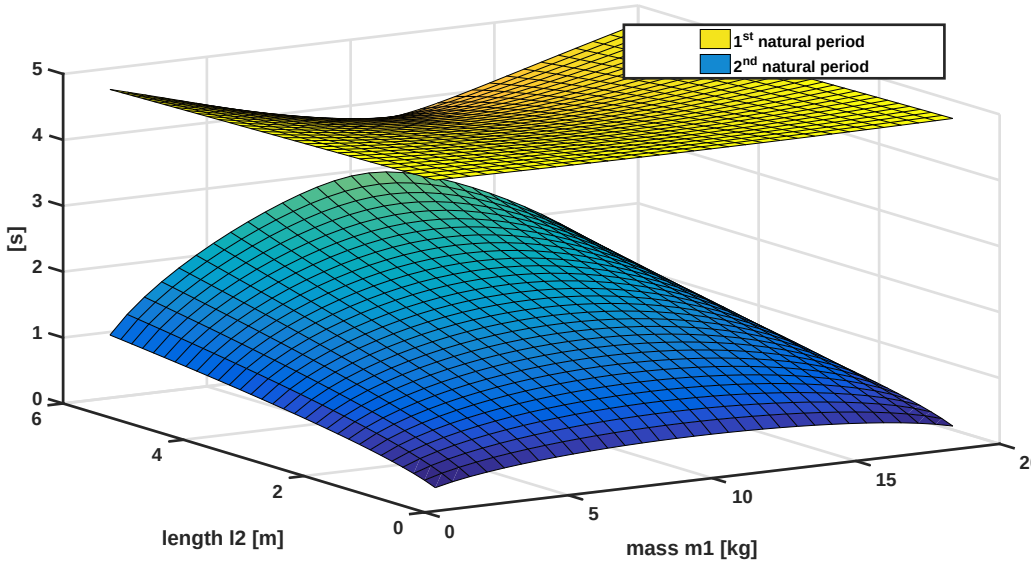

Figure 2.7: Natural periods of the double pendulum.

and

$$\xi_i = \frac{-\alpha_i}{\sqrt{\alpha_i^2 + \beta_i^2}} \tag{2.84}$$

For a further and more detailed discussion of computational methods for the numerical determination of complex eigenvalues for natural frequencies and damping ratios of multi-modal systems see [14].

2.4 Transfer functions

For dynamics inversion methods it will be necessary to obtain some useful transfer functions. In this section transfer functions between force and payload position, cart position and payload position and between force and cart position will be explicitly calculated.

2.4.1 Simple pendulum

In order to find the relation between the force U acting on the cart and the payload position X_P it is sufficient to consider the state space description given by matrices (2.1.2), (2.1.2) and (2.26) and to remember the formula to pass from a state space description to the transfer function:

$$G(s) = \mathcal{C}(\mathcal{I}s - \mathcal{A})^{-1}\mathcal{B} + \mathcal{D} \tag{2.85}$$

where $\mathcal{D}$ is a null matrix in the case of strictly proper systems. The transfer function therefore is given by

$$\frac{X_P(s)}{U(s)} = \frac{C_1 s + g m_1 l_1^2}{D_{P_1}(s)} \tag{2.86}$$

with

$$\begin{aligned} D_{P_1}(s) = (l_1^2 m_1 m_C)s^4 + (C_c m_1 l_1^2 + C_1 m_1 + C_1 m_C)s^3 \\ +(g l_1^2 m_1^2 + g m_C l_1^2 m_1 + C_1 C_c)s^2 + (C_c g l_1^2 m_1)s \end{aligned}$$

Similarly, by changing matrix $\mathcal{C}$ and assigning the value $\mathcal{C} = \begin{pmatrix} 1 & 0 & 0 & 0 \end{pmatrix}$ the transfer function from the force U applied to the cart and the position of the cart X_C is given by (2.85) and it has the form

$$\frac{X_C(s)}{U(s)} = \frac{({l_1}^2 m_1)s^2 + C_1 s + g {l_1}^2 m_1}{D_{C_1}(s)} \tag{2.87}$$

with

$$D_{C_1}(s) = ({l_1}^2 m_1 m_C)s^4 + (C_c m_1 {l_1}^2 + C_1 m_1 + C_1 m_C)s^3 \\ +(g{l_1}^2 {m_1}^2 + g m_C {l_1}^2 m_1 + C_1 C_c)s^2 + (C_c g {l_1}^2 m_1)s$$

From (2.86) and (2.87) the transfer function between the position of the cart X_C and the position of the payload X_P can be obtained as

$$\frac{X_P(s)}{X_C(s)} = \frac{X_P(s)}{U(s)} \frac{U(s)}{X_C(s)} = \frac{g m_1 {l_1}^2 + C_1 s}{({l_1}^2 m_1)s^2 + C_1 s + g {l_1}^2 m_1} \tag{2.88}$$

Equation (2.88) characterizes also the relation between cart velocity V_C and payload velocityV_P. The transfer function where the input is the cart velocity V_C and the output is payload velocity V_P can easily be found by integrating equation (2.88):

$$\frac{X_P(s)}{V_C(s)} = \frac{1}{s} \frac{X_P(s)}{X_C(s)} = \frac{s + \frac{g m_1 l_1^2}{C_1}}{s(s^2 + \frac{C_1}{m_1 l_1^2} s + g)} \tag{2.89}$$

In the case of low damping, such is the case of cranes, the zeroes in the transfer functions (2.86) and (2.88) are far more rapid than the poles of the system and they can be simplified without affecting the results.

In particular, (2.86) results in

$$\frac{X_P(s)}{U(s)} = \frac{g l_1^2 m_1}{D_{P_1}(s)} \tag{2.90}$$

with

$$D_{P_1}(s) = (l_1^2 m_1 m_C)s^4 + (C_c m_1 l_1^2 + C_1 m_1 + C_1 m_C)s^3 \\ +(g l_1^2 m_1^2 + g m_C l_1^2 m_1 + C_1 C_c)s^2 + (C_c g l_1^2 m_1)s$$

and equation (2.88) results in

$$\frac{X_P(s)}{X_C(s)} = \frac{g m_1 {l_1}^2}{({l_1}^2 m_1)s^2 + C_1 s + g {l_1}^2 m_1} \tag{2.91}$$

2.4.2 Double pendulum

As in the previous section, transfer functions of the double pendulum model will be calculated using its state space description, that is, from matrices (2.57), (2.58) and (2.60). The transfer function between the force U acting on the cart and the position of the payload X_P is given by equation (2.85) and its given by

$$\frac{X_P(s)}{U(s)} = \frac{N_{P_2}(s)}{D_{P_2}(s)} \tag{2.92}$$

with

$$\begin{aligned} N_{P_2}(s) = &(C_1C_2)s^2 + (C_1gm_2{l_2}^2 + C_2(g{l_1}^2m_1 + g{l_1}^2m_2))s \\ &+ g{l_2}^2m_2(g{l_1}^2m_1 + g{l_1}^2m_2) \end{aligned}$$

and

$$\begin{aligned} D_{P_2}(s) =&({l_1}^3{l_2}^3m_1m_2m_C)s^5 + (C_1{l_2}^3m_1m_2 + C_2{l_1}^3m_1m_C + C_1{l_2}^3m_2m_C \\ &+ C_2{l_1}^3m_2m_C + C_c{l_1}^3{l_2}^3m_1m_2)s^4 + (gm_C{l_1}^3{l_2}^2m_1m_2 + gm_C{l_1}^3{l_2}^2{m_2}^2 \\ &+ C_2C_c{l_1}^3m_1 + C_2C_c{l_1}^3m_2 + g{l_1}^2{l_2}^3{m_1}^2m_2 + g{l_1}^2{l_2}^3m_1{m_2}^2 \\ &+ gm_C{l_1}^2{l_2}^3m_1m_2 + gm_C{l_1}^2{l_2}^3{m_2}^2 + C_1C_c{l_2}^3m_2 + C_1C_2m_1 + C_1C_2m_2 \\ &+ C_1C_2m_C)s^3 + (C_cg{l_1}^3{l_2}^2m_1m_2 + C_cg{l_1}^3{l_2}^2{m_2}^2 + C_cg{l_1}^2{l_2}^3m_1m_2 \\ &+ C_cg{l_1}^2{l_2}^3{m_2}^2 + C_2g{l_1}^2{m_1}^2 + 2C_2g{l_1}^2m_1m_2 + C_2gm_C{l_1}^2m_1 \\ &+ C_2g{l_1}^2{m_2}^2 + C_2gm_C{l_1}^2m_2 + C_1g{l_2}^2m_1m_2 + C_1g{l_2}^2{m_2}^2 \\ &+ C_1gm_C{l_2}^2m_2 + C_1C_2C_c)s^2 + (g^2{l_1}^2{l_2}^2{m_1}^2m_2 + 2g^2{l_1}^2{l_2}^2m_1{m_2}^2 \\ &+ m_Cg^2{l_1}^2{l_2}^2m_1m_2 + g^2{l_1}^2{l_2}^2{m_2}^3 + m_Cg^2{l_1}^2{l_2}^2{m_2}^2 + C_2C_cg{l_1}^2m_1 \\ &+ C_2C_cg{l_1}^2m_2 + C_1C_cg{l_2}^2m_2)s + (C_cg^2{l_1}^2{l_2}^2{m_2}^2 + C_cm_1g^2{l_1}^2{l_2}^2m_2) \end{aligned}$$

The transfer function between the force U acting on the cart and the position of the cart X_C can be obtained by (2.85) setting $\mathcal{C} = \begin{pmatrix} 1 & 0 & 0 & 0 & 0 & 0 \end{pmatrix}$, yielding

$$\frac{X_C(s)}{U(s)} = \frac{N_{C_2}(s)}{D_{C_2}(s)} \tag{2.93}$$

with

$$\begin{aligned} N_{C_2}(s) = &({l_1}^3{l_2}^3m_1m_2)s^4 + (C_2{l_1}^3m_1 + C_1{l_2}^3m_2 + C_2{l_1}^3m_2)s^3 \\ &+ (g{l_1}^3{l_2}^2{m_2}^2 + gm_1{l_1}^3{l_2}^2m_2 + g{l_1}^2{l_2}^3{m_2}^2 + gm_1{l_1}^2{l_2}^3m_2 + C_1C_2)s^2 \\ &+ (C_2g{l_1}^2m_1 + C_1g{l_2}^2m_2 + C_2g{l_1}^2m_2)s \\ &+ (g^2{l_1}^2{l_2}^2{m_2}^2 + m_1g^2{l_1}^2{l_2}^2m_2) \end{aligned}$$

and

$$\begin{aligned}C_{C_2}(s) =&(l_1{}^3l_2{}^3m_1m_2m_C)s^6 + (C_1l_2{}^3m_1m_2 + C_2l_1{}^3m_1m_C + C_1l_2{}^3m_2m_C \\ &+ C_2l_1{}^3m_2m_C + C_cl_1{}^3l_2{}^3m_1m_2)s^5 + (gm_Cl_1{}^3l_2{}^2m_1m_2 + gm_Cl_1{}^3l_2{}^2m_2{}^2 \\ &+ C_2C_cl_1{}^3m_1 + C_2C_cl_1{}^3m_2 + gl_1{}^2l_2{}^3m_1{}^2m_2 + gl_1{}^2l_2{}^3m_1m_2{}^2 \\ &+ gm_Cl_1{}^2l_2{}^3m_1m_2 + gm_Cl_1{}^2l_2{}^3m_2{}^2 + C_1C_cl_2{}^3m_2 + C_1C_2m_1 + C_1C_2m_2 \\ &+ C_1C_2m_C)s^4 + (C_cgl_1{}^3l_2{}^2m_1m_2 + C_cgl_1{}^3l_2{}^2m_2{}^2 + C_cgl_1{}^2l_2{}^3m_1m_2 \\ &+ C_cgl_1{}^2l_2{}^3m_2{}^2 + C_2gl_1{}^2m_1{}^2 + 2C_2gl_1{}^2m_1m_2 + C_2gm_Cl_1{}^2m_1 \\ &+ C_2gl_1{}^2m_2{}^2 + C_2gm_Cl_1{}^2m_2 + C_1gl_2{}^2m_1m_2 + C_1gl_2{}^2m_2{}^2 \\ &+ C_1gm_Cl_2{}^2m_2 + C_1C_2C_c)s^3 + (g^2l_1{}^2l_2{}^2m_1{}^2m_2 + 2g^2l_1{}^2l_2{}^2m_1m_2{}^2 \\ &+ m_Cg^2l_1{}^2l_2{}^2m_1m_2 + g^2l_1{}^2l_2{}^2m_2{}^3 + m_Cg^2l_1{}^2l_2{}^2m_2{}^2 \\ &+ C_2C_cgl_1{}^2m_1 + C_2C_cgl_1{}^2m_2 + C_1C_cgl_2{}^2m_2)s^2 + (C_cg^2l_1{}^2l_2{}^2m_2{}^2 \\ &+ C_cm_1g^2l_1{}^2l_2{}^2m_2)s\end{aligned} \tag{2.94}$$

Finally, the transfer function between cart position X_C and payload X_P can be obtained by (2.92) and (2.93):

$$\frac{X_P(s)}{X_C(s)} = \frac{X_P(s)}{U(s)}\frac{U(s)}{X_C(s)} = \frac{N_{PC_2}(s)}{N_{PC_2}(s)} \tag{2.95}$$

with

$$\begin{aligned}N_{PC_2}(s) = &(C_1C_2)s^2 + (C_1gm_2l_2{}^2 + C_2(gl_1{}^2m_1 + gl_1{}^2m_2))s \\ &+ gl_2{}^2m_2(gl_1{}^2m_1 + gl_1{}^2m_2)\end{aligned}$$

and

$$\begin{aligned}D_{PC_2}(s) = &(l_1{}^3l_2{}^3m_1m_2)s^4 + (C_2l_1{}^3m_1 + C_1l_2{}^3m_2 + C_2l_1{}^3m_2)s^3 \\ &+ (gl_1{}^3l_2{}^2m_2{}^2 + gm_1l_1{}^3l_2{}^2m_2 + gl_1{}^2l_2{}^3m_2{}^2 + gm_1l_1{}^2l_2{}^3m_2 + C_1C_2)s^2 \\ &+ (C_2gl_1{}^2m_1 + C_1gl_2{}^2m_2 + C_2gl_1{}^2m_2)s \\ &+ (g^2l_1{}^2l_2{}^2m_2{}^2 + m_1g^2l_1{}^2l_2{}^2m_2)\end{aligned}$$

In the case of low damping, such is the case of industrial overhead cranes, the zeroes in the transfer functions (2.92) and (2.95) are farer from the imaginary axis than the poles of the system and can be neglected for control purposes. In particular, (2.92) results in

$$\frac{X_P(s)}{U(s)} = \frac{N_{simpP_2}(s)}{D_{simpP_2}(s)} \tag{2.96}$$

where

$$N_{simpP_2}(s) = g^2 {l_1}^2 {l_2}^2 m_2(m_1 + m_2)$$

and

$$D_{simpP_2}(s) = D_{P_2}(s)$$

, while (2.95) results in

$$\frac{X_P(s)}{X_C(s)} = \frac{N_{simpC_2}(s)}{D_{simpC_2}(s)} \tag{2.97}$$

with

$$N_{simpC_2}(s) = g^2 {l_1}^2 {l_2}^2 m_2(m_1 + m_2)$$

and

$$D_{simpC_2}(s) = D_{C_2}(s)$$

.

Chapter 3

Input Shaping

Among open-loop control techniques to generate non-oscillatory response in overhead cranes the most popular one is the *Input Shaping*, initially theorized in the late '50s in [32] and [6] and formalized later in [29]. This technique exploits the superposition principle for linear systems, shaping the input command in order to generate a series of superposed outputs which sum generates a non-oscillatory response. Usually, a nominal desired profile of velocity or position is given, and the input is shaped thanks to the knowledge of some key features of the system, i.e. natural frequencies and damping.

3.1 Mathematical formalization of the method

The most simple oscillatory system can be modeled as a second order system, which impulse response is given [16] by

$$y(t) = \left[A \frac{\omega_n}{\sqrt{1-\xi^2}} \exp^{\omega_n (t-t_0)} \right] \sin(\omega_n \sqrt{1-\xi^2 (t-t_0)}) \tag{3.1}$$

where A is impulse amplitude, ω_n is the system natural frequency and ξ is the damping. The impulse response (3.1) is shown in Figure 3.1.

Exploiting the superposition principle for linear systems, the response to two impulses is the sum of two responses in the form (3.1) can be written like

$$B_1 \sin(\alpha t + \phi_1) + B_2 \sin(\alpha t + \phi_2) = A_{amp} \sin(\alpha t + \psi) \tag{3.2}$$

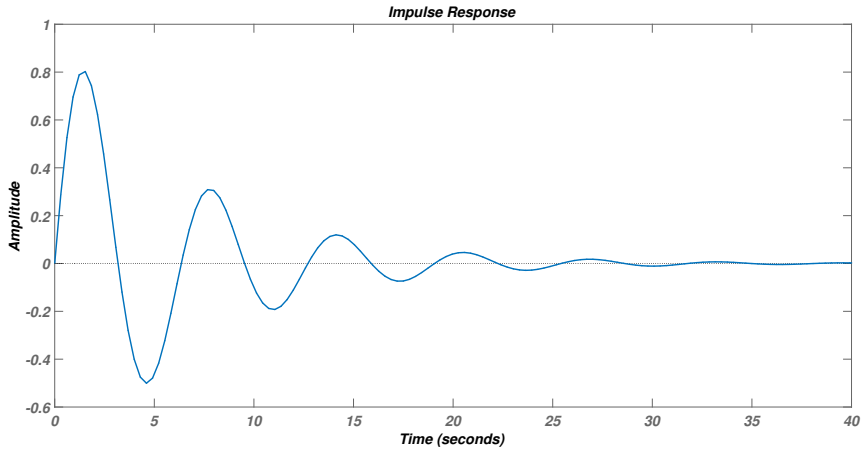

Figure 3.1: Impulse response of a second order system with $\omega_n = 1$ and $\xi = 0.3$.

where

$$\begin{aligned} A_{amp} &= \sqrt{(B_1 \cos\phi_1 + B_2 \cos\phi_2)^2 + (B_1 \sin\phi_1 + B_2 \sin\phi_2)^2} \\ \psi &= \tan^{-1}\left(\frac{B_1 \cos\phi_1 + B_2 \cos\phi_2}{B_1 \sin\phi_1 + B_2 \sin\phi_2}\right) \end{aligned} \tag{3.3}$$

Generalizing (3.2) for the case of N impulses we find

$$\begin{aligned} A_{amp} &= \sqrt{(\sum_{j=1}^{N} B_j \cos\phi_j)^2 + (\sum_{j=1}^{N} B_j \sin\phi_j)^2} \\ \phi_j &= \omega_n \sqrt{(1-\xi^2)t_j} \end{aligned} \tag{3.4}$$

with

$$\begin{aligned} B_j &= \frac{A_j \omega_n}{\sqrt{1-\xi^2}} e^{-\xi\omega_n(t_N - t_j)} \\ \phi_j &= \omega_n \sqrt{1-\xi^2}(t - t_j) \end{aligned} \tag{3.5}$$

where t_j is the instant of time when the impulse j is given as an input to the system.

To have a non-oscillatory response, the amplitude A_{amp} has to be equal

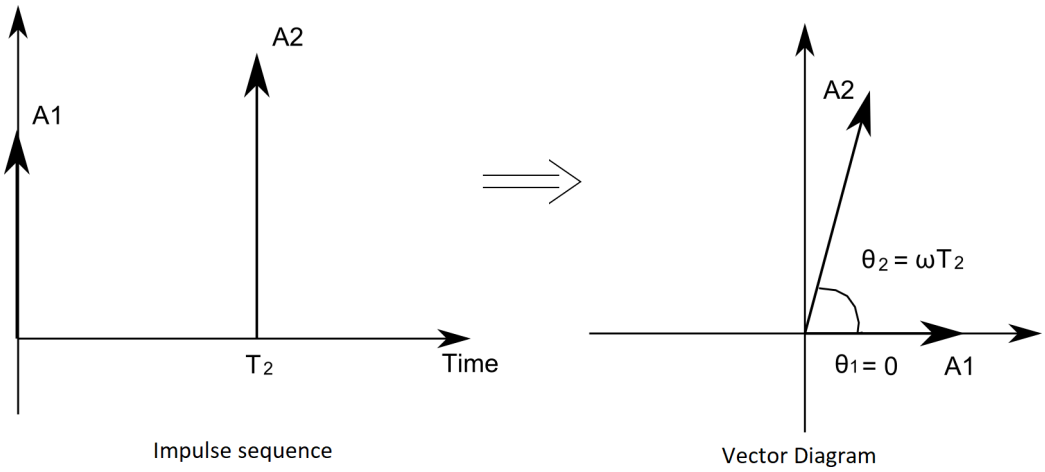

Figure 3.2: Transposition of 2 vectors on a vector diagram

to zero. This yields to

$$\begin{cases} B_1 \cos\phi_1 + B_2 \cos\phi_2 + ... + B_N \cos\phi_N = 0 \\ B_1 \sin\phi_1 + B_2 \sin\phi_2 + ... + B_N \sin\phi_N = 0 \end{cases} \tag{3.6}$$

that, given (3.5), can be written as

$$\begin{cases} \sum_{j=1}^{N} A_j e^{-\xi\omega_n(t_N - t_j)} \sin(t_j \omega_n \sqrt{1-\xi^2}) = 0 \\ \sum_{j=1}^{N} A_j e^{-\xi\omega_n(t_N - t_j)} \cos(t_j \omega_n \sqrt{1-\xi^2}) = 0 \end{cases} \tag{3.7}$$

3.2 Vector diagrams approach

Another way to approach the input shaping technique is through vector diagrams, as in [31]. Representing the impulses with polar coordinates r and θ, the sum of the responses can be calculated as a vectors' sum. An impulse on a vector diagram can be represented by setting r equal to its amplitude A_j and its phase $\phi_j = \omega_n t_j$. Figure 3.2 show the transposition from time domain graphic representation and vector diagrams. In the case of null damping, the amplitude R of the vectorial sum of the impulses in Figure 3.3 is proportional to the amplitude of residual vibration. It is moreover important to observe that, once the resultant vector is found, a single impulse with same amplitude θ_r and with a phase of $\theta = \theta_r + \pi$ is enough to ensure a zero residual vibration.

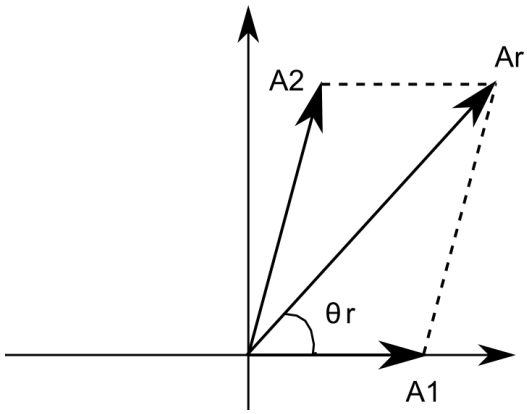

Figure 3.3: Sum of two impulses contribution with vector diagrams.

Following the rules for vectorial sum, the resultant from a series of N vectors is given by

$$\begin{aligned} A_r &= \sqrt{(\sum_{j=1}^{N} A_{j_x})^2 + (\sum_{j=1}^{N} A_{j_y})^2} \\ \theta_r &= \tan^{-1}\left(\frac{\sum_{j=1}^{N} A_{j_x}}{\sum_{j=1}^{N} A_{j_y}}\right) \end{aligned} \tag{3.8}$$

where $A_{j_x} = A_j \cos\theta_j$ and $A_{j_y} = A_j \sin\theta_j$. Note that(3.8) correspond to (3.4) written in with polar coordinates.

By introducing the effects of damping, the representation of impulse vectors must be modified. First of all, damped natural frequency substitutes the natural frequency, so that the phase of impulses become

$$\theta_j = \sqrt{1-\xi^2}\omega_n t_j \tag{3.9}$$

where ξ is the damping coefficient. Finally, the amplitude of the impulses must decrease dynamically with time depending on the value of ξ:

$$A_j(t) = A_j e^{-\xi\omega_n(t-t_j)} \tag{3.10}$$

Substituting (3.9) and (3.10) in (3.8) equation (3.7) can be found again.

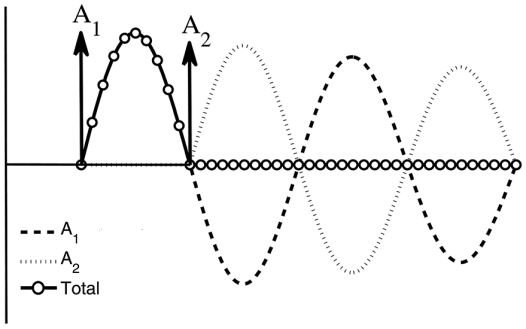

Figure 3.4: Two-impulse IS method.

3.3 Two-impulse input shaping

The simplest input shaping method, and by far the most diffused in industry, is the two-impulse input shaping, also called *Zero-Vibration* (ZV) shaper. Here, two impulses are given as inputs to the system, generating two oscillatory responses which cancel each other. Solving system (3.7) for $N = 2$ yields the solution shown in Figure 3.5: two impulses at time $t_1 = 0$ and $t_2 = \Delta T$ of amplitude

$$A_1 = A\frac{1}{1+K} \quad , \quad A_2 = A\frac{K}{1+K} \tag{3.11}$$

where A is a scaling factor and

$$\begin{aligned} K &= e^{-\frac{\xi\pi}{\sqrt{1-\xi^2}}} \\ \Delta T &= \frac{\pi}{w_0\sqrt{1-\xi^2}} \end{aligned} \tag{3.12}$$

Two-impulse input shaping is graphically illustrated in Figure 3.4, both in time domain and on a vector graph. It can be noted the intuitiveness of the representation of the method with the representation on vector graphs.

The series of two impulses can be organized in a vector of amplitudes and times as

$$\mathbf{ZV} = \begin{bmatrix} A_i \\ t_i \end{bmatrix} = \begin{bmatrix} \frac{1}{1+K} & \frac{K}{1+K} \\ 0 & \frac{\pi}{\omega_d} \end{bmatrix} \tag{3.13}$$

with $\omega_d = \omega_n\sqrt{1-\xi^2}$ damped natural frequency of the system.

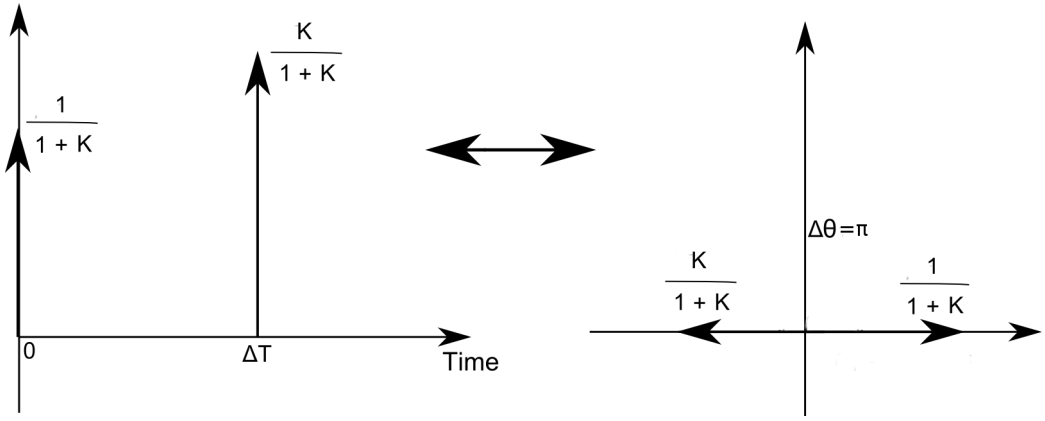

Figure 3.5: Graphical representation of two-impulse input shaping.

3.4 ZVD and ZVDD

As will be shown in Chapter 3.5, ZV method ensures zero residual oscillation if the system natural frequency is exactly equal to the one of the model, but its performances degrade rapidly in case of modelling errors. To increase the robustness of the shaper, the number of impulses can be increased. By adding an impulse to ZV shaper, other conditions have to be included, as system (3.7) gives just two equations, while with three-impulse input require solving five unknown parameters,A_1, A_2, A_3, t_2, t_3. Two more equations are required, and can be introduced as shown in [10] by making the derivative of the constraint system (3.7) with respect to natural frequency of the system equal to zero, that is adding the constraint

$$\begin{cases} \sum_{j=1}^{N} A_j t_j e^{-\xi\omega_n(t_N - t_j)} \cos(t_j \omega_n \sqrt{1-\xi^2}) = 0 \\ \sum_{j=1}^{N} A_j t_j e^{-\xi\omega_n(t_N - t_j)} \cos(t_j \omega_n \sqrt{1-\xi^2}) = 0 \end{cases} \tag{3.14}$$

A specific solution to constraints (3.7) and (3.14) is

$$\mathbf{ZVD} = \begin{bmatrix} A_i \\ t_i \end{bmatrix} = \begin{bmatrix} \frac{1}{1+2K+K^2} & \frac{2K}{1+2K+K^2} & \frac{K^2}{1+2K+K^2} \\ 0 & \frac{\pi}{\omega_d} & \frac{2\pi}{\omega_d} \end{bmatrix} \tag{3.15}$$

The three-impulse shaper is also called *Zero Vibration and Derivative* (ZVD).

Further increasing the robustness, another impulse can be added, and a vector of amplitudes and times for the four impulses can be found by adding

to (3.7) and (3.14) the condition of null second derivative of (3.7) with respect to natural frequency of the system, finding

$$\mathbf{ZVDD} = \begin{bmatrix} A_i \\ \\ t_i \end{bmatrix} = \begin{bmatrix} \dfrac{1}{D_{ZVDD}} & \dfrac{3K}{D_{ZVDD}} & \dfrac{3K^2}{D_{ZVDD}} & \dfrac{K^3}{D_{ZVDD}} \\ \\ 0 & \dfrac{\pi}{\omega_d} & \dfrac{2\pi}{\omega_d} & \dfrac{3\pi}{\omega_d} \end{bmatrix} \tag{3.16}$$

where

$$D_{ZVDD} = 1 + 3K + 3K^2 + K^3 \tag{3.17}$$

Theoretically, robustness can be further increased by adding impulses and defining ZVDDD, ZVDDDD, etc. methods. Nevertheless, every impulse added increase the total time of control by half of the damped period.

3.5 Robustness and *Extra Insensitive* shapers

All the methods seen guarantee zero residual vibration after the last impulse if the natural frequency and its damping are arbitrarily well estimated. By adding constraints of zero-derivatives, derivative methods are naturally more robust with respect to model errors, as shown in Figure 3.6.

The drawback of increasing robustness by forcing to zero high order derivatives is that the total time of the series of impulses increase. An alternative is to relax the request of zero residual vibration for $\omega = \omega_n$ and allowing the residual vibration to a determined percentage of the unshaped response final oscillation. This can be achieved by changing time and amplitude values of derivative methods, but the same total control time of a derivative method with equal number of impulses.

For example, a shaper of this type with three impulses, called *Extra Insensitive* (EI) shaper has

$$\mathbf{EI} = \begin{bmatrix} A_i \\ t_i \end{bmatrix} = \begin{bmatrix} A_1 & 1-(A_1+A_3) & A_3 \\ \\ 0 & t_2 & \dfrac{2\pi}{\omega_d} \end{bmatrix} \tag{3.18}$$

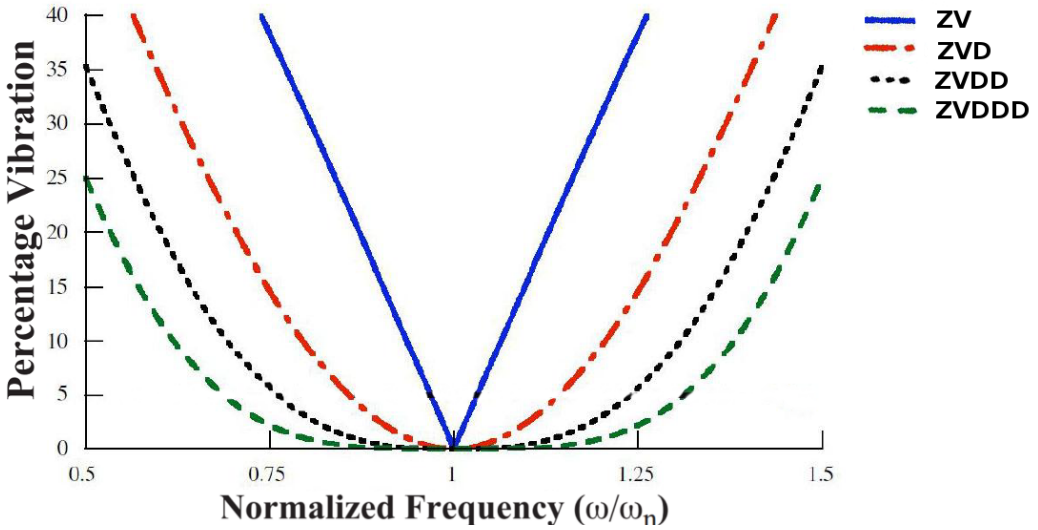

Figure 3.6: Robustness of different Input Shaping methods [33].

with

$$\begin{aligned} A_1 =& 0.24968 + 0.24962V_{tol} + 0.80008\xi + 1.23328V_{tol}\xi + \\ &+ 0.49599\xi^2 + 3.17316V_{tol}\xi^2 \end{aligned}$$

$$\begin{aligned} A_3 =& 0.25149 + 0.21474V_{tol} - 0.83249\xi + 1.41498V_{tol}\xi + \\ &+ 0.85181\xi^2 - 4.90094V_{tol}\xi^2 \end{aligned} \tag{3.19}$$

$$\begin{aligned} t_2 =& \frac{2\pi}{\omega_d}(0.49990 + 0.46159V_{tol}\xi + \\ &+ 4.26169V_{tol}\xi^2 + 1.75601V_{tol}\xi^3 + 8.57843V_{tol}^2\xi - \\ &- 108.644V_{tol}^2\xi^2 + 336.989V_{tol}^2\xi^3) \end{aligned}$$

where V_{tol} is the maximum residual percentage vibration for $\omega = \omega_n$.

In the same way, EI shapers with four and five impulses can be built, called respectively *Two-hump EI* and *Three-hump EI* shapers. Coefficients for the values of impulses' amplitudes and times can be found in [33]. In Figure 3.7 a comparison between ZV shaper and EI shapers is depicted.

Input shaper robustness to errors in damping follows very similar trends, as shown in [33], in Figure 3.8 and in Figure 3.9.

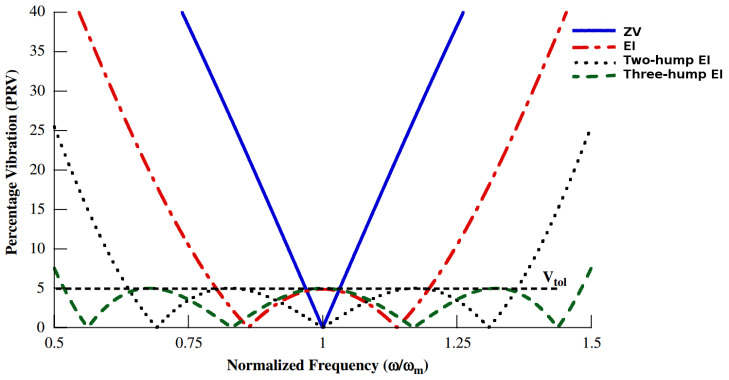

Figure 3.7: Robustness of Extra Intensive shapers [33].

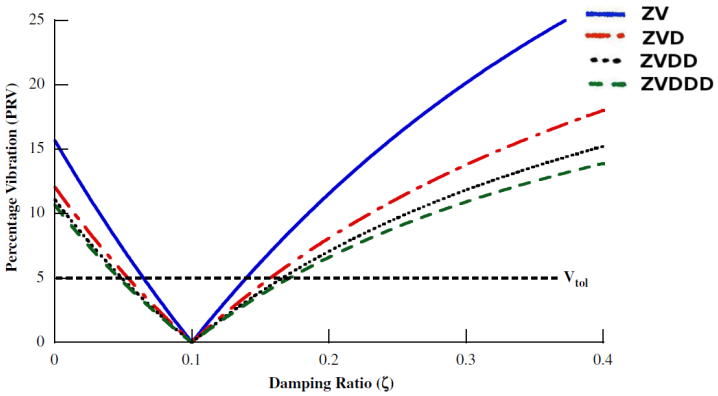

Figure 3.8: Robustness of ZV and ZV derivatives shapers to damping errors [33].

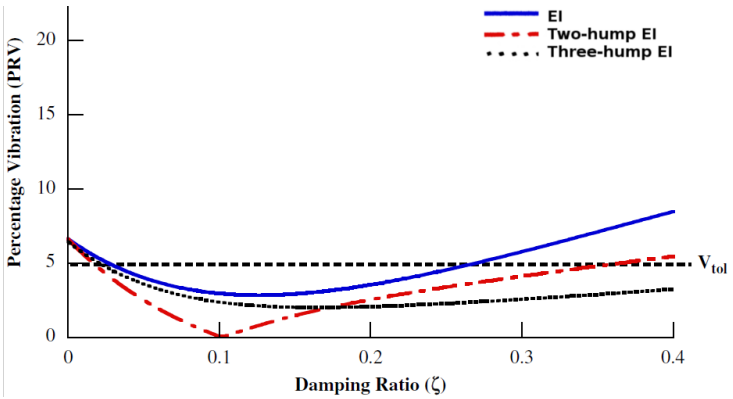

Figure 3.9: Robustness of *Extra Intensive* shapers to damping errors [33].

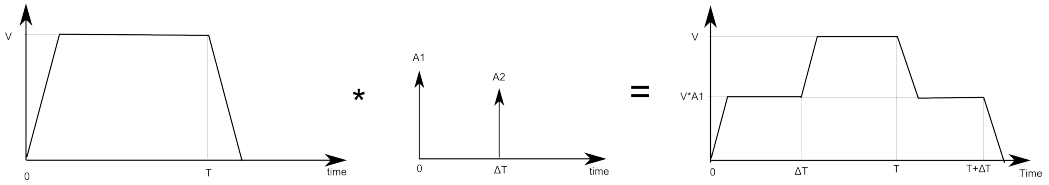

Figure 3.10: Convolution between a general signal and an impulse sequence.

For a complete survey on robust input shapers see [33].

3.6 Using Impulse Input Sequences to Shape Inputs

Until this moment only inputs constituted by sequences of impulses have been considered. In most of the cases it is not possible to use this kind of input for a general system for control purposes. This section presents a method for using the sequences derived above to generate arbitrary inputs with the same vibration-reducing properties, as shown in [29].

The vibration reduction is simply accomplished by convolving any desired input to the system together with the impulse sequence in order to yield to the shortest actual system input that makes the same motion without vibration. The result of a convolution between an arbitrary signal and an impulse sequence is shown in Figure 3.10. The sequence, therefore, becomes a prefilter for any input to be given to the system. This prefilter is the "Input shaper" block in Figure 3.11, which shows the typical structure of an IS prefilter added before a feedback control loop. The resulting time penalty delay due to the convolution equals the length of the impulse sequence, thus a more robust sequence imply a more significant time penalty. The choice of which method between the ones seen and the others presented in [33] depends on project robustness requirements.

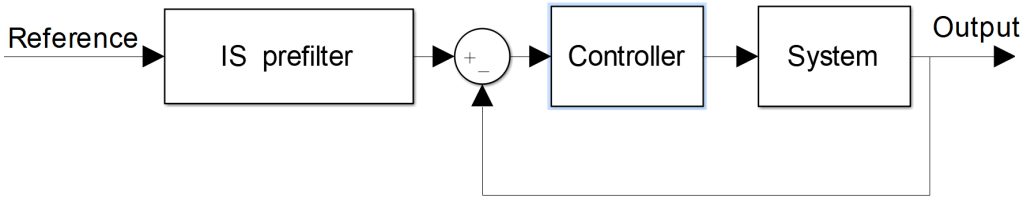

Figure 3.11: Input Shaper prefilter block added before the feedback control loop.

3.7 Input shaping for multi-mode systems

Until now, only systems with a single vibrational mode have been considered. However, the system studied on this thesis is at least a two-mode system. Fortunately, input shaping technique can easily be generalized to multi-mode systems. As a matter of fact, exploiting linear systems proprieties, it is possible to demonstrate [29] that different impulse sequences can be found to deal with every vibrational frequency of the system, and the convolution of these sequences is sufficient to move the system without residual vibration on any of its modes.

A drawback of this solution is that the resulting time penalty is given by the sum of the sequences lengths. Another solution is presented, that consists in solving a system containing all the constraints related to every vibrational mode. For example, if the four equations used to generate the sequence of a ZVD shaper were repeated for two different frequencies on a two-mode system, a system of eight equations would result and could be solved for four unknown impulse amplitudes and times (plus the first, arbitrary impulse), yielding a five-impulse sequence. The resulting sequence has four fewer impulses than the result of convolving the two independent sequences, and is always shorter in time. At any rate, this solution is rarely used in applications, because involves the explicit solution of high order systems, while convolution of simple impulse sequences is computationally simple and, as shown in previous chapters, the calculation of impulse sequences is easily parametrized with ω_n and ξ.

3.8 Input shaping for single and double pendulum systems

Input shaping is a widespread technique for residual vibration reduction in industry, due to its simplicity. In fact, it is not necessary to have an accurate model of the system, but it is sufficient to know its natural frequencies that can be evaluated in a number of way. For the purposes of this thesis, once that the system has been modelled as a single or double pendulum, natural frequencies can be calculated as shown in Chapter 2.3, and the application of input shaping technique is direct.

Chapter 4

Input-output inversion

Even if the input-shaping is the most widely used technique in industry, another open-loop control for residual vibration reduction has been demonstrated to be competitive and implementable with off-the-shelf industrial components [26].

Input-output inversion technique (also called dynamic inversion technique) is a two-step method based on the dynamic inversion of the model of minimum phase systems. First, a desired output trajectory has to be calculated. This trajectory must satisfy some conditions for being an achievable output function; specifically, a certain order of continuity is required, depending on the system to be controlled, and a finite transition time τ is also required. A good form for output's trajectory is the polynomial one [22]. Secondly, the dynamic of the system is inverted, and the input signal is calculated in such a way that the corresponding response of the system is the desired output function.

In this chapter a method for a stable simplified input-output inversion will be presented. The method will be tested by means of simulations and by applying it for the control of the double pendulum crane discussed in Chapter 2.

4.1 Mathematical formalization of the method

Consider a general linear system with transfer function

$$G(s) = k_1 \frac{Y(s)}{U(s)} = k_1 \frac{s^m + b_{m-1}s^{m-1} + ... + b_1 s + b_0}{s^n + a_{n-1}s^{n-1} + ... + a_1 s + a_0} \tag{4.1}$$

with $\rho = n - m$ its relative order. First, a desired output function has to be built, then the inversion of the dynamics will be mathematically formulated and finally the input corresponding to the defined output will be found in a closed form.

4.1.1 Form of the desired output

In order to have zero residual vibration and a finite transition time τ from y_a to y_b, the desired output function $\bar{y}(t)$ has to satisfy the conditions

$$\begin{aligned} \bar{y}(t) &= y_a \quad for \quad t \leq 0 \\ \bar{y}(t) &= y_b \quad for \quad t \geq \tau \end{aligned} \tag{4.2}$$

In order not to have undesirable oscillation for $0 \geq t \geq \tau$ $\bar{y}(t)$ must be also a monotone function. For sake of simplicity but without loss of generality and thanks to the proprieties of linear systems, the system (4.1) will be considered with a gain equal to one, and $y_a = 0, y_b = 1$.

Defining

$$\begin{aligned} B = &\{(u(.), y(.)) \in P \times P : D^n y + a_{n-1}D^{n-1}y + ... + a_0 y \\ &= k_1(D^m u + b_{m-1}D^{m-1}u + ... + b_0 u)\}, \end{aligned} \tag{4.3}$$

as the set of all the possible input-output couples of the system (4.1), the following proposition is valid:

Proposition 1 *Consider a couple* $(u(.), y(.)) \in B$. *Then* $u(.) \in C^l \iff y(.) \in C^{\rho+l}$, *with* $l \in \mathbb{N}^+$.

As it is shown in [22] that the polynomial form is suitable for the output, $\bar{y}(t)$, given conditions (4.2), will have the form

$$y(t) = \begin{cases} 0 & t \leq 0 \\ c_0 + c_1 t + .. + c_{2k+1} t^{2k+1} & 0 < t < \tau \\ 1 & t \geq \tau. \end{cases} \tag{4.4}$$

Coefficients c_i can be found by imposing continuity conditions at $t = 0$ and $t = \tau$ on $\bar{y}(t)$ and its derivatives until the derivative of order k:

$$\begin{cases} y(0) = 0, Dy(0) = 0, ...D^k y(0) = 0 \\ y(\tau) = 1, Dy(\tau) = 0, ...D^k y(\tau) = 0 \end{cases} \tag{4.5}$$

Proposition 1 gives an useful tool for the choice of k, as $2k + 1$ has to be greater of the relative order of system 4.1.

A couple of propositions about the solution of system (4.5) [22], here cited without demonstration, give us the form of $\bar{y}(t)$:

Proposition 2 *The linear system* (4.5) *admits a unique solution for any* $\tau \in \mathbb{R}^+$ *and any* $k \in \mathbb{N}$.

Proposition 3 *The unique solution of system* (4.5) *is given by*

$$\bar{y}(t, \tau) = \frac{(2k+1)!}{(k!)^2 \tau^{2k+1}} \int_0^t \upsilon^k (\tau \upsilon)^k d\upsilon, t \in [0, \tau] \tag{4.6}$$

Equation (4.6) is a monotone function, which guarantees the absence of oscillations during the transient. The integral in (4.6) can be analytically solved giving the output function in the form

$$\bar{y}(t, \tau) = \begin{cases} 0 & t \leq 0 \\ \frac{(2k+1)!}{k! \tau^{2k+1}} \sum_{i=0}^{k} \frac{(-1)^{k-i}}{i!(k-i)!(2k-i+1)} \tau^i t^{2k-i+1} & 0 < t < \tau \\ 1 & t \geq \tau. \end{cases} \tag{4.7}$$

An example of a possible representation of $\bar{y}(t, \tau)$ is shown in Figure 4.1. The smoothness of the transient depends on the value of k.

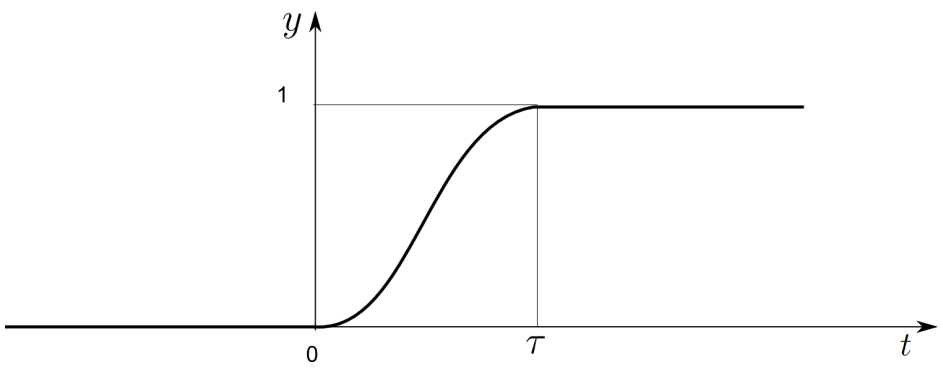

Figure 4.1: Desired output $\bar{y}(t)$

4.1.2 Input-output inversion

Under the assumption of a system with gain equal to 1, assumption that can be done without loss of generality thanks to the properties of linear systems, the system (4.1) can be written as

$$G(s) = \frac{Y(s)}{U(s)} = \frac{\beta_m s^m + \beta_{m-1} s^{m-1} + ... + \beta_1 s + 1}{\alpha_n s^n + \alpha_{n-1} s^{n-1} + ... + \alpha_1 s + 1}. \tag{4.8}$$

Therefore, knowing the form of the output in (4.7) and with the model in (4.8), the desired input can be obtained by inverting (4.8) as

$$U(s,\tau) = G^{-}1(s)\bar{Y}(s,\tau) \tag{4.9}$$

By polynomial division transfer function division it is

$$G^{-1}(s) = \gamma_\rho s^\rho + \gamma_{\rho-1} s^{\rho-1} + ... + \gamma_1 s + \gamma_0 + H_0(s) \tag{4.10}$$

where

$$H_0(s) = \frac{\delta_{0,m-1} s^{m-1} + \delta_{0,m-2} s^{m-2} + ... + \delta_{0,0}}{\beta_m s^m + \beta_{m-1} s^{m-1} + ... + \beta_1 s + 1} \tag{4.11}$$

is the zero dynamics of the system, which is strictly proper.

Defining $\eta_0(t) = L^{-1}[H_0(s)]$ the impulse response of the system, from (4.9) and (4.10), the following Proposition can be demonstrated [22].

Proposition 4 *Consider $y(t,\tau)$ defined by (4.7). Provided that $k \geq \rho - 1$ then*

$$\begin{aligned} u(t,\tau) =& \gamma_\rho D^\rho y(t,\tau) + \gamma_{\rho-1} D^{\rho-1} y(t,\tau) + ... + \gamma_0 y(t,\tau) \\ &+ \int_0^t \eta_0(t-\upsilon) y(\upsilon,t) d\upsilon, t \geq 0. \end{aligned} \tag{4.12}$$

holds.

Therefore, the input corresponding to the desired output can be calculated by a sum of the derivatives of the output multiplied by the coefficients obtained by polynomial division in Equation (4.10), plus the integral of the zero dynamics.

Even if other choices are possible for the output function, a polynomial function like the one in equation (4.7) can be easily derived, and the form of its derivatives is

$$D^{\alpha}\bar{y}(t,\tau) = \begin{cases} \frac{(2k+1)!}{k!\tau^{2k+1}} \sum_{i=0}^{k} \frac{(-1)^{k-i}\tau^{i}(2k-i+1)}{i!(k-i)!(2k-i+1)(2k-i+1-\alpha)!} \tau^{i} t^{2k-i+1-\alpha} & 0 < t < \tau \\ 0 & ELSEWHERE \end{cases} \tag{4.13}$$

Moreover, the form of the desired output can be further simplified in the case of low-damped systems [20]. In those cases, where the process dynamics is dominant with respect to the zero dynamics, the zero dynamics can be neglected and the desired output does not contain an integral that would cause a post-action. This simplification is applicable in the case of industrial cranes where the zeroes due to the friction on the cables occurs at a much higher frequency with respect to the poles of the system. The absence of an integral part on the output function also means that no post-action is required, that means that the control task ends with the end of the load's movement, simplifying the applicability of this technique on off-the-shelf industrial components.

4.2 I/O inversion of crane dynamics

Following the method mathematically described in Chapter 4.1, the dynamics of the crane will now be inverted in order to find an appropriate input function for residual oscillation free motion. A number of different approaches can be chosen for the inversion. In particular, under the assumption of perfect tracking on cart motion, the transfer function between the position (velocity) of the cart and the position (velocity) of the payload (2.88) and (2.95) can be

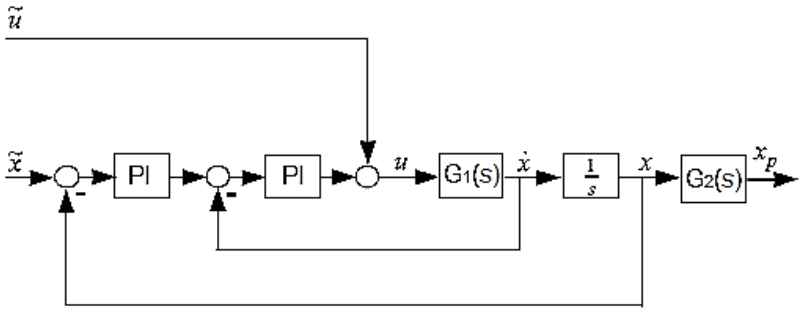

Figure 4.2: Control scheme for position control with force feedforward.

inverted and obtaining the trajectory of the cart. When a perfect tracking is not possible, that is in all real systems, a solution that helps during the tracking of the trajectory found is the inversion of the transfer function between the force to be applied to the crane and the position of the cart (2.87) and (2.93). Once the torque corresponding to the desired trajectory of the cart has been found, it can be given as a feedforward torque signal to the motors.

Thanks to the low values of C_1 and C_2, for control purposes the system will be considered as an undamped one, avoiding the explicit calculation of the convolution of the zero dynamics and the post action, as said in Chapter 4.1.2.

In Figure 4.2 the position control scheme used for the control of he overhead crane is presented, with the feedforward force signal.

In Figure 4.3 the velocity control scheme used for the control of he overhead crane is presented, with the feedforward force signal. In both the schemes $G_1(s)$ is the transfer function between the force applied to the cart and the velocity of the cart, while $G_2(s)$ is the transfer function between the velocity (position) of the cart and the velocity (position) of the payload.

4.2.1 Simple pendulum

Here the control laws necessary for the control of a simple pendulum system will be calculated. As the motion of a crane can be controlled in both velocity

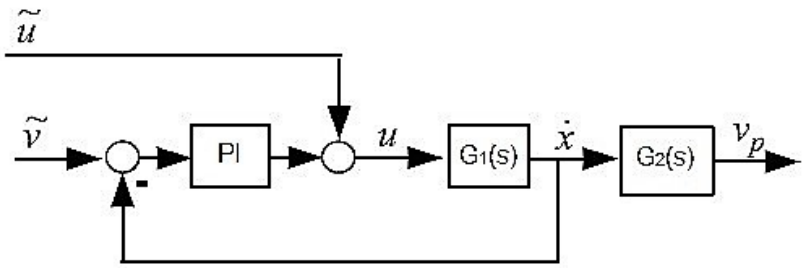

Figure 4.3: Control scheme for velocity control with force feedforward.

and position, two different inversions can be made: the first one between the velocity of the cart and the velocity of the payload and the second one between position of the cart and the position of the payload.

Velocity control

First, the velocity law of the cart will be explicitly found in order to obtain an oscillation-free velocity of the payload in a time τ. Then the corresponding torque to be applied will be calculated, in order to provide a feed-forward to the motor. Then the polynomial corresponding to the oscillation-free movement of the payload from a point to another will be found and inverted.

The first law found is the cart velocity with respect to a desired payload output velocity. By inverting (2.88) we obtain

$$G_{inv} = \frac{1}{g}s^2 + \frac{C_1}{gm_1l_1^2}s + 1 \tag{4.14}$$

, while (4.12) and (4.13) for the case of simple pendulum gives

$$V_P(\tau, q, t) = \frac{6q}{\tau^5}t^5 - \frac{15q}{\tau^4}t^4 + \frac{10q}{\tau^3}t^3 \tag{4.15}$$

Choosing $k = 2$, that is the lowest value possible in order to guarantee a form of the velocity of class C^0, the form of the velocity of the cart is given by

$$V_c(t) = \frac{1}{g}V_P^{(2)}(\tau, q, t) + \frac{C_1}{gm_1l_1^2}V_P(\tau, q, t) + 1 \tag{4.16}$$

where q and τ are respectively the desired final velocity and the transient time to reach that velocity, the only two free parameters of the polynomial law.

In order to find the feedforward expression for the force, equation (2.90) has to be derived (adding s to the numerator) and then inverted, obtaining

$$\begin{aligned} G_{inv} =& \frac{m_C}{g}s^3 + \frac{C_C m_1 {l_1}^2 + C_1 m_1 + C_1 m_C}{g{l_1}^2 m_1}s^2 + \\ & \frac{g{l_1}^2 {m_1}^2 + g m_C {l_1}^2 m_1 + C_1 C_C}{g{l_1}^2 m_1}s + C_C \end{aligned} \tag{4.17}$$

Then, following the steps seen in the previous passage, the polynomial of the torque is given by

$$\begin{aligned} F_v(t) =& \frac{m_C}{g}V_P^{(3)}(\tau, q, t) + \frac{C_C m_1 {l_1}^2 + C_1 m_1 + C_1 m_C}{g{l_1}^2 m_1}V_P^{(2)}(\tau, q, t) + \\ & \frac{g{l_1}^2 {m_1}^2 + g m_C {l_1}^2 m_1 + C_1 C_C}{g{l_1}^2 m_1}V_P^{(1)}(\tau, q, t) + C_C V_P(\tau, q, t) \end{aligned} \tag{4.18}$$

While with equation (4.16) it is possible to move the cart in order to have a residual oscillations free movement of the payload, equation (4.18) gives the form of the theoretical force to be applied to the cart in order to obtain the velocity shape in (4.16), to be added as a feedforward signal directly to the motor responsible for the movement of the cart. This solution, in all the cases when it is implementable, guarantees improved tracking of the trajectory, with the result of lower residual oscillations of the load.

Position control

It is also possible to control the cart in position, this time using the parameters q and τ as the desired final position and the transient time. As the transfer function (2.90) identifies both the relation between cart and payload positions and velocities, the inverse of the transfer function will also be the same. The form of the polynomial that describes the trajectory of the cart can be calculated by (2.90) and (4.12), setting the value of $k = 3$, that is the lowest value that guarantees the trajectory to be C^1. The obtained polynomial trajectory of the payload has the form

$$X_P(\tau, q, t) = -\frac{20q}{\tau^7}t^7 + \frac{70q}{\tau^6}t^6 - \frac{84q}{\tau^5}t^5 + \frac{35q}{\tau^4}t^4 \tag{4.19}$$

The resulting trajectory to be followed by the cart can be therefore written as

$$X_c(t) = \frac{1}{g}X_P^{(2)}(\tau, q, t) + \frac{C_1}{gm_1 l_1^2}X_P(\tau, q, t) + 1 \tag{4.20}$$

The corresponding force feed-forward signal can be calculated by inverting (2.90), obtaining the polynomial

$$\begin{aligned} F_x(t) =& \frac{{l_1}^4 {m_1}^2 m_C}{g} X_P^{(4)}(\tau, q, t) + \\ & \frac{{l_1}^2 m_1 \left(C_C m_1 {l_1}^2 + C_1 m_1 + C_1 m_C\right)}{g} X_P^{(3)}(\tau, q, t) + \\ & \frac{{l_1}^2 m_1 \left(g {l_1}^2 {m_1}^2 + g m_C {l_1}^2 m_1 + C_1 C_C\right)}{g} {X_P}^{(2)}(\tau, q, t) + \\ & C_C {l_1}^4 {m_1}^2 {X_P}^{(1)}(\tau, q, t) \end{aligned} \tag{4.21}$$

4.2.2 Double pendulum

As seen for the case of single pendulum model, here too two controls are possible: velocity and position.

Velocity control

Following the same steps of the previous chapters, the analytical form of the trajectories for both velocity and position control can be found. For the sake of brevity, the explicit polynomials will not be reported here, but they will be expressed instead as functions of the derivatives of the trajectory of the payload defined by equation (4.7).

Given equation (2.97) and setting $k = 4$ in (4.7), the inverse of the transfer function between velocity of the cart and velocity of the payload is

$$G_{inv} = P_1 s^4 + P_2 s^3 + P_3 s^2 + P_4 s + P_5 \tag{4.22}$$

where

$$
\begin{aligned}
P_1 =& \frac{l_1 l_2 m_1}{g^2(m_1+m_2)} \\
P_2 =& \frac{C_2 {l_1}^3 m_1 + C_1 {l_2}^3 m_2 + C_2 {l_1}^3 m_2}{g^2 {l_1}^2 {l_2}^2 m_2(m_1+m_2)} \\
P_3 =& \frac{g {l_1}^3 {l_2}^2 {m_2}^2 + g m_1 {l_1}^3 {l_2}^2 m_2 + g {l_1}^2 {l_2}^3 {m_2}^2 + g m_1 {l_1}^2 {l_2}^3 m_2 + C_1 C_2}{g^2 {l_1}^2 {l_2}^2 m_2(m_1+m_2)} \\
P_4 =& \frac{C_2 g {l_1}^2 m_1 + C_1 g {l_2}^2 m_2 + C_2 g {l_1}^2 m_2}{g^2 {l_1}^2 {l_2}^2 m_2(m_1+m_2)} \\
P_5 =& \frac{g^2 {l_1}^2 {l_2}^2 {m_2}^2 + m_1 g^2 {l_1}^2 {l_2}^2 m_2}{g^2 {l_1}^2 {l_2}^2 m_2(m_1+m_2)}
\end{aligned}
$$

and the desired velocity profile results

$$
V_P(\tau, q, t) = \frac{70q}{\tau^9} t^9 - \frac{315q}{\tau^8} t^8 + \frac{540q}{\tau^7} t^7 - \frac{420q}{\tau^6} t^6 + \frac{126q}{\tau^5} t^5 \tag{4.23}
$$

From (4.22) and (4.23), the function of the cart velocity in order to reach a velocity q in a time τ is

$$
\begin{aligned}
V_c(t) =& P_1 V_P^{(4)}(\tau, q, t) + P_2 V_P^{(3)}(\tau, q, t) + P_3 {V_P}^{(2)}(\tau, q, t) + \\
& P_4 {V_P}^{(1)}(\tau, q, t) + P_5 V_P(\tau, q, t)
\end{aligned} \tag{4.24}
$$

where

$$
\begin{aligned}
P_1 =& \frac{l_1 l_2 m_1}{g^2(m_1+m_2)} \\
P_2 =& \frac{C_2 {l_1}^3 m_1 + C_1 {l_2}^3 m_2 + C_2 {l_1}^3 m_2}{g^2 {l_1}^2 {l_2}^2 m_2(m_1+m_2)} \\
P_3 =& \frac{g {l_1}^3 {l_2}^2 {m_2}^2 + g m_1 {l_1}^3 {l_2}^2 m_2 + g {l_1}^2 {l_2}^3 {m_2}^2 + g m_1 {l_1}^2 {l_2}^3 m_2 + C_1 C_2}{g^2 {l_1}^2 {l_2}^2 m_2(m_1+m_2)} \\
P_4 =& \frac{C_2 g {l_1}^2 m_1 + C_1 g {l_2}^2 m_2 + C_2 g {l_1}^2 m_2}{g^2 {l_1}^2 {l_2}^2 m_2\,(m_1+m_2)} \\
P_5 =& \frac{g^2 {l_1}^2 {l_2}^2 {m_2}^2 + m_1 g^2 {l_1}^2 {l_2}^2 m_2}{g^2 {l_1}^2 {l_2}^2 m_2(m_1+m_2)}
\end{aligned}
$$

In the same way, by inverting the derivative of equation (2.96), the polynomial expression of the feedforward force corresponding to (4.24) is given by

$$
F_v(s) = \frac{1}{g^2}(P_1 s^5 + P_2 s^4 + P_3 s^3 + P_4 s^2 + P_5 s + P_6) \tag{4.25}
$$

where

$$
\begin{aligned}
P_1 =& {l_1}^5 {l_2}^5 m_1 {m_2}^3 m_C \\
P_2 =& {l_1}^2 {l_2}^2 {m_2}^2 (C_1 {l_2}^3 m_1 m_2 + C_2 {l_1}^3 m_1 m_C + C_1 {l_2}^3 m_2 m_C + \\
& C_2 {l_1}^3 m_2 m_C + C_C {l_1}^3 {l_2}^3 m_1 m_2) \\
P_3 =& {l_1}^2 {l_2}^2 {m_2}^2 (g m_C {l_1}^3 {l_2}^2 m_1 m_2 + g m_C {l_1}^3 {l_2}^2 {m_2}^2 + C_2 C_C {l_1}^3 m_1 + \\
& C_2 C_C {l_1}^3 m_2 + g {l_1}^2 {l_2}^3 {m_1}^2 m_2 + g {l_1}^2 {l_2}^3 m_1 {m_2}^2 + g m_C {l_1}^2 {l_2}^3 m_1 m_2 + \\
& g m_C {l_1}^2 {l_2}^3 {m_2}^2 + C_1 C_C {l_2}^3 m_2 + C_1 C_2 m_1 + C_1 C_2 m_2 + C_1 C_2 m_C) \\
P_4 =& {l_1}^2 {l_2}^2 {m_2}^2 (C_C g {l_1}^3 {l_2}^2 m_1 m_2 + C_C g {l_1}^3 {l_2}^2 {m_2}^2 + C_C g {l_1}^2 {l_2}^3 m_1 m_2 + \\
& C_C g {l_1}^2 {l_2}^3 {m_2}^2 + C_2 g {l_1}^2 {m_1}^2 + 2 C_2 g {l_1}^2 m_1 m_2 + C_2 g m_C {l_1}^2 m_1 + \\
& C_2 g {l_1}^2 {m_2}^2 + C_2 g m_C {l_1}^2 m_2 + C_1 g {l_2}^2 m_1 m_2 + C_1 g {l_2}^2 {m_2}^2 + \\
& C_1 g m_C {l_2}^2 m_2 + C_1 C_2 C_C) \\
P_5 =& {l_1}^2 {l_2}^2 {m_2}^2 (g^2 {l_1}^2 {l_2}^2 {m_1}^2 m_2 + 2 g^2 {l_1}^2 {l_2}^2 m_1 {m_2}^2 + m_C g^2 {l_1}^2 {l_2}^2 m_1 m_2 + \\
& g^2 {l_1}^2 {l_2}^2 {m_2}^3 + m_C g^2 {l_1}^2 {l_2}^2 {m_2}^2 + C_2 C_C g {l_1}^2 m_1 + C_2 C_C g {l_1}^2 m_2 + \\
& C_1 C_C g {l_2}^2 m_2) \\
P_6 =& {l_1}^2 {l_2}^2 {m_2}^2 (C_C g^2 {l_1}^2 {l_2}^2 {m_2}^2 + C_C m_1 g^2 {l_1}^2 {l_2}^2 m_2) + {l_1}^2 {l_2}^2 m_1 m_2
\end{aligned}
$$

The form of the force polynomial in time is given by substituting in (4.25) the various s^n with the derivative of order n of (4.23), that is

$$
\begin{aligned}
F_v(t) =& P_1 V_P^{(5)}(\tau, q, t) + P_2 V_P^{(4)}(\tau, q, t) + P_3 V_P^{(3)}(\tau, q, t) + \\
& P_4 V_P^{(2)}(\tau, q, t) + P_5 V_P^{(1)}(\tau, q, t) + P_6 V_P(\tau, q, t)
\end{aligned}
\tag{4.26}
$$

where $P_1, ..., P_6$ have the same values as in (4.25).

Position control

Setting now $k = 5$ in equation (4.7), that is having a trajectory of the payload described by

$$
\begin{aligned}
X_P(\tau, q, t) =& -\frac{252q}{\tau^{11}} t^{11} + \frac{(1386q)}{\tau^{10}} t^{10} - \frac{3080q}{\tau^9} t^9 + \frac{(3465q)}{\tau^8} t^8 \\
& - \frac{1980q}{\tau^7} t^7 + \frac{(462q)}{\tau^6} t^6
\end{aligned}
\tag{4.27}
$$

and considering (2.97), the trajectory of the cart given the final position q and the transient time τ is given by

$$X_c(s) = P_1 s^4 + P_2 s^3 + P_3 s^2 + P_4 s + P_5 \tag{4.28}$$

where

$$\begin{aligned}
P_1 =& \frac{l_1 l_2 m_1)}{g^2 (m_1 + m_2)} \\
P_2 =& + \frac{C_2 {l_1}^3 m_1 + C_1 {l_2}^3 m_2 + C_2 {l_1}^3 m_2}{g^2 {l_1}^2 {l_2}^2 m_2 (m_1 + m_2)} \\
P_3 =& \frac{g {l_1}^3 {l_2}^2 {m_2}^2 + g m_1 {l_1}^3 {l_2}^2 m_2 + g {l_1}^2 {l_2}^3 {m_2}^2 + g m_1 {l_1}^2 {l_2}^3 m_2 + C_1 C_2}{g^2 {l_1}^2 {l_2}^2 m_2 (m_1 + m_2)} \\
P_4 =& \frac{C_2 g {l_1}^2 m_1 + C_1 g {l_2}^2 m_2 + C_2 g {l_1}^2 m_2}{g^2 {l_1}^2 {l_2}^2 m_2 (m_1 + m_2)} \\
P_5 =& \frac{g^2 {l_1}^2 {l_2}^2 {m_2}^2 + m_1 g^2 {l_1}^2 {l_2}^2 m_2}{g^2 {l_1}^2 {l_2}^2 m_2 (m_1 + m_2)}
\end{aligned}$$

The trajectory of the cart is therefore given by

$$\begin{aligned}
X_c(t) =& P_1 X_P^{(4)}(\tau, q, t) + P_2 X_P^{(3)}(\tau, q, t) + P_3 X_P^{(2)}(\tau, q, t) + \\
& P_4 X_P^{(1)}(\tau, q, t) + P_5 X_P(\tau, q, t)
\end{aligned} \tag{4.29}$$

where $P_1, ..., P_5$ have the same values as in (4.31).

Inverting now equation (2.96) the force to be applied as a feedforward signal to the cart in order to obtain trajectory (4.28) is given by

$$F_c(s) = \frac{1}{g^2 {l_1}^2 {l_2}^2 m_2 (m_1 + m_2)} (P_1 s^6 + P_2 s^5 + P_3 s^4 P_4 s^3 + P_5 s^2 + P_6 s) \tag{4.30}$$

where

$$
\begin{aligned}
P_1 =& {l_1}^3 {l_2}^3 m_2 m_1 m_C \\
P_2 =& C_1 {l_2}^3 m_1 m_2 + C_2 {l_1}^3 m_1 m_C + C_1 {l_2}^3 m_2 m_C + C_2 {l_1}^3 m_2 m_C + C_C {l_1}^3 {l_2}^3 m_1 m_2 \\
P_3 =& g m_C {l_1}^3 {l_2}^2 m_1 m_2 + g m_C {l_1}^3 {l_2}^2 {m_2}^2 + C_2 C_C {l_1}^3 m_1 + C_2 C_C {l_1}^3 m_2 + \\
& g {l_1}^2 {l_2}^3 {m_1}^2 m_2 + g {l_1}^2 {l_2}^3 m_1 {m_2}^2 + g m_C {l_1}^2 {l_2}^3 m_1 m_2 + g m_C {l_1}^2 {l_2}^3 {m_2}^2 + \\
& C_1 C_C {l_2}^3 m_2 + C_1 C_2 m_1 + C_1 C_2 m_2 + C_1 C_2 m_C \\
P_4 =& + C_C g {l_1}^3 {l_2}^2 m_1 m_2 + C_C g {l_1}^3 {l_2}^2 {m_2}^2 + C_C g {l_1}^2 {l_2}^3 m_1 m_2 + C_C g {l_1}^2 {l_2}^3 {m_2}^2 + \\
& C_2 g {l_1}^2 {m_1}^2 + 2 C_2 g {l_1}^2 m_1 m_2 + C_2 g m_C {l_1}^2 m_1 + C_2 g {l_1}^2 {m_2}^2 + C_2 g m_C {l_1}^2 m_2 + \\
& C_1 g {l_2}^2 m_1 m_2 + C_1 g {l_2}^2 {m_2}^2 + C_1 g m_C {l_2}^2 m_2 + C_1 C_2 C_C \\
P_5 =& g^2 {l_1}^2 {l_2}^2 {m_1}^2 m_2 + 2 g^2 {l_1}^2 {l_2}^2 m_1 {m_2}^2 + m_C g^2 {l_1}^2 {l_2}^2 m_1 m_2 + g^2 {l_1}^2 {l_2}^2 {m_2}^3 + \\
& m_C g^2 {l_1}^2 {l_2}^2 {m_2}^2 + C_2 C_C g {l_1}^2 m_1 + C_2 C_C g {l_1}^2 m_2 + C_1 C_C g {l_2}^2 m_2 \\
P_6 =& C_C g^2 {l_1}^2 {l_2}^2 {m_2}^2 + C_C m_1 g^2 {l_1}^2 {l_2}^2 m_2
\end{aligned}
$$

The feedforward force signal corresponding to trajectory (4.27) is therefore given by

$$
\begin{aligned}
F_c(t) =& \frac{1}{g^2 {l_1}^2 {l_2}^2 m_2 \left(m_1 + m_2\right)} (P_1 X_P^{(6)}(\tau, q, t) + P_2 X_P^{(5)}(\tau, q, t) \\
& + P_3 X_P^{(4)}(\tau, q, t) P_4 X_P^{(3)}(\tau, q, t) + P_5 X_P^{(2)}(\tau, q, t) + P_6 X_P^{(1)}(\tau, q, t))
\end{aligned}
\tag{4.31}
$$

Chapter 5

Simulations

In order to prove the performance of the different techniques described in the previous chapters a useful tool is simulation. In this chapter all the techniques will be applied to the control of both simple and double pendulum models built inside Simulink environment thanks to Simscape™ Multibody™, a multibody simulation environment for 3D mechanical systems.

First it will be shown how to model a double pendulum system with the library Simscape Multibody, and the model will be used to show the correctness of the linearized model obtained in Chapter 2. Then the control techniques seen in Chapters 3 and 4 will be used to move the crane and their performance will be compared in terms of residual oscillations and robustness with respect to parameter variations.

Finally, a double pendulum will be controlled with all the techniques

5.1 Simscape™ Multibody™ model

Even if MATLAB® is a useful tool to work with differential equations, like the ones that describe the pendulum dynamics, it is not easy to simulate a generic model with variable inputs. Simulink® is a software, integrated with MATLAB, explicitly designed for simulation purposes, that provides a graphical editor, customizable block libraries, and solvers for modelling and simulating dynamic systems. A useful library for the simulation of mechanical systems is Simscape™ Multibody™, which provides a multibody simulation

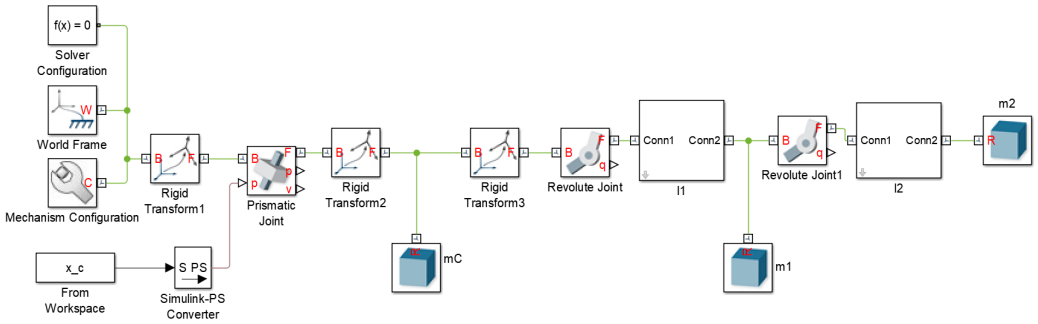

Figure 5.1: Model of a double pendulum on a cart in Simscape™ Multibody™.

environment for 3D mechanical systems.

Simscape™ Multibody™ has been used to model a crane like a double pendulum on a cart, as shown in Figure 5.1. First, it is necessary to insert three blocks:

a World Frame, which define the absolute coordinates of the system

a Solver Configuration block which sets the parameters for the solution of the differential equations related to the model

a Mechanism Configuration block which sets mechanical and simulation parameters that apply to an entire machine, like, for example, the direction and the magnitude of the gravitational field.

Then it is possible to connect to the World Frame a series of blocks like

Rigid Transform which apply a rotation and a translation of coordinates between its input and its output

Prismatic and Revolute Joints which permit the motion of the following parts of the body in a determined direction. Some options allow to control the motion of the joints (like shown in Figure 5.1, where the position of the prismatic joint is controlled through the variable x_c)

Solids which are the only objects to have proprieties like mass and inertia.

The result is the model of a mechanical system described by its geometrical and physical proprieties and, by defining the proprieties of the surrounding environment, it is possible to accurately simulate its behaviour without

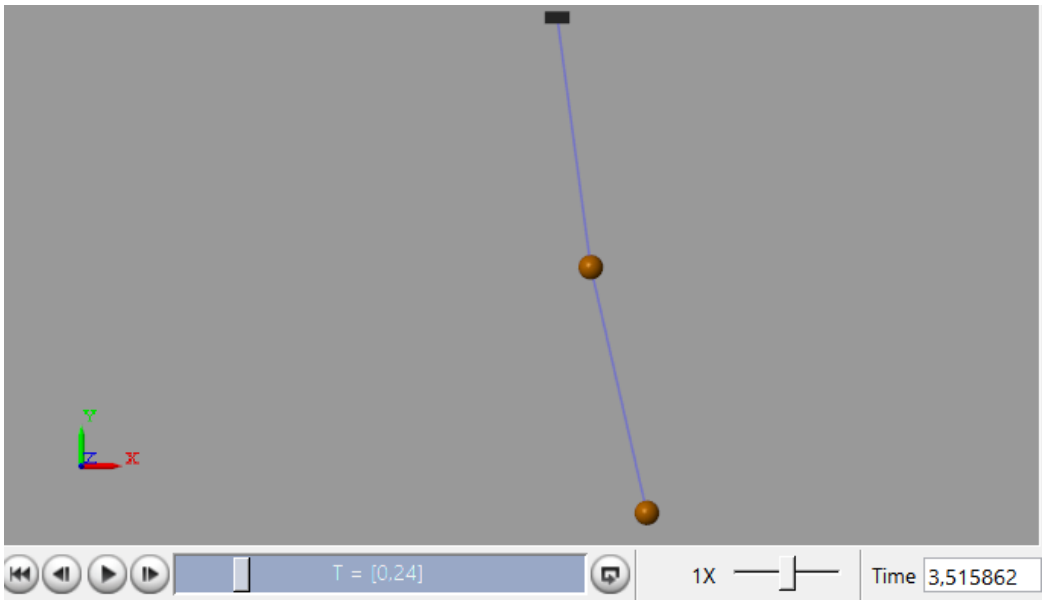

Figure 5.2: Frame of the animation provided by Simscape Multibody simulation.

the need of writing the equations of the dynamics. A useful tool provided by Simscape Multibody is the possibility to see an animation of the system that represent its movement during the simulation. A frame of the animation for the case of the double pendulum is presented in Figure 5.2.

5.2 Validation of the linear model

In this section the linear models of the pendulum, obtained in Chapter 2, will be validated comparing its free dynamics with the nonlinear Simscape model one.

The validation of the linearized model will be done just for the case of the double pendulum. In fact, the double pendulum is the most sensible one with respect to model errors and having a sensitive dependence on initial conditions, being the most simple example of chaotic system. The simple pendulum instead can be linearized obtaining an accurate model for small angles.

To do so, the free evolution of both linearized and Simscape models is

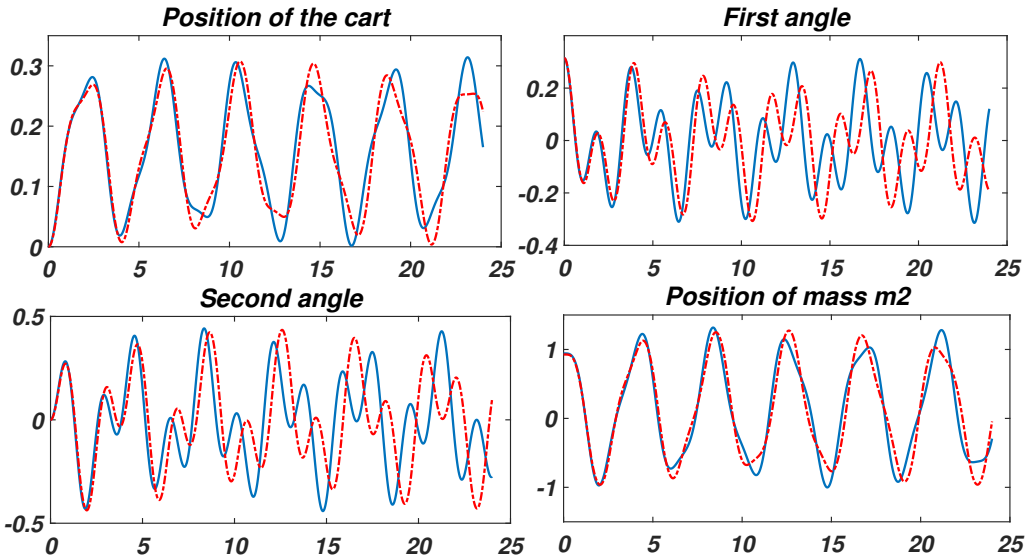

Figure 5.3: Comparison between the free evolution of the complete model (red line) and the linearized one (blue line) in a simulation lasting 25 seconds. Angles are measured in radians, positions in meters.

analyzed giving the same initial conditions, that is,

$$\boldsymbol{x} = \begin{pmatrix} x \\ \theta_1 \\ \theta_2 \end{pmatrix} = \begin{pmatrix} 0.314 \\ 0 \\ 0 \end{pmatrix} \quad , \quad \dot{\boldsymbol{x}} = \begin{pmatrix} \dot{x} \\ \dot{\theta}_1 \\ \dot{\theta}_2 \end{pmatrix} = \begin{pmatrix} 0 \\ 0 \\ 0 \end{pmatrix} \tag{5.1}$$

In particular, the data used for testing the model are shown in Table 5.1.

The results of the simulations are shown in Figure 5.3. It can be seen that the linear model follows the free evolution of the nonlinear model for the first seconds. After a while the errors due to the approximations introduced with the linearization make the evolution of the two systems diverge. It has to be noted that the linearization has low influence on the natural frequencies of the system as the position of m_2 keeps being comparable between the two models. The linearized model can be used for control purposes, but it has to be noted that the use of feedforward techniques, like input shaping and input-output inversion, is highly dependent on the accuracy of the model, so that the differences seen in the comparison of the two models in Figure 5.3 will lead to the presence of small residual oscillations.

Table 5.1: Parameters of the model used in simulations.

Model data	
m_C	100 $[kg]$
m_1	10 $[kg]$
m_2	10 $[kg]$
l_1	3 $[m]$
l_2	3 $[m]$
C_C	0.1 $[\frac{Ns}{m}]$
C_1	3 $[\frac{Nms}{rad}]$
C_2	3 $[\frac{Nms}{rad}]$
ω_1	1.49 $[\frac{rad}{s}]$
ξ_1	0.002
ω_1	3.39 $[\frac{rad}{s}]$
ξ_2	0.004

5.3 IS techniques simulation

As mentioned in Chapter 2 and Chapter 3 all the theory needed for Input Shaping control has been developed. From Chapter 2.3 the natural frequencies and damping coefficients are parametrized and can be used in simulation.

The convolution of a signal with a series of N impulses is equal to the sum of N scaled signals delayed in time. While with off-the-shelf industrial hardware it is hardly probable to have an easy way to implement a convolution between signals, to scale and delay a signal is a basic task. Instead of using the convolution block, available in Simulink, for IS technique a series of delay and gain blocks has been used. The input signal is elaborated in two blocks (Figure 5.4): each block scale and delay the signal according to the corresponding natural frequency ω_n and damping coefficient ξ. The structure of the blocks depend on the kind of input shaping technique used, but the basic idea is the same. The blocks receive in input the damped periods of the system and its damping coefficients and elaborate the input signal accordingly to the chosen technique. In Figure 5.5 the implementation of ZV technique is shown. First, coefficient K is calculated accordingly to equation

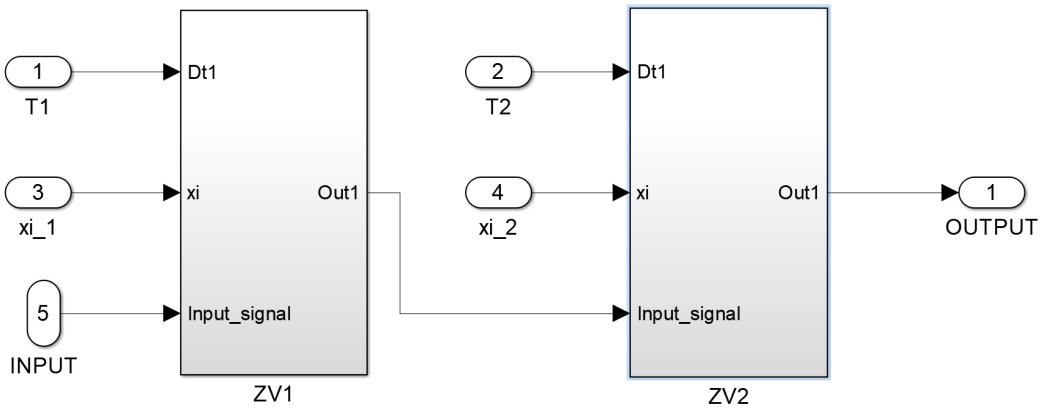

Figure 5.4: Subsystem used to shape the input signal of the System.

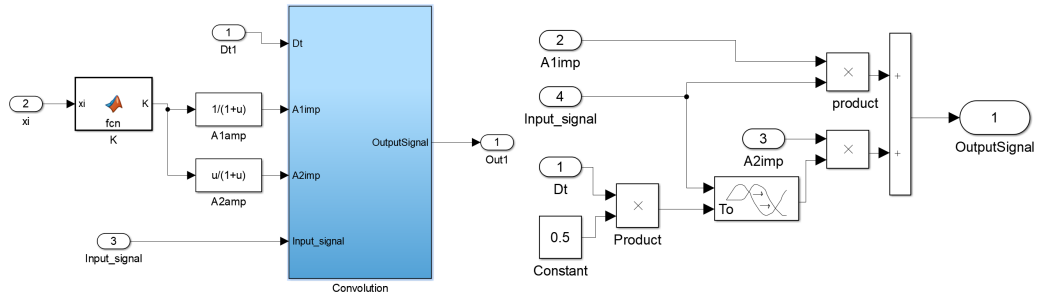

(a) Calculation of K, A_1 and A_2.

(b) Scaling and delaying of the signal.

Figure 5.5: Implementation of ZV IS for a single frequency.

(3.12) and the amplitude of the two impulses is calculated following equation (3.11) (Figure 5.5a). Then, inside the block named as *convolution* (Figure 5.5b), the signal is scaled and delayed. This process is repeated on two different stages, one for each frequency of the system. The implementation of the other techniques follows the same scheme, changing the calculation of amplitudes and delays.

Depending on how the cart is controlled, the driving signal can be both a velocity ramp or a position setpoint to be reached. Typically, in order not to stress the mechanical of real systems, the input signal is built through a series of ramps that, in the case of position control, have to be filtered in order to obtain a non-impulsive acceleration profile.

In Figure 5.6 a comparison between IS techniques is made through simulation. A position reference, corresponding to a ramp going from a null position to 3 $[m]$ in 0.5 $[s]$, is given as an input to the cart. The input is manipulated by IS blocks and it is given to the Simscape Multibody model. The position of the payload is than calculated, plotted and compared to the position of the cart in order to check the magnitude of residual oscillations. The figure shows that IS techniques reduces the residual oscillations, that are not greater than 0.05 $[m]$, while the oscillations corresponding to the non-shaped input exceed the 3 $[m]$. It can be observed how performance in terms of oscillation reduction increases with the total transient time of the technique for ZV techniques. With EI techniques, even if transient times are equal to the ones of ZVD and ZVDD, the performance in terms of oscillations reduction is reduced, as they allow an oscillation up to 5% of the unshaped case. Anyway, as demonstrated in Chapter 5.5, EI shapers are more robust than ZV ones.

Usually, on industrial environments, overhead cranes are manually controlled by the operator in velocity, and not in position. When the operator pushes the command button, the cart starts accelerating until it reaches a predetermined velocity and keeps moving until the command button is released. It is thereby interesting to simulate the performance of Input Shaping techniques also with velocity controls.

The most common velocity profile used for the control of industrial mechatronic machines is the trapezoidal one, characterized by an initial phase with

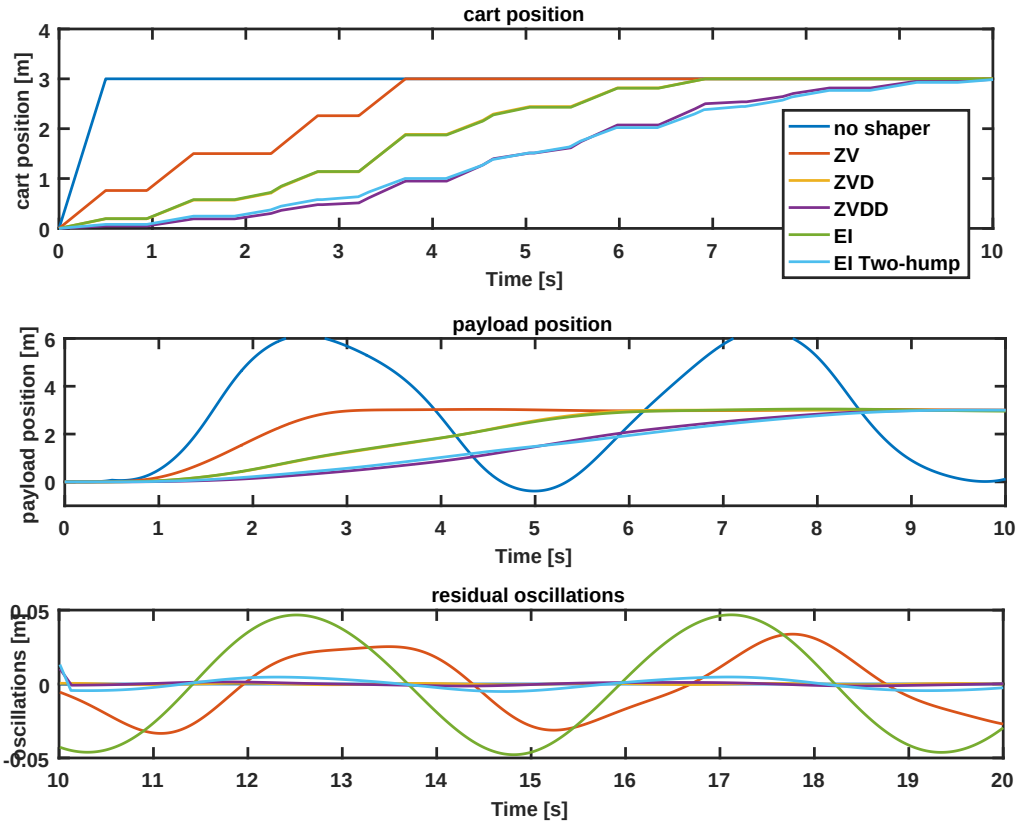

Figure 5.6: Comparison between all IS techniques presented. The top graphic represent the shape of the position reference after the shaping, the graphic at the center the position of the payload and the bottom one the difference between the two graphics, that is the oscillation of the payload with respect to a frame attached to the cart. In the last graph the residual oscillation produced by the unshaped signal is not reported.

constant acceleration, a second phase with constant velocity and a third phase of constant deceleration after which the cart stays put.
In order to check the entity of the oscillations in simulation the difference between the position of the cart and the position of mass m_2 has been made.

The results of velocity control simulations are shown in Figure 5.7

5.4 Input-output inversion technique simulation

It has been also possible to test input-output inversion technique through simulation. In this chapter the passages followed for the simulation of input-output inversion control on a double pendulum will be described. The simulation for the simple pendulum case follows the same scheme.

First, the state space matrices $\mathcal{A}$ and $\mathcal{B}$ are built according to (2.57) and (2.58). Then, by changing the matrix $\mathcal{C}$, the transfer functions described in Chapter 2.4.2 are found. The form of the desired polynomial is symbolically written as in equation (4.6), as well as its derivatives of order α (equation (4.13)).

The desired transfer function (depending on the kind of control desired, in position or velocity) is inverted and expressed as a polynomial in s plus a transfer function representing the zero-dynamics of the system. The zero-dynamics of the system is ignored because its contribute is negligible if the system is lowly damped [20].

Following the passages of Chapter 4.2.2 the trajectory (velocity profile) of the cart and the feedforward force signal are found in the interval $[0, T_f]$ and then extended in $[T_f, \infty]$.

The trajectory (velocity profile) of the cart is then given as input to the model developed in Simscape and the output, corresponding to the horizontal position of the payload, is then analyzed.

An example of the results of a simulation of position control is shown in Figure 5.8, with a total movement time of 5 second, a total displacement of 10 meters and the same model parameters used in the previous chapter. In Figure 5.8a the cart and payload trajectories are plotted. In Figure 5.8b the feed-forward force is reported, and in Figure 5.8c the difference between the theoretical trajectory of the payload and the output of the model is

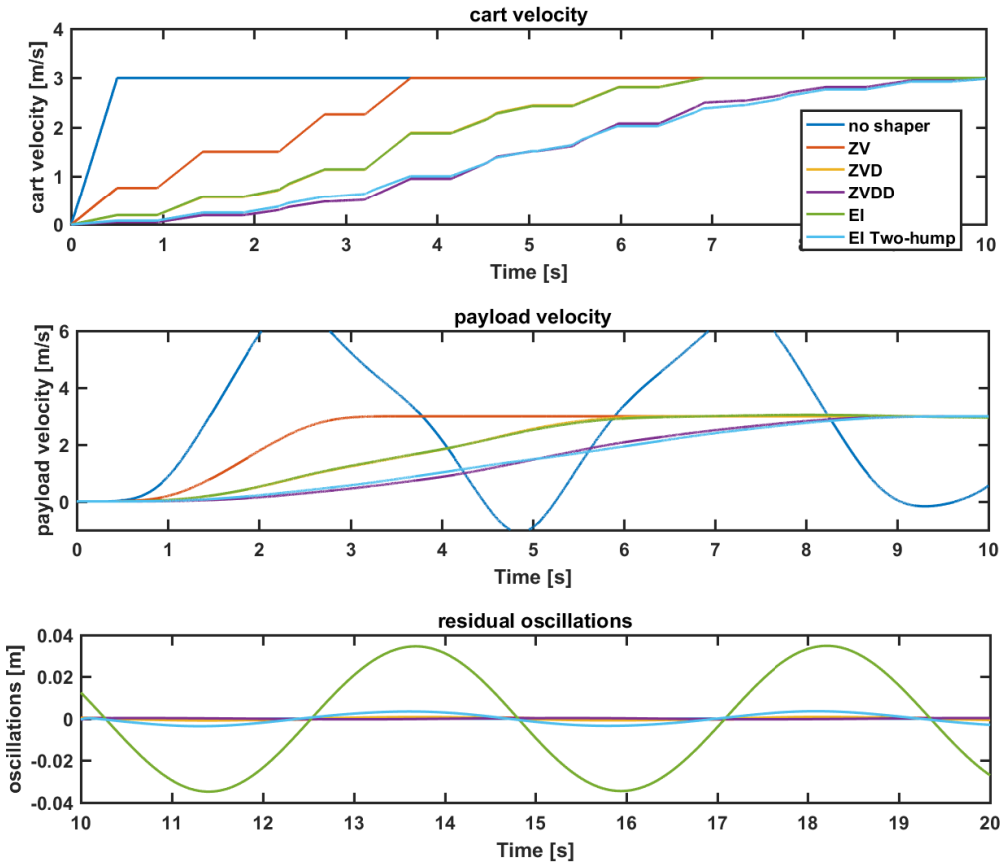

Figure 5.7: Comparison between all IS techniques presented applied to velocity control. The top graphic represent the shape of the velocity reference after the shaping, the graphic at the center the velocity of the payload and the bottom one the difference between the position of the cart and the position of the mass m_2, that is the oscillation of the payload with respect to a frame attached to the cart. In the last graph the residual oscillation produced by the unshaped signal is not reported.

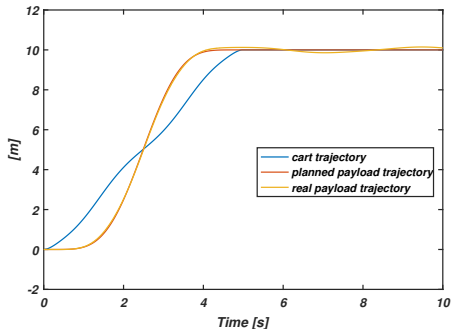

(a) Cart and payload trajectory

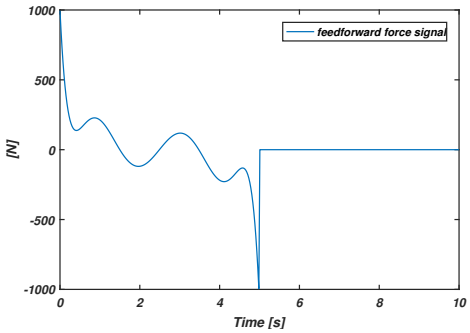

(b) Feedforward force signal

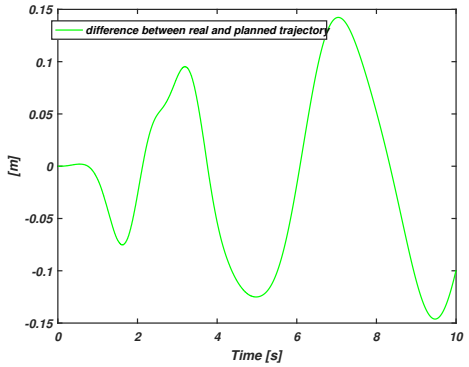

(c) Difference between real and planned trajectory

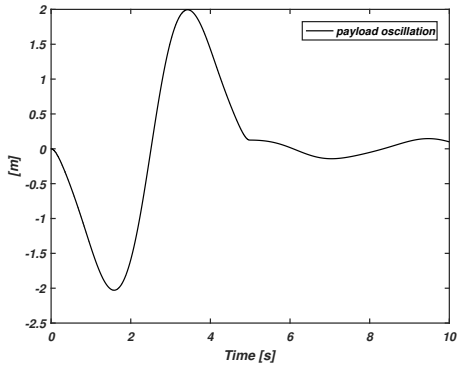

(d) oscillation of the payload with respect to cart position

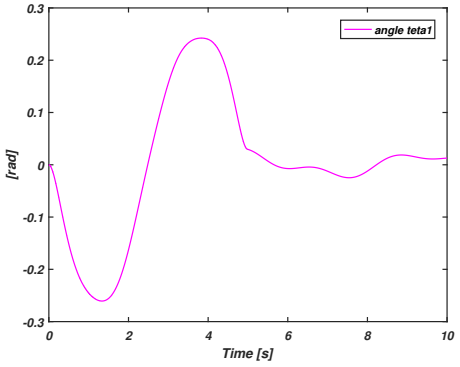

(e) Angle θ_1

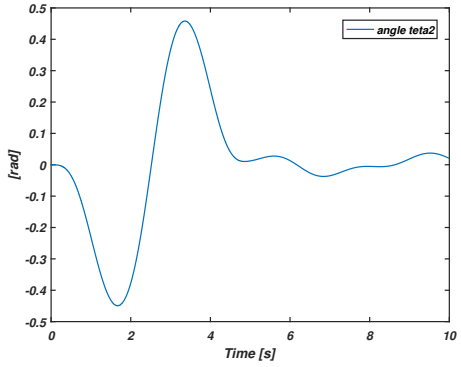

(f) Angle θ_2

Figure 5.8: Simulation of position control using input-output inversion on a double pendulum.

shown. The magnitude of the residual oscillations is comparable with the ones obtained using ZV IS technique, if the transient time τ is set as half of the two periods sum. In Figure 5.8d the oscillation of the payload is reported, calculated as the difference between payload and cart horizontal position. In Figure 5.8e and 5.8f the trajectory of angles θ_1 and θ_2 is shown.

In Figure 5.9 the results of a velocity control simulation example are shown, with a set final velocity of 10 $[m/s]$ and a transient time of 5 $[s]$.

The script used to inverse the dynamics is reported in appendix.

5.5 Robustness of the techniques to parameters variation

The most important drawback of feedforward control techniques is their strong dependence on the accuracy of the model of the system on which they are based. In fact, IS technique filter the input based on the natural frequency and the damping of the system. These parameters are not always available with the desired precision, and they can change, and not only between a movement and the other (for example thanks to a change in the mass of the payload), but also during a single movement, for example in the case of the crane when the payload is lifted. Input-output technique is strongly dependant on the system as it explicitly invert the model mathematical description.

It is therefore utterly important to check how these techniques vary their response when model parameters change, such as variation in payload mass and cable length, that are the variables that are are most likely to change in an industrial crane.

In this chapter only results for the double pendulum case will be reported, for the robustness of this techniques in the case of simple pendulum has already been studied in many publications (e.g. [33]).

In order to test the robustness of the techniques a series of simulations for every technique has been executed. In particular, starting from the values listed on the table in Chapter 5.2, the values of l_1 and m_2 have been varied on a linear grid, varying l_1 in the interval $[1.2, 6]$ meters every 0.6 $[m]$ and m_2

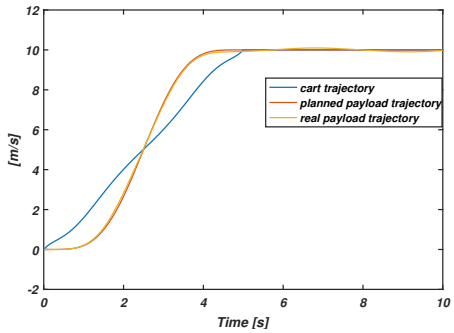

(a) Cart and payload velocity profiles

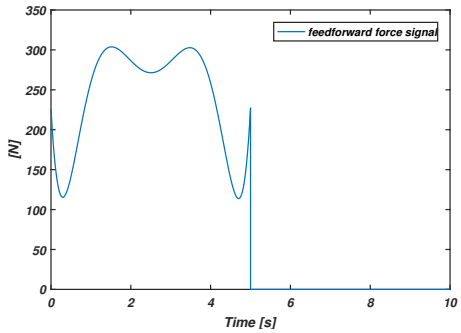

(b) Feedforward force signal

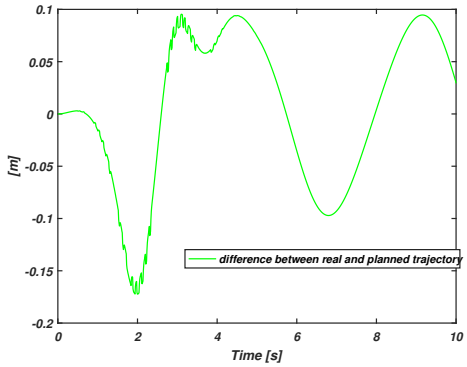

(c) Difference between real and planned velocity profiles

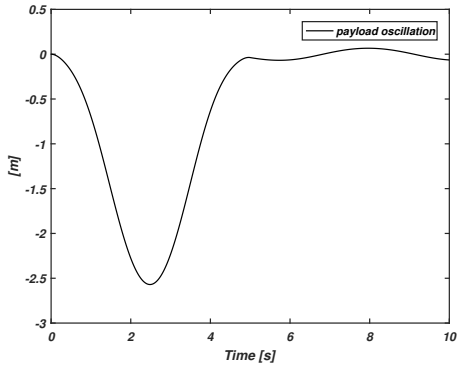

(d) oscillation of the payload with respect to cart position

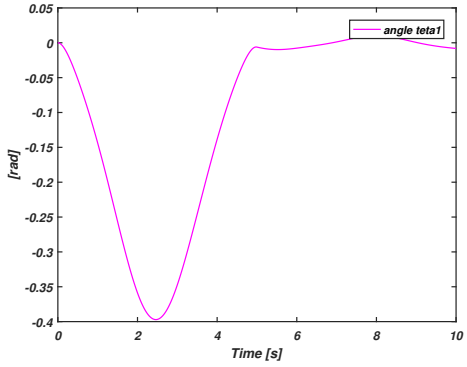

(e) Angle θ_1

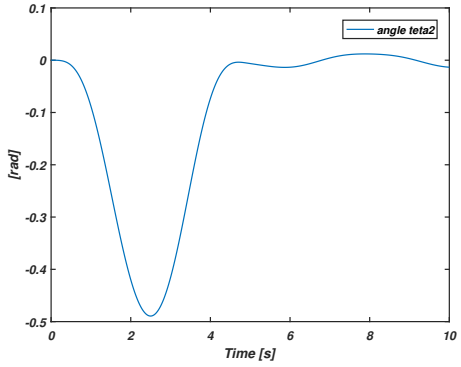

(f) Angle θ_2

Figure 5.9: Simulation of velocity control using input-output inversion on a double pendulum.

in the interval $[4, 20]$ kilograms with steps of 1 $[kg]$. The entity of residual oscillations has been measured by checking the maximum horizontal distance of the payload from the position of the cart over a sufficiently long period of time after the transient of the cart was ended. In this way, the oscillation can be measured both in position and velocity control mode. The maximum oscillation has been saved for every simulation and then plotted in order to compare the robustness of the different techniques.

The surfaces representing the robustness of the techniques are shown in Figure 5.10. The robustness of the techniques does not change between position (left graphs) and velocity (right graphs) control. The graphs have been grouped in order to have all the techniques that requires the same amount of transient time together. Input-output inversion technique transient time has been scaled in order to be comparable with input shaping techniques.

For a transient time of $\frac{T_1 + T_2}{2}$, where T_1 and T_2 are the damped periods of the system, input-output inversion techniques is slightly more robust than IS, and ensures a better performance in the case of a perfect model too (Figure 5.10a and 5.10b). With a transient time equal to the sum of the two periods, *ZVD* and *EI* techniques are implemented, along with input-output inversion technique (Figure 5.10c and 5.10d). While input-output inversion technique appears to grant better performances when the model is accurate, it is less robust than *ZVD IS* and *Extra-Insensitive IS*. In fact, as expected, *EI* allows small oscillations when the model is perfect, put is the most robust of the techniques. In Figure 5.10e and 5.10f the techniques that introduce a delay equal to 1.5 times the sum of the damped periods are plotted, i.d. *ZVDD* and *EI two-hump*, along with input-output technique with equal transient time. It can be seen that input-output works better than the others when the model is perfect, but its performance rapidly deteriorate with uncertainties in model parameters. *ZVDD* technique shows good performance over a wide range of uncertainties, keeping residual vibrations low. *Two-hump EI* technique appears to be less performing, but this is only due to the allowed oscillations of 5%, that guarantees a robustness over a range that exceed the range of uncertainties simulated, and that could be lowered for this reason to a value of 2%.

During the control of a single movement in industrial cranes it is unlikely

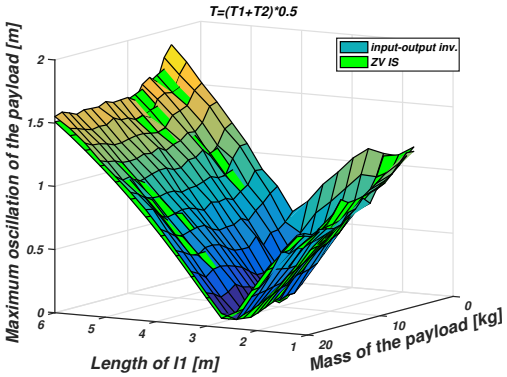

(a) Position control, total time of $\frac{T_1+T_2}{2}$

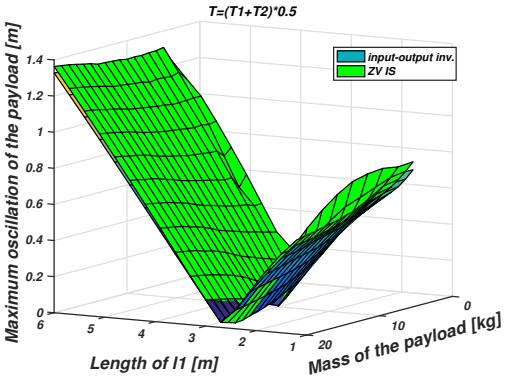

(b) Velocity control, total time of $\frac{T_1+T_2}{2}$

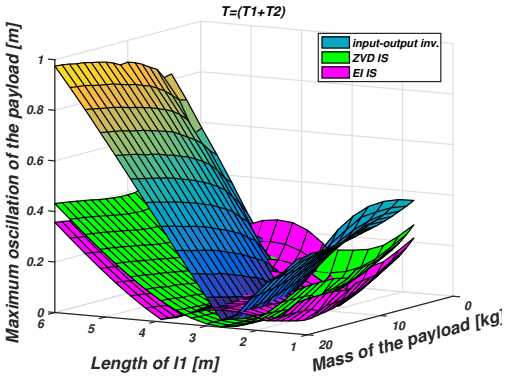

(c) Position control, total time of T_1+T_2

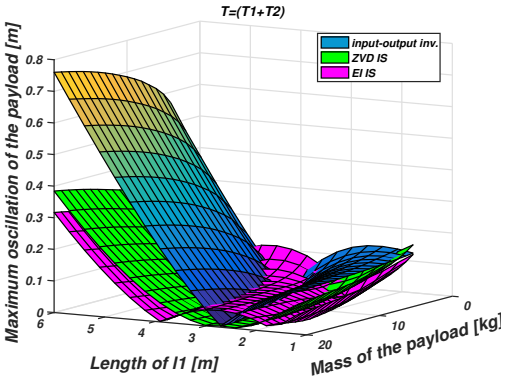

(d) Velocity control, total time of T_1+T_2

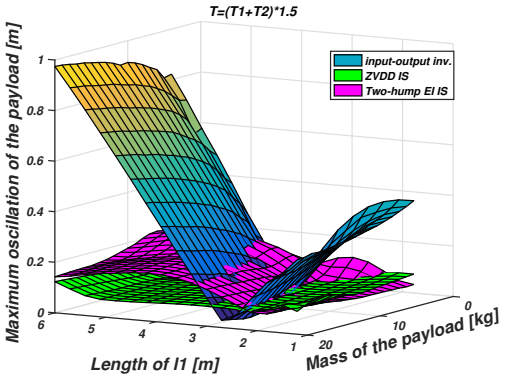

(e) Position control, total time of $\frac{3}{2}(T_1+T_2)$

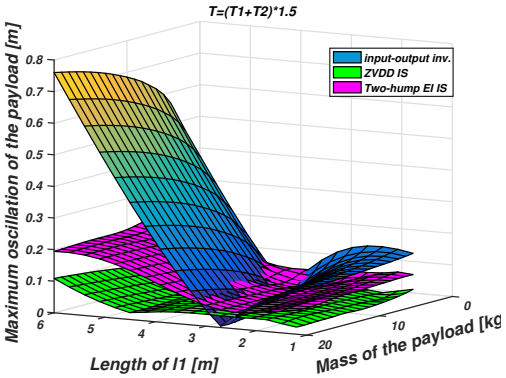

(f) Position control, total time of $\frac{3}{2}(T_1+T_2)$

Figure 5.10: Maximum difference between cart and payload position showing the robustness of various feedforward technique with respect to changes in model parameters. The nominal parameters for which feedforward signals have been built are $l_1 = 3\ [m]$ and $m_2 = 10\ [kg]$.

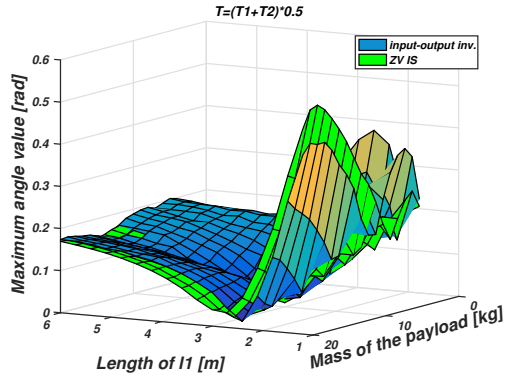

(a) Position control, total time of $\frac{T_1+T_2}{2}$

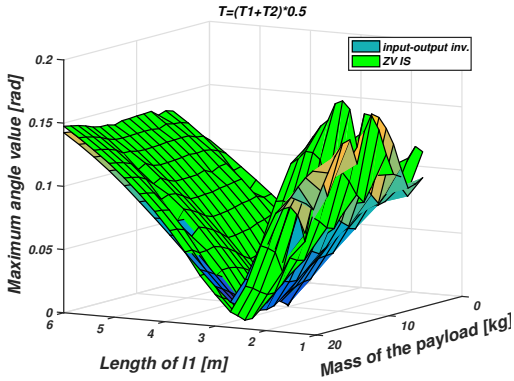

(b) Velocity control, total time of $\frac{T_1+T_2}{2}$

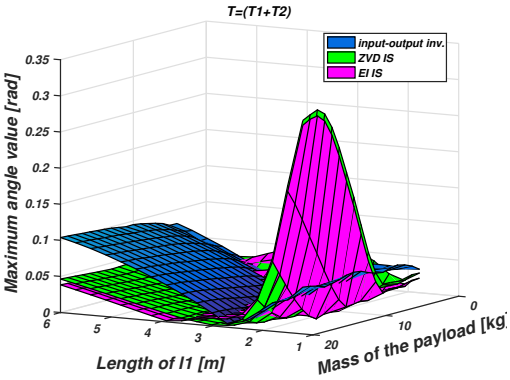

(c) Position control, total time of T_1+T_2

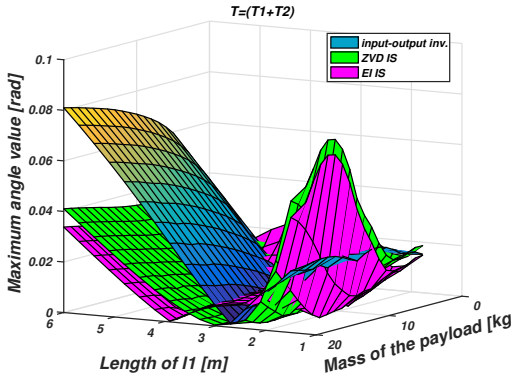

(d) Velocity control, total time of T_1+T_2

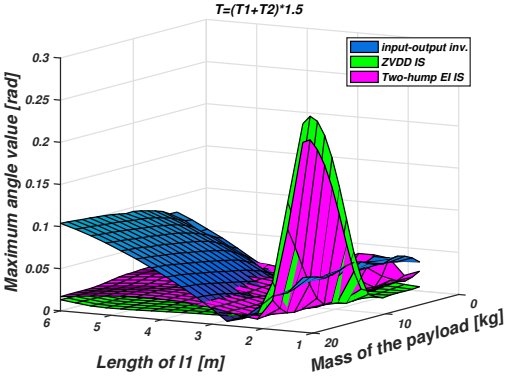

(e) Position control, total time of $\frac{3}{2}(T_1+T_2)$

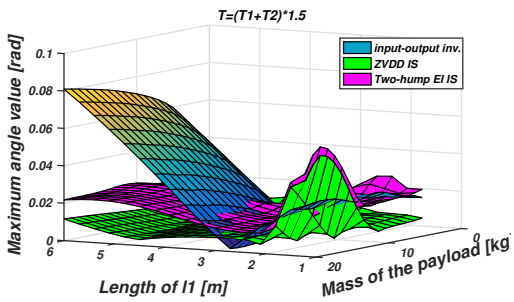

(f) Position control, total time of $\frac{3}{2}(T_1+T_2)$

Figure 5.11: Maximum value of angle θ_1 showing the robustness of various feedforward technique with respect to changes in model parameters. The nominal parameters for which feedforward signals have been built are $l_1 = 3$ $[m]$ and $m_2 = 10$ $[kg]$.

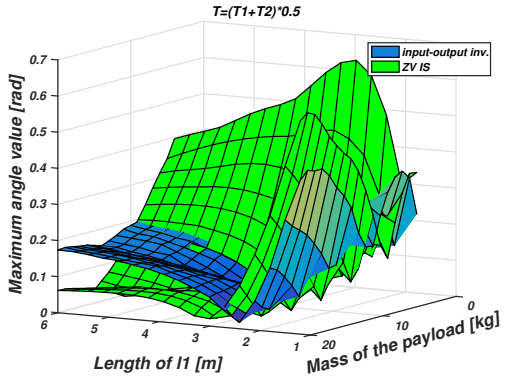

(a) Position control, total time of $\frac{T_1+T_2}{2}$

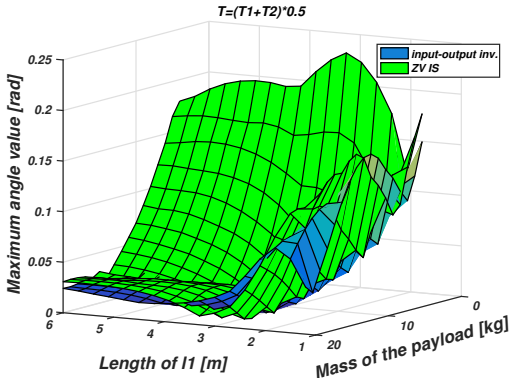

(b) Velocity control, total time of $\frac{T_1+T_2}{2}$

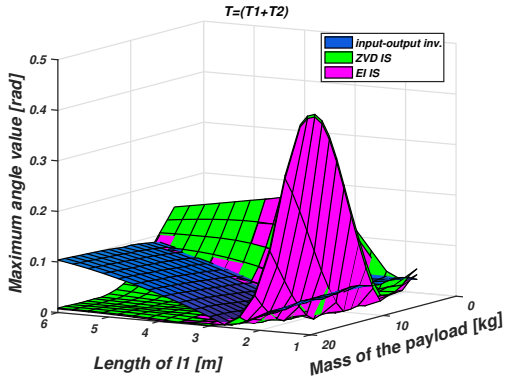

(c) Position control, total time of T_1+T_2

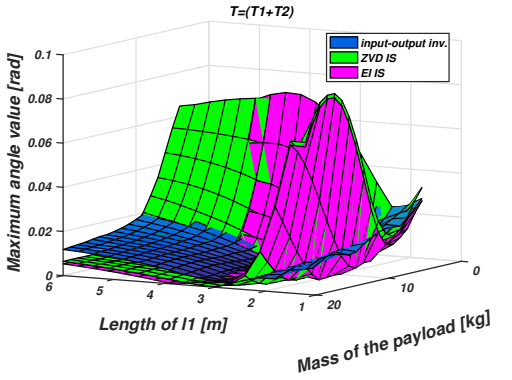

(d) Velocity control, total time of T_1+T_2

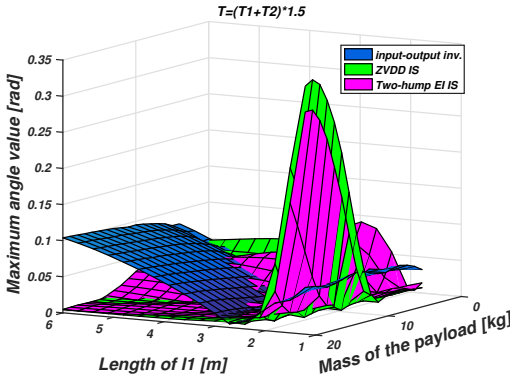

(e) Position control, total time of $\frac{3}{2}(T_1+T_2)$

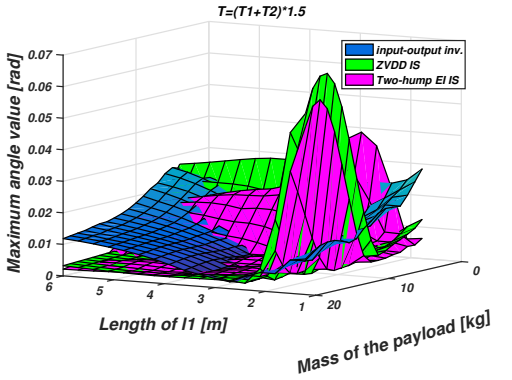

(f) Position control, total time of $\frac{3}{2}(T_1+T_2)$

Figure 5.12: Maximum value of angle θ_2 showing the robustness of various feedforward technique with respect to changes in model parameters. The nominal parameters for which feedforward signals have been built are $l_1 = 3$ $[m]$ and $m_2 = 10$ $[kg]$.

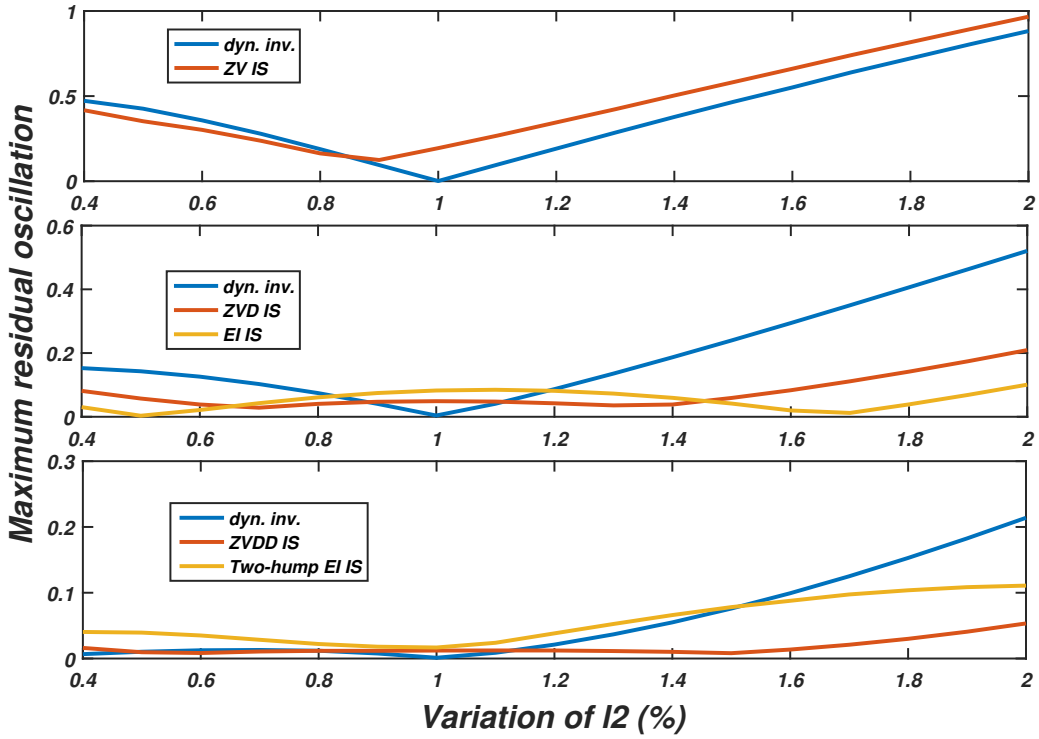

Figure 5.13: Robustness of the implemented techniques with respect to changes in the length of l_2.

for the mass to change, and it has anyway proven (Figure 5.10) that the techniques are generally very robust with respect to payload mass changes. On the other hand, the lifting of the payload is a common maneuver during its movement, and a change of the cable length is more likely to happen. It is therefore interesting to focus on how robust techniques are in the control of industrial cranes with respect to changes in the length l_2. A comparison of this kind of robustness is shown in Figure 5.13.

5.6 Simple VS double pendulum model

For most of the industrial applications, it is enough to model the system as a simple pendulum. This reduces the time spent to build the mathematical model of the crane. In fact, it is enough to measure the length of the cable,

the mass of the payload and the damping ratio of the main oscillation to easily calculate all the variables of a simple pendulum model.

By the way, some applications may require a major suppression of residual oscillations. For example, in the case of repetitive movements such is the case of assembly chains, the variables of the model do not change and it is reasonable to spend a little more time and resources to have a double pendulum model of the system, granting reduced residual oscillations with respect to a simple pendulum model. Moreover, for payloads transported in a assembly chain, CAD models are usually available, and the physical characteristics needed to calculate a more accurate model for the crane are usually retrievable from there.

Other applications for which a double pendulum model can lead to great improvements in terms of increased residual oscillations reduction are all the applications where the payloads have important moment of inertia with respect to an horizontal axis perpendicular to direction of movement of the crane, such is the case of the concrete cylinder used in Chapter 8, and in general all the applications where an hook of non-negligible mass is used.

To justify what is written above, some simulations have been performed in order to prove the differences between simple and double pendulum model-based techniques applied to a system with an hook of non-negligible mass and a payload. The tests have been made on a double pendulum model, with a total mass $m_1 + m_2 = 20$ $[kg]$ and a total length $l_1 + l_2 = 6$ $[m]$. The values of m_1 and l_1 have been varied, keeping total length and mass constant, and input output inversion and ZV input shaping techniques with single and double pendulum models approximations have been tested for both velocity and position control. For the simple pendulum model, the mass of the payload is set equal to the sum of the two masses of hook and payload, that is equal to 20 $[kg]$, while the length of the cable is set equal to the distance between the cart and the center of gravity of the system composed by the hook and the payload.

In Figure 5.14 the results from simulation on velocity and position control with input output inversion technique are reported. For the velocity, a final velocity of 3 $[m/s]$ is set, with a transient time of 6 $[s]$. For position control, a total displacement of 20 $[m]$ is carried out in a total time of 6 $[s]$ with input-

output inversion techniques using both simple and double pendulum models. It can be seen that the improvements introduced by the double pendulum model are significant, in particular when the mass of the hook is greater than the one of the payload and when the distance between hook and cart is smaller than the one between payload and hook. This makes sense, because as the distance between hook and payload increases, the simplification of both as a single mass becomes more and more inaccurate. Moreover, as can be seen in Figure 5.14, when the hook has a mass greater than the payload mass, the accuracy of the simple pendulum model decreases, as the system can not be approximated anymore as a system with a predominant low frequency.

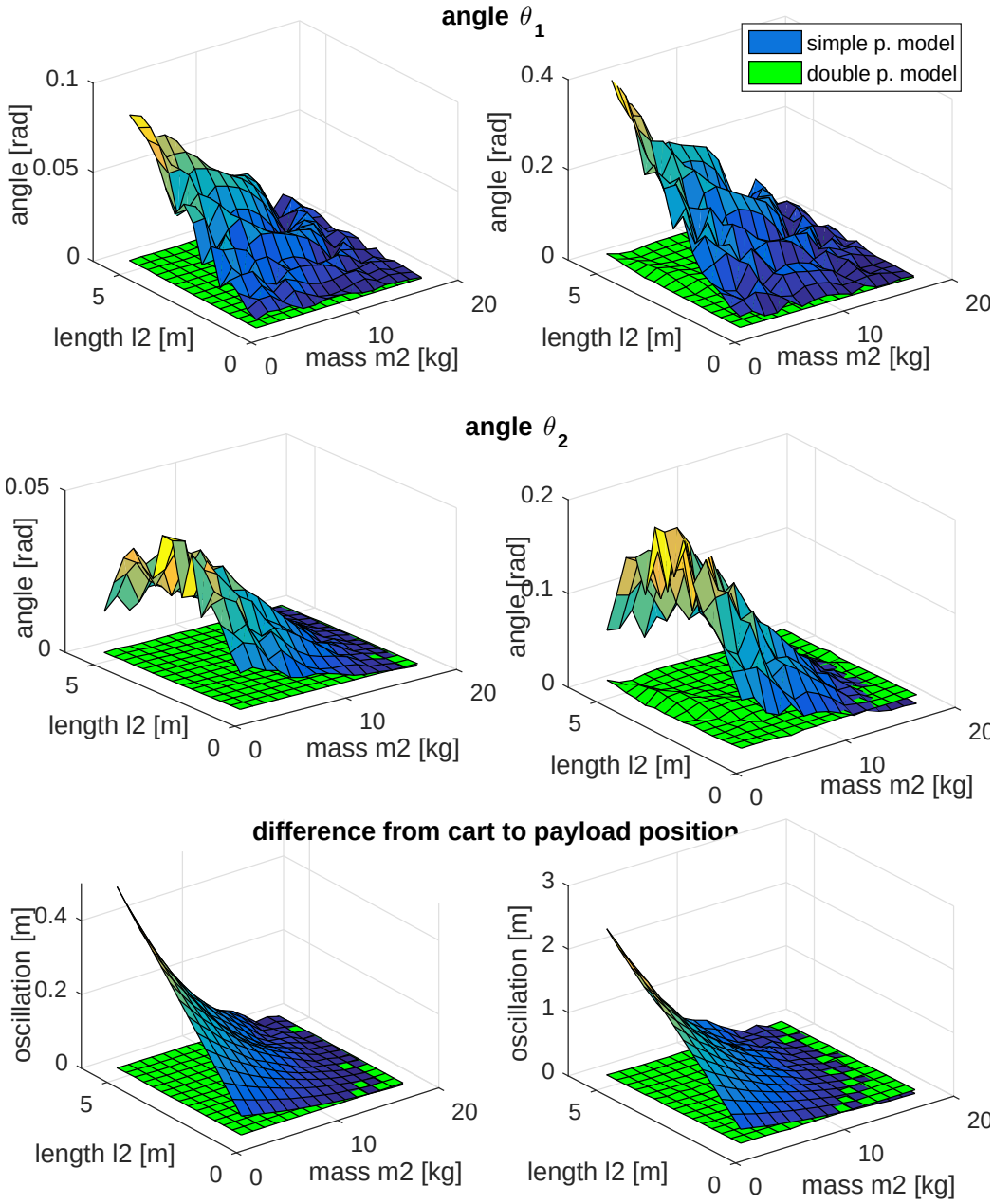

Figure 5.14: Comparison between residual oscillations using simple and double pendulum models in input-output inversion techniques in position (on the left) and velocity (on the right). The first four graphs present the maximum oscillations of angles θ_1 and θ_2, while the latter ones the residual oscillation of mass m_2 calculated as the difference between payload and cart position.

Chapter 6

Experimental set-up

In order to test the techniques developed in the previous chapters on a real system, a scaled model of an industrial overhead crane has been used. In this chapter the whole system will be presented. In Chapter 6.1 the mechanical part will be illustrated. The system is the same developed and used in [26], to which some changes have been made. In particular, a second motor has been added for the lifting of the payload. In order to accentuate the presence of a second way of vibrating the payload has been substituted: instead of the sack used in [26] a cylindrical concrete block has been used. In Chapter 6.2 the off-the-shelf industrial hardware used will be presented, and in Chapter 6.3 a description of the control scheme will be shown.

6.1 Mechanical part and model parameters

The scaled model of an industrial crane can be seen in Figura 6.1. The bearing structure consists in five square steel tubes with a side of 150 $[mm]$, a length of 2.5 $[m]$ and a width of 5 $[mm]$. Connecting the top of the structure a sliding guide is present, which sustain the sliding cart. Mounted on the sliding cart there is the second motor, responsible for the lifting of the payload, consisting in a cylindrical concrete block, with a diameter of 80 $[mm]$ and a length of 872 $[mm]$. The weight of the guide is 45 $[kg]$, the one of the sliding cart is 5 $[kg]$, the motor and the mechanical structure needed for it to be fixed to the cart together weight approximately $m_C = 38$ $[kg]$, while the two

Figure 6.1: Picture of the system used to test the control techniques.

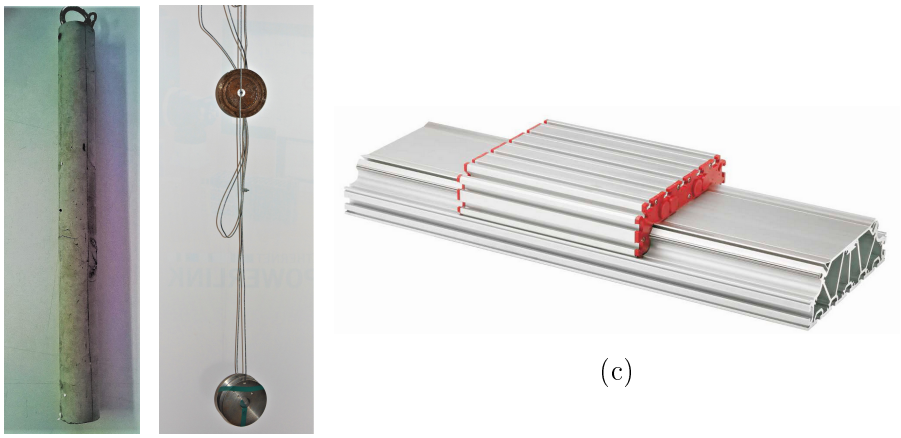

(a) (b) (c)

Figure 6.2: 6.2a Distributed payload, consisting in a concrete cylinder. 6.2b Distributed payload, consisting in two different iron discs. 6.2c hook plus pointmass payload.

payloads used weight between 9.8 and 8.35 $[kg]$.

The discussed techniques have been tested on two different configurations.

On the first configuration, a distributed payload consisting of a chylindrical concrete block has been used. While the length of the cable that connects cart and payload can vary by actuating the motor, the length of l_2 of the double pendulum model of the system and the masses m_1 and m_2 can be found using the equivalent system for distributed payloads presented in Chapter 2.2.3 applied to the distributed payload reported in Figure 6.2a. In particular, using (2.62) with the measured mass and length of the payload, the results are:

$$\begin{cases} m_1 = 2.45 \ \ [kg] \\ m_2 = 7.35 \ \ [kg] \\ l_2 = 0.581 \ \ [m] \end{cases} \tag{6.1}$$

For the purpose of testing the techniques, length l_1 has been fixed to a value $l_1 = 1.120$ $[m]$ for the case of distributed payload.

The second configuration consists in an hook of not negligible mass, which is represented by a disc of mass $m_1 = 4.57$ $[kg]$, and a payload consisting in a disc with mass $m_2 = 3.78$ $[kg]$, as shown in Figure 6.2b. Both hook and

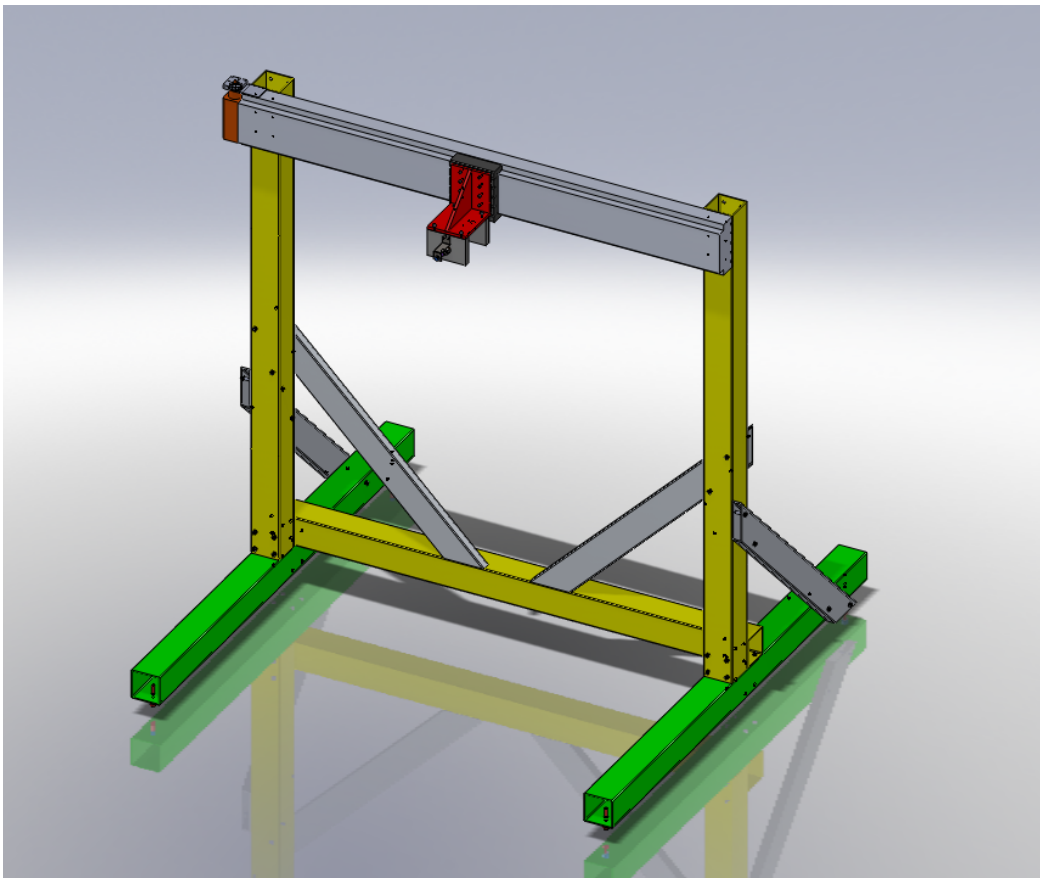

Figure 6.3: Mechanical structure of the system.

payload can in this case be modelized as a masspoints.

The square consisting in the yellow tubes in Figure 6.3 and the guide are sustained by the green tubes, which sustain the whole weight of the structure. In order to ensure stability and stiffness to the structure four other rectangular steel tubes has been added to counteract the bending moments. Thanks to the oversized dimensions of the tubes and the hyperstaticity of the system the structure can be considered as rigid. As proof of this approximation, a numerical example has been reported in [26] with very conservative conditions.

The top of the structure is composed by a recirculating ball bearing guide, with a length of 2.5 $[m]$. The cart is actuated by a motor through a gearbox and a power transmission belt. The linear friction coefficient of the cart,

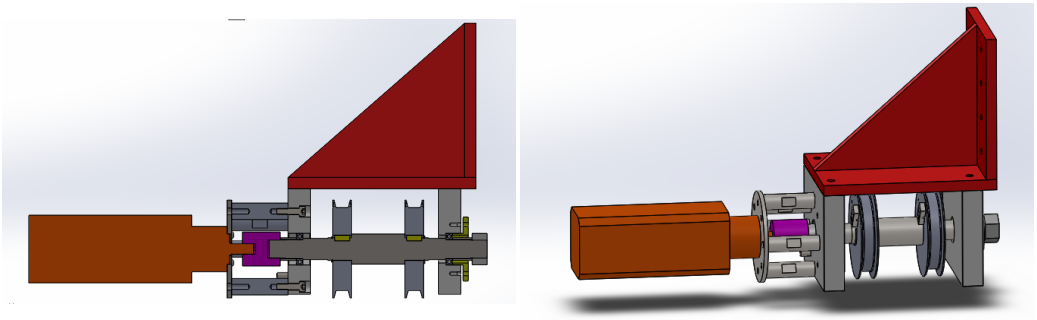

Figure 6.4: Scheme of the lifting system.

calculated in [26], is $C_C = 85\ [Ns/m]$.

One of the possible future works on this system is the study of control techniques on time-variant systems, and for this reason a second motor has been added to vary the length of the cable through the lifting of the payload.

A study of forces and inertia has been made, and the supporting system has been changed from the setup used in [26], adding a second motor and two pulleys. A scheme of the new part is shown in Figure 6.4. For a deeper review of the lifting system, see [7].

The two motors, the one that actuates the sliding of the cart and the one which lifts the payload, are both brushless motors. The model of the two motors is the same, that is *B&R 8LSA34.ee030ffgg-0*, like the one shown in Figure 6.5a. Being brushless motors they can satisfy requirements of high precision positioning with fast dynamics, such is the case of the system built. The main specifications of the motor are listed in Table 6.1. The motors are equipped with Endat absolute multi-turn encoders. The main advantage of EnDat encoders is that there is no need for an initial homing procedure of the system when it is turned on. The absolute position of the motor is saved when the system is turned off, and when it is turned on the actual position is known even if the motor has been moved for more than one turn (up to 4096 turns). Both the motors are equipped with a planetary gearboxes, with a gear ratio of 1:10, like the one shown in Figure 6.5b. The main specifications of the gearboxes are reported in Table 6.2.

The last parameters needed in order to apply the techniques seen to the crane are the natural frequencies and the dampings. It is possible to calculate

Nominal velocity	3000 $[rpm]$
Nominal torque	1.4 $[Nm]$
Nominal power	440 $[W]$
Nominal current	0.96 $[A]$
Nominal stall torque	1.5 $[Nm]$
Stall current	1.03 $[A]$
Maximum Torque	6 $[Nm]$
Maximum current	4.43 $[A]$
Maximum angular acceleration	100000 $[rad/s^2]$
Maximum velocity	12000 $[rpm]$
Torque constant (Kt)	1.46 $[Nm/A]$
Stator resistance	32.3 $[\Omega]$
Stator inductance	73.12 $[mH]$
Electrical time constant	2.26 $[ms]$
Thermal time constant	35 $[min]$
Moment of inertia	0.6 $[kgcm^2]$
Weight	2.89 $[kg]$

Table 6.1: Motor nominal specifications.

Gear ratio	1 : 10
Nominal output torque	15 $[Nm]$
Maximum output torque	24 $[Nm]$
Moment of inertia	0.06 $[kgcm^2]$
Weight	0.9 $[kg]$

Table 6.2: Main parameters of the gearbox.

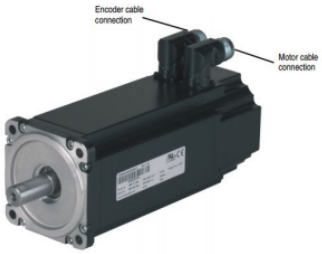

(a) *B&R 8LSA34.ee030ffgg-0* motor.

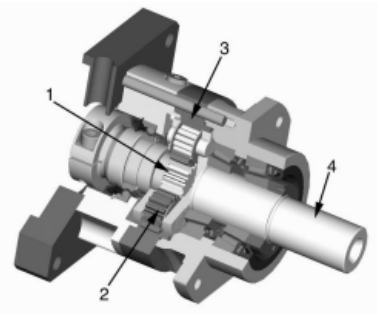

(b) Particular of the planetary gearbox.

Figure 6.5: Motors and gearboxes used for the motion of the cart and the lifting of the payload

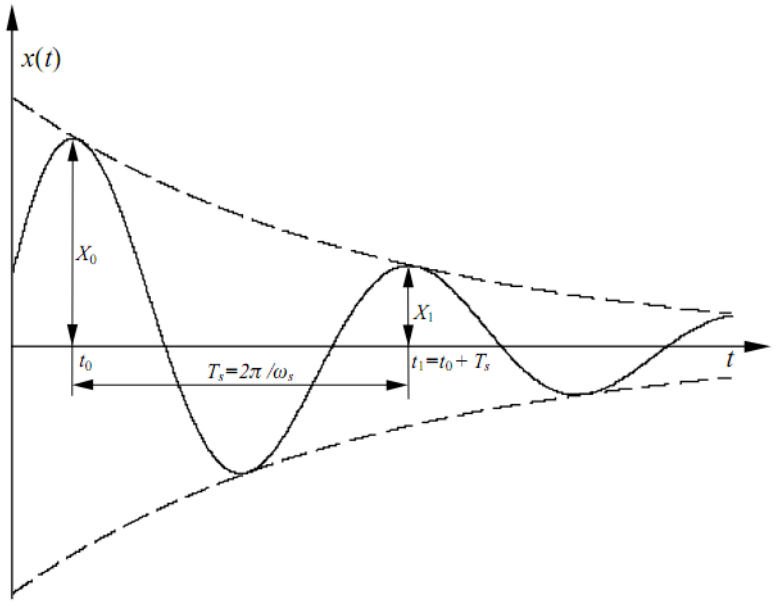

Figure 6.6: Logarithmic decrement of a second order system.

the dampenings through experimental measures using the logarithmic decrement. Referring to Figure 6.6, the logarithmic decrement δ can be calculated as

$$\delta = ln\left(\frac{X_0}{X_1}\right) \tag{6.2}$$

and, for the general case of non-consecutive peaks,

$$\delta = \frac{1}{k} ln\left(\frac{X_0}{X_k}\right) \tag{6.3}$$

Given

$$\delta = \xi \omega_n T_s \tag{6.4}$$

, where T_s is the dumped period defined as

$$T_s = \frac{2\pi}{\omega_s} = \frac{2\pi}{\omega_n \sqrt{1-\xi^2}} \tag{6.5}$$

then

$$\delta = \frac{2\pi\xi}{\sqrt{1-\xi^2}} \tag{6.6}$$

and finally, by inverting (6.6), we have

$$\xi = \frac{\delta}{\sqrt{(2\pi)^2 + \delta^2}} \tag{6.7}$$

In order to obtain the values $\xi_{1,2}$ for the model, the first and second natural frequencies of the payload have been excited manually, and the angle θ_1 measured, giving the results shown in Figure 6.7 for the configuration of distributed payload.

From (6.3), (6.7) and the data in Figure 6.7, the following damping ratios have been calculated:

$$\begin{aligned} \xi_1 &= 0.003 \\ \xi_2 &= 0.038 \end{aligned} \tag{6.8}$$

The undamped frequencies can be found by using (2.80) with the parameters found or by checking the damped period T_s in Figure 6.7 and by inverting T_s. From the model, we find

$$\begin{aligned} \omega_1 &= 2.48 \quad [rad/s] \\ \omega_2 &= 9.81 \quad [rad/s] \end{aligned} \tag{6.9}$$

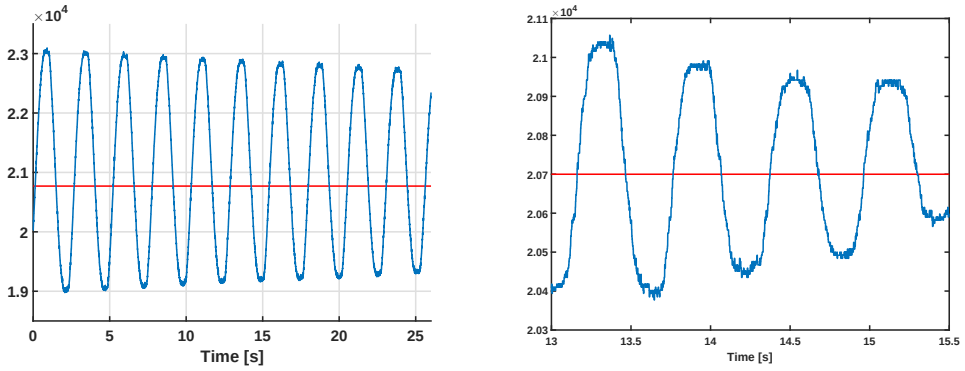

(a) (b)

Figure 6.7: Trajectory of θ_1 after excitations of 6.7a the first natural frequency and 6.7b the second natural frequency. The ordinate represents the value returned by the ADC, an unsigned integer.

The values of the coefficients C_1 and C_1 that returns the values of (6.8) given (6.9) by solving (2.84) can be approximated as

$$\begin{aligned} C_1 &= 0.1 \quad [Nms/rad] \\ C_2 &= 0.4 \quad [Nms/rad] \end{aligned} \tag{6.10}$$

Following the same process, the parameters for the configuration of hook and payload are

$$\begin{aligned} \xi_1 &= 0.004 \\ \xi_2 &= 0.05 \\ \omega_1 &= 2.47 \quad [rad/s] \\ \omega_2 &= 5.54 \quad [rad/s] \\ C_1 &= 0.15 \quad [Nms/rad] \\ C_2 &= 0.7 \quad [Nms/rad] \end{aligned} \tag{6.11}$$

Summarizing, the parameters that fully describe the model of the crane are reported in Table 6.3 for the configuration with distributed payload, and in table 6.4 for the configuration with hook and masspoint payload.

In Figure 6.8 the zeros and poles are plotted in a logarithmic scale for both distributed and hook and mass payloads used. It can be seen how the

m_C	38.0 $[kg]$
m_1	2.45 $[kg]$
m_2	7.35 $[kg]$
l_1	1.12 $[m]$
l_2	0.581 $[m]$
C_C	85 $[Ns/m]$
C_1	0.1 $[Nms/rad]$
C_2	0.4 $[Nms/rad]$
ω_1	2.48 $[rad/s]$
ω_2	9.81 $[rad/s]$
ξ_1	0.003
ξ_2	0.038

Table 6.3: Parameters of the crane model with distributed payload.

m_C	38.0 $[kg]$
m_1	4.57 $[kg]$
m_2	3.78 $[kg]$
l_1	1.03 $[m]$
l_2	0.86 $[m]$
C_C	85 $[Ns/m]$
C_1	0.15 $[Nms/rad]$
C_2	0.7 $[Nms/rad]$
ω_1	2.47 $[rad/s]$
ω_2	5.54 $[rad/s]$
ξ_1	0.004
ξ_2	0.05

Table 6.4: Parameters of the crane model with hook and mass payload.

zeros are far faster than the poles and can therefore be neglected for control purposes.

6.2 Electrical components

In this section the electrical components of the system will be presented. As shown in Figure 6.9, four *B&R* off-the-shelf industrial products have been used in order to control the motors and to acquire signals. A PLC, marked with the number 1 in Figure 6.9, computes the main code and communicates with the other modules. In particular, it communicates through an HUB with a PC platform (used for programming, debugging and data acquisition) and with a Power Panel, from which the operator can set parameters and send commands to the system. Even if the trajectories to be followed are built by the CPU, an ACOPOS servo driver, marked with number 4 in Figure 6.9, receives the setpoint sent by the PLC and control the movements of the motors. Servo drive and PLC communicate through ETHERNET POWERLINK, a deterministic open protocol introduced by Austrian automation company *B&R* in 2001.

6.2.1 PLC

The PLC used mounts a INTEL-compatible Celeron 650 CPU, with a cycle time up to 200 $[\mu s]$ and runs a multitasking real time OS named Automation Runtime (see Chapter 6.3.2). In Figure 6.10 a of the PLC is presented. The ROM memory of the PLC consists of a removable compact flash memory. The PLC has two Ethernet ports that support POWERLINK and Ethernet communication, two USB ports and a RS232 interface module. Moreover X2X native communication is supported. The PLC is powered with 24 $[V]$ by an external module, marked in Figure 6.9 with the number 2, which is powered by a general 220 $[V]$ alternate current power supply. Some I/O modules have been added to the standard PLC configuration, in order to be able to acquire data from external sensors (e.g. sensors like potentiometers or mechanical limit switch). In particular, a module for 12 digital inputs is present, along with a 12 digital outputs module, a 2 analog inputs and a 2

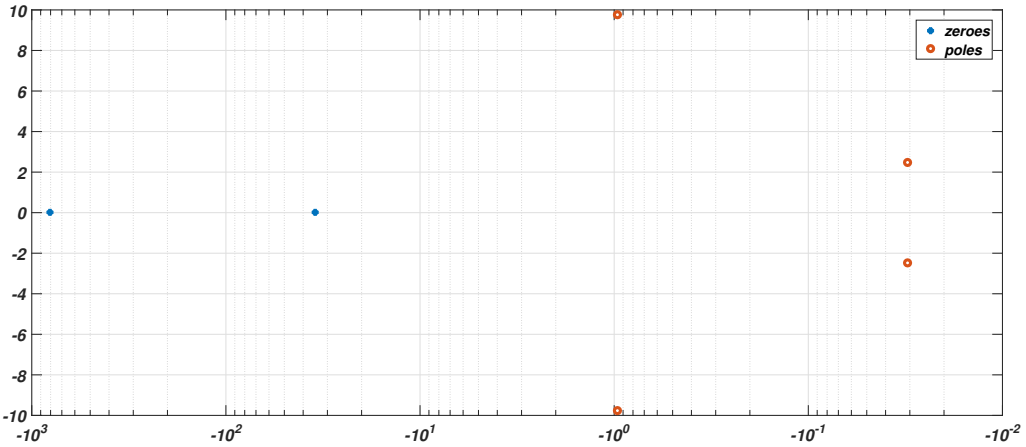

(a) Zeros and poles with the distributed payload.

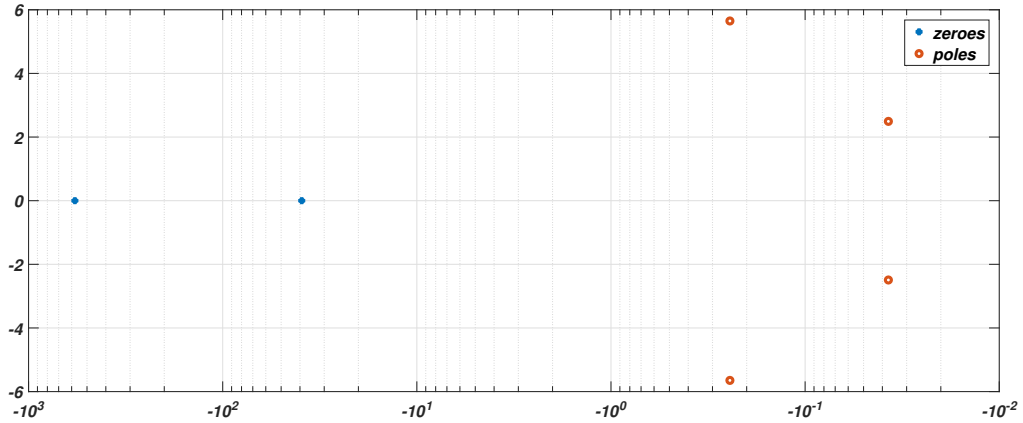

(b) Zeros and poles with the hook and mass payload.

Figure 6.8: Poles and zeros of the system with the payloads used. The zeros can be neglected for control purposes, due to their fast dynamics.

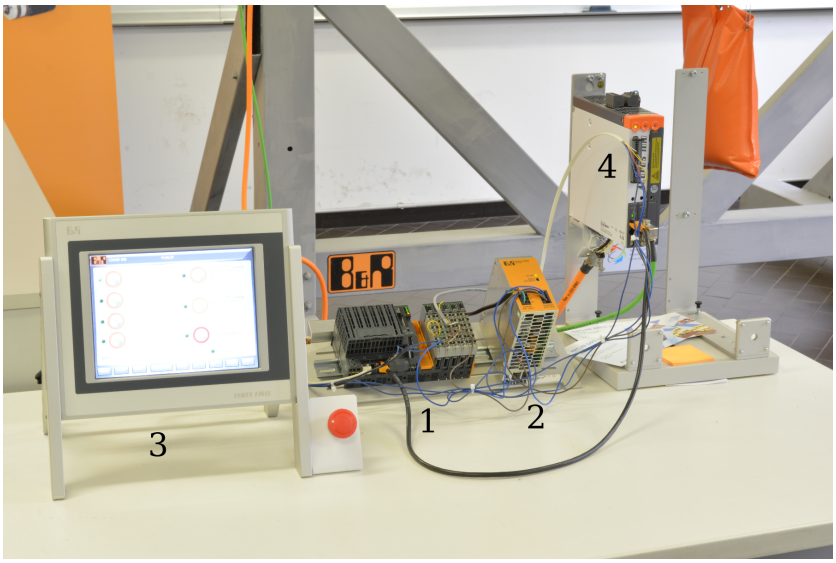

Figure 6.9: *B&R Electrical components used.*

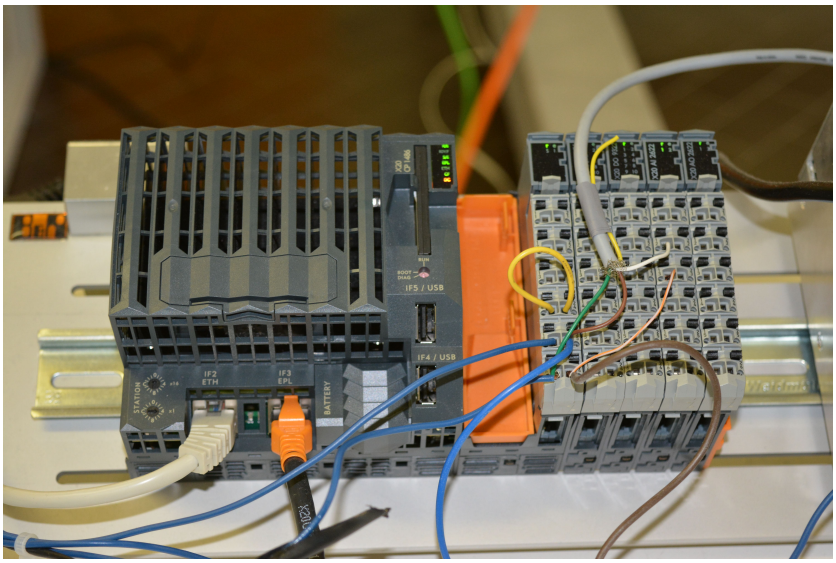

Figure 6.10: *B&R X20CP1486*

Figure 6.11: *B&R Power Panel 4PP320_1043_31*

analog output modules.

6.2.2 Power Panel

In order to create an interface from the operator to the system a B&R Power Panel has been used. The panel used is a 10.4" resistive touch screen, like the one shown in Figure 6.11, connected to the PLC using Ethernet protocol by means of an HUB. The screen is programmed with the visualization section of the Automation Studio *B&R* proprietary software. The power panel has its own compact flash in which are stored the informations needed to handle the interface, and it is powered with 24 $[V]$ by the the same external module that powers the PLC.

6.3 Control scheme and components

In this section the control part of the system will be presented. First, the servo driver used will be shown, presenting the B&R proprietary control scheme implemented inside the driver. Then, an overview of the operating systems and IDE used will be shown. Finally, the main program that imple-

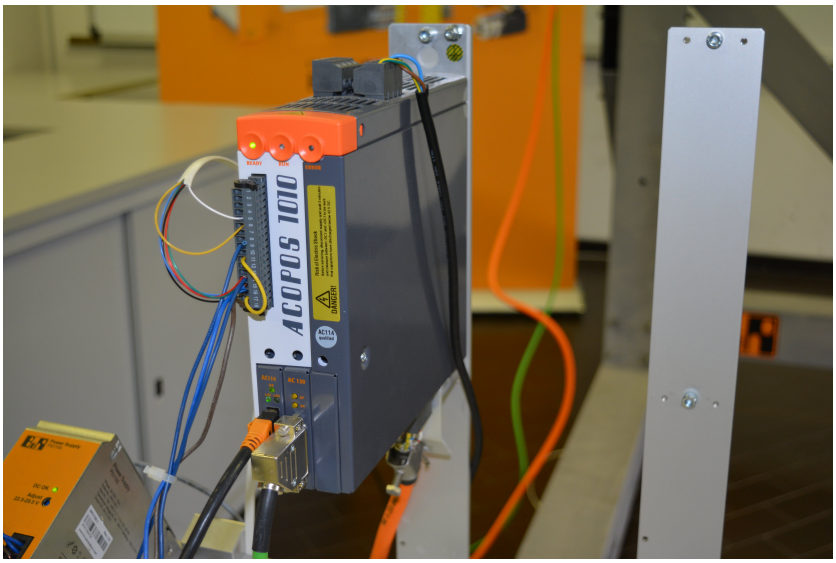

Figure 6.12: *B&R ACOPOS 8V1010.50-2*

ments the motion of the cart following the techniques seen in the previous chapters will be discussed.

6.3.1 Servo driver

The servo driver used to control the motion of the motors is an *ACOPOS 8V1010.50-2*, like the one shown in Figure 6.12. It is provided with a POWERLINK interface, used to communicate with the PLC, and a AC120 plug-in module to communicate with the EnDat encoder of the motor. The driver runs a NC operating system; it directly communicates to a part of the program implemented on the PLC, the NC Manager, which provides the driver with some parameters, called ParID, in order for example to tune internal control loops.

The internal control scheme operated by the servo driver is shown in Figure 6.13. It is a cascade control scheme, with an internal current loop, an intermediate velocity loop and an external position loop. The parameters of the controllers of the two outer control loops (that have a PID structure) can be set by the user modifying particular ParIds. The inner one, the current loop, is closed to external tuning.

Figure 6.14 shows the internal control schemes of the position and velocity

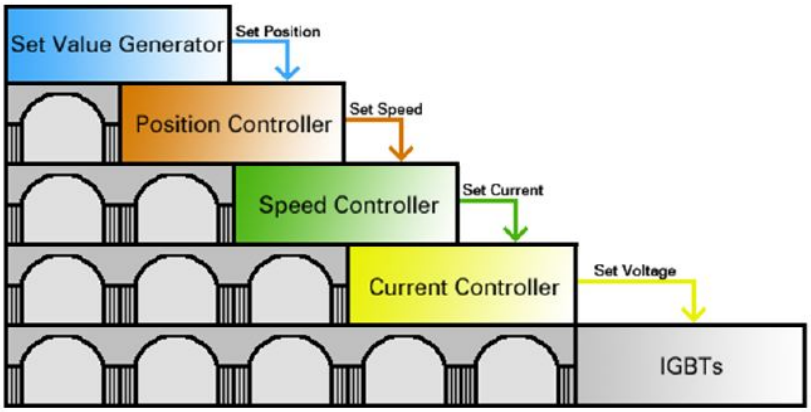

Figure 6.13: Internal control scheme of the ACOPOS servo driver [1].

control loops, and focuses on the scheme that shows how it is possible to insert a torque feedforward signal to the driver.

The outer position control runs with a cycle time of 400 [μs] and use a PI controller equipped with an anti-windup part to avoid integral overcharges. The output of position controller (v_set) is the sum of the signal calculated after the PI controller and the anti-windup and a value called "v_feed" resulting from a prediction block.

The velocity loop works at 200 [μs] and follows the same pattern of the position one. A PI control with anti-windup is used. The feedback signal is a velocity, usually noisy, and it is thereby filtered by a low-pass filter. It is also possible to provide a feedforward torque signal.

The inner one is a torque control loop, with the possibility to compensate Coulomb and viscous friction and with a block that specify the entity of the motor's load. The torque is then converted to current by means of a block that uses the characteristic curve of the motor used on the project.

6.3.2 Automation Runtime

Automation Runtime is the proprietary real time operating systems ran by B&R components. It can run on every CPU-based hardware produced: PLC, industrial PCs and Power Panels. This OS allows the CPU to run tasks with different priorities in a deterministic way. Every task has its priority and its

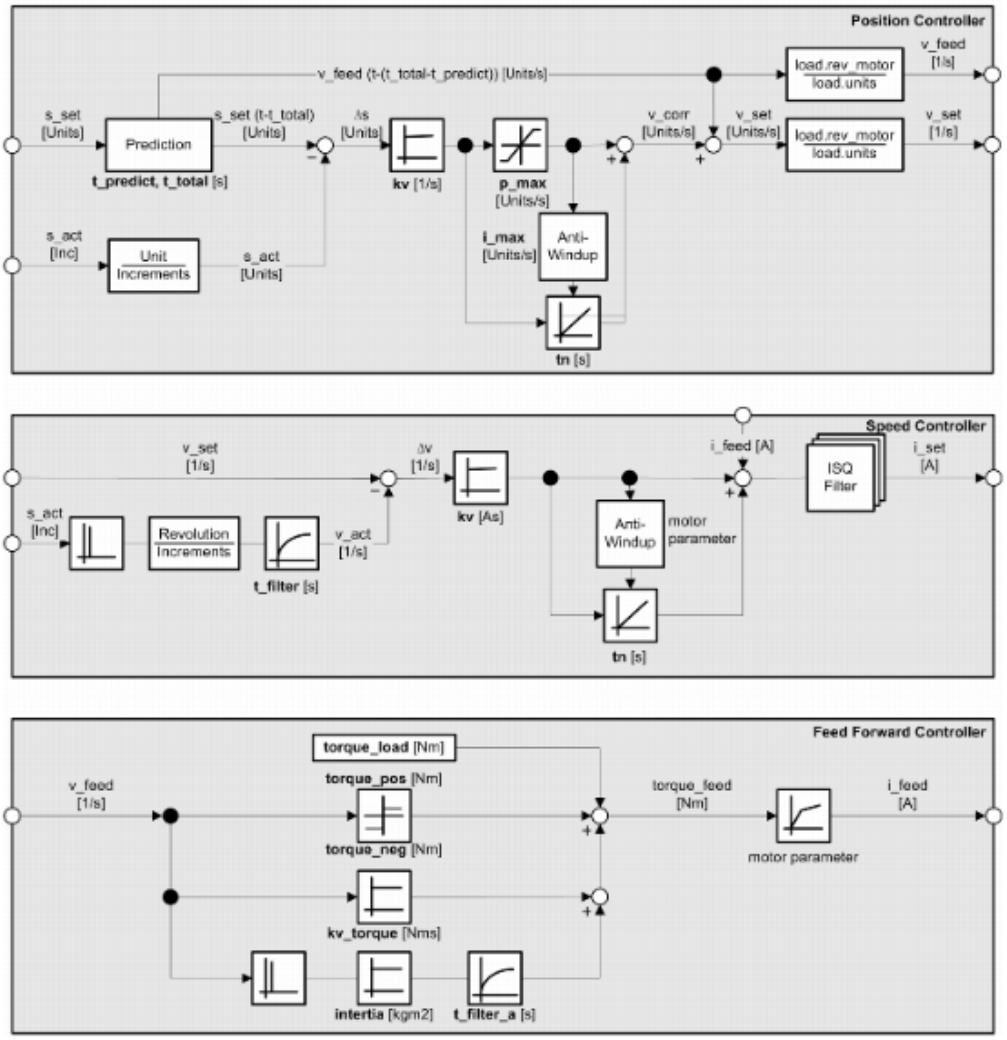

Figure 6.14: Scheme of position, velocity and torque control loops.

cycle time of execution, but it can also allow some "tolerance" in the respect of this cycle time, depending if the task is more or less critic. The main feature of Automation Runtime are the following ones:

- Guaranteed highest possible performance for the hardware being used
- Runs on all B&R target systems
- Makes the application hardware-independent
- Applications can be easily ported between B&R target systems
- Cyclic system guarantees deterministic behaviour
- Configurable jitter tolerance in all task classes
- Supports all relevant programming language such as IEC 61131-3 and C
- Extensive function library conforming to IEC 61131-3 as well as the expanded B&R Automation library

6.3.3 Automation Studio

Automation Studio is a proprietary software for programming all the components provided by B&R. Automation Studio is an IDE that support all the programming languages of IEC 61131-3 standard:

- Instruction List (IL)
- Structured Text (ST)
- Ladder Diagram (LD)
- Function Block Diagram (FBD)
- Sequential Function Chart (SFC)

Moreover, Automation Studio supports three other languages:

- ANSI C

- B&R Automation Basic
- Continuous Function Chart (CFC)

Automation Studio allows to develop the software part of the project independently from the hardware components; it also support simulations, so that the project can be tested before being transferred to the hardware. A tool that would have facilitate the implementation of the technique that is available in Automation Studio is the "B&R Automation Studio Target for Simulink" that allows the auto-coding and the transfer of Simulink schemes inside the project. This strongly facilitate and accelerate the process of programming model-based applications and rapid prototyping, particularly when the model's scheme are already available on Simulink. For the purposes of this thesis the schemes and blocks used in Chapter 5 could have been used. By the way, the function blocks that implement the techniques seen have been programmed by scratch to show the applicability in industrial environments, even without having access to Mathworks or B&R particular licenses for auto-coders

For more informations about Automation Runtime and Automation Studio see [1].

6.3.4 The main program

In this section the structure of the main control implemented in Automation Studio's environment will be discussed. The main program structure is based on a standard B&R Finite State Machine for industrial machines, modified in order to meet the needs of the application. Once again, this also shows how the techniques can be easily applied to industrial application.

The core of the program is the code inside the task named as *MovePosNeg*, which manages the coordination of the cart's movements. Other tasks are present, e.g. for the management of the external sensors or the visualization.

All the techniques studied have been developed in Function Blocks (written in ANSI C or Structured Text) and included in exportable libraries, so that they can be easily exported to other projects. The implementation of those Function Blocks will be discussed in greater detail in Chapter 7.

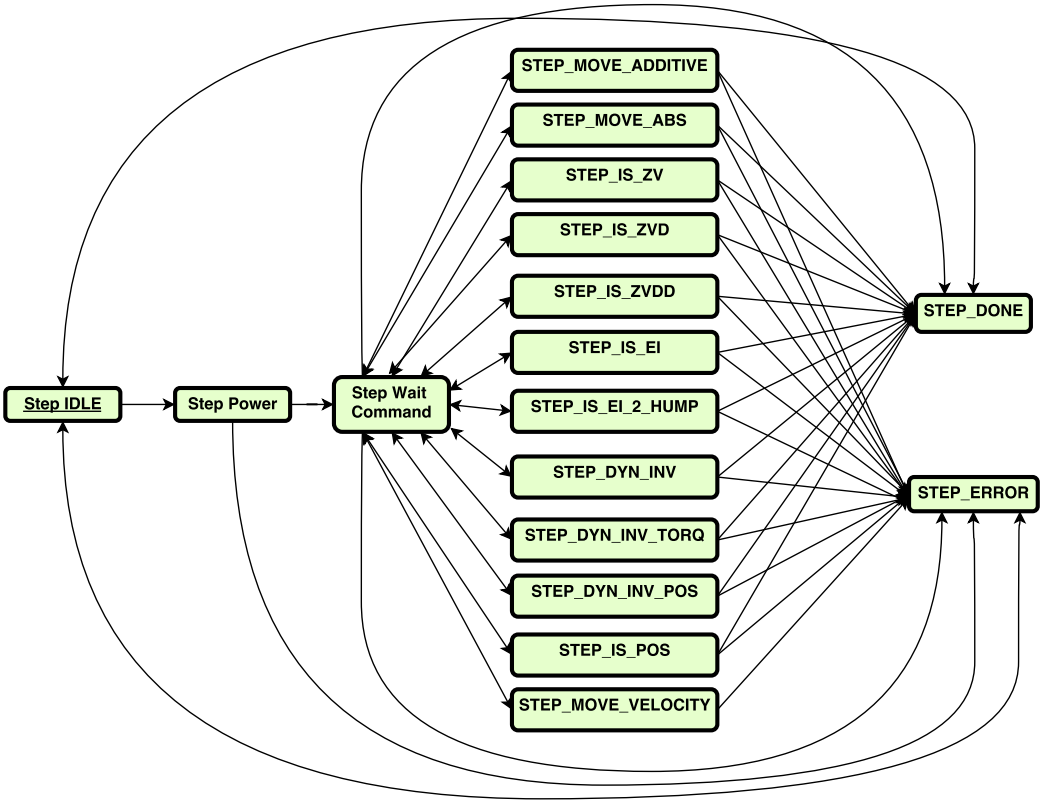

Figure 6.15: Simplified scheme of the Finite State Machine used.

The main program is written in ANSI C and the Finite State Machine is implemented with a switch statement where every case consists in a single state of the FSM graphically represented in Figure 6.15. Actually, what is reported in Figure 6.15 is just a simplification of the complex of different states implemented, as will be discussed in Chapter 7, but is a more schematic representation of the program's real flow.

Below a brief description of every operative state of the machine is given. In `Step IDLE` the PLC waits the command to switch on the power to the servo driver and start the motion. It is a safe state, where the cart does not have applied torque. When the PLC is turned on it automatically goes in `Step IDLE`, and it returns to `Step IDLE` from `STEP_ERROR` after the reset or when the operator decide to stop the actual movement through `STEP_DONE`. When the CPU in `Step IDLE` receives the activation command from the Power Panel it activates the loops of the servo driver and the motors are

activated. Subsequently, the machine goes to `STEP_WAIT_COMMAND`, where it wait for operative commands. From `STEP_WAIT_COMMAND` the machine can go to any of the possible operative states described below.

There are two different ways of moving the cart in position without using the control techniques described. Both relative and absolute position can be given to the machine. In case of relative movements, the machine goes in `STEP_MOVE_ADDITIVE` and the cart accelerate and decelerate with the setted values till the setted value of velocity for the total displacement given by the operator. In case of absolute movements, the machine goes in `STEP_MOVE_ABS` and the cart goes to the absolute position given by the operator with setted accelerations and velocity. The cart can also be moved in velocity: the cart moves with setted velocity until the dedicated command button is released. This task is carried out by `STEP_MOVE_VELOCITY`.

Regarding intelligent velocity control, all Input Shaping techniques seen in Chapter 3 have been implemented. Depending on the command sent by the operator, the control of the cart can be done with Zero Vibration IS (`STEP_IS_ZV`), Zero Vibration and Derivative (`STEP_IS_ZVD`), ZVDD Input Shaping (`STEP_IS_ZVDD`) and with Extra-Insensitive techniques with three or four impulses (`STEP_IS_EI` and `STEP_IS_EI_2_HUMP`). Inverse dynamics velocity control is carried out by `STEP_DYN_INV` and by `STEP_DYN_INV_TORQ` depending on the presence or not of torque feedforward.

As for intelligent position control, a desired displacement and transient time can be set, and the motion can be done both with inverse dynamics techniques (`STEP_DYN_INV_POS`) that directly invert the position and uses torque feedforward and with Input Shaping techniques (`STEP_IS_POS`), for which a trajectory has to been shaped. More details on the implementation of this technique are presented in Chapter 7.1.2.

If, for any reason, the operator decides that the movement has to be terminated and that the motor has to be deactivated, the machine can go from any operative state to `STEP_DONE`, from where it reach again `STEP_IDLE`.

In case of internal errors (e.g wrong setted parameters), when the set velocity/acceleration exceeds the setted values or when the operator press the red emergency button, the machine goes to `STEP_ERROR`. In order to

return to operative states the errors have to be expressively acknowledged by the operator.

6.4 Product code of used components

As already done in [26], here the product codes for the industrial components used for the experimental set-up. This will facilitate future modifications of the set-up itself.

- Brushless motors: 8LSA34.ee030ffgg-0, B&R;
- Planetary gearbox: 8GP40-060hh010klmm, B&R;
- PLC: X20CP1486, B&R;
- Digital inputs module: X20DI9371, B&R;
- Digital outputs module: X20DO9322, B&R;
- Analogical inputs module: X20AI2622, B&R;
- Analogical outputs module: X20AO2622, B&R;
- Power Panel: 4PP320.1043-31, B&R;
- Servo drivers: Acopos1010.50-2, B&R;
- Power supply: Power Supply 1100, B&R;

Chapter 7

Controller implementation

After having developed the theory in Chapter 3 and Chapter 4 and having simulated the techniques in Chapter 5, here the control techniques for the elimination of residual oscillations will be implemented on industrial off-the-shelf components and applied on a real system, described in Chapter 6.

First the implementation of input shaping techniques will be shown for both the cases of velocity and position control, along with the generation of the trajectory to be shaped.

Then the implementation of Input-Output inversion will be presented, showing how the results found in Chapter 4 have been applied to the control of the crane. Both velocity and position control will be presented, along with the force feedforward signal calculus.

In Figure 7.1 the main HMI control page is shown, divided in all the parts that use different control techniques.

7.1 input shaping

There are two possible ways to control the movement of an industrial overhead crane. The most common one is the velocity control. With velocity control, the operator pushes a button and the crane accelerates and starts moving with a setted velocity in the desired direction. When the operator releases the button, the crane decelerates and stops its motion. The second way an industrial crane can be controlled is in position. When the command

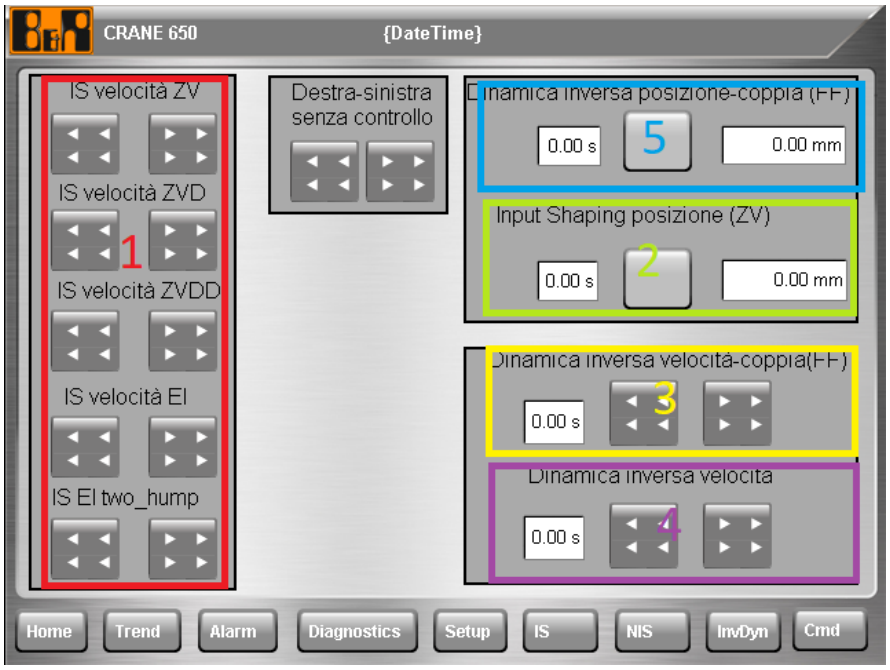

Figure 7.1: Main control page.

is given, the crane follows a given trajectory and reach the setted position. Both velocity and position control are matter of interest in industrial research, as the first one is used when a human operator is directly controlling the payload, while the second one is used for example in fully automated warehouses.

As already explained, it is utterly important to avoid residual oscillations, both in case of velocity and position control. input shaping techniques for residual oscillations minimization can be applied in any case. In fact, the system natural frequencies and dampenings do not change depending on the way the system is controlled.

7.1.1 Velocity control

In the case of velocity control, an acceleration profile has to be given to the system in order to define the law of motion to be followed during the transient between the moment the button is pressed and the moment the cart reach the desired constant velocity. A constant acceleration law of motion has been

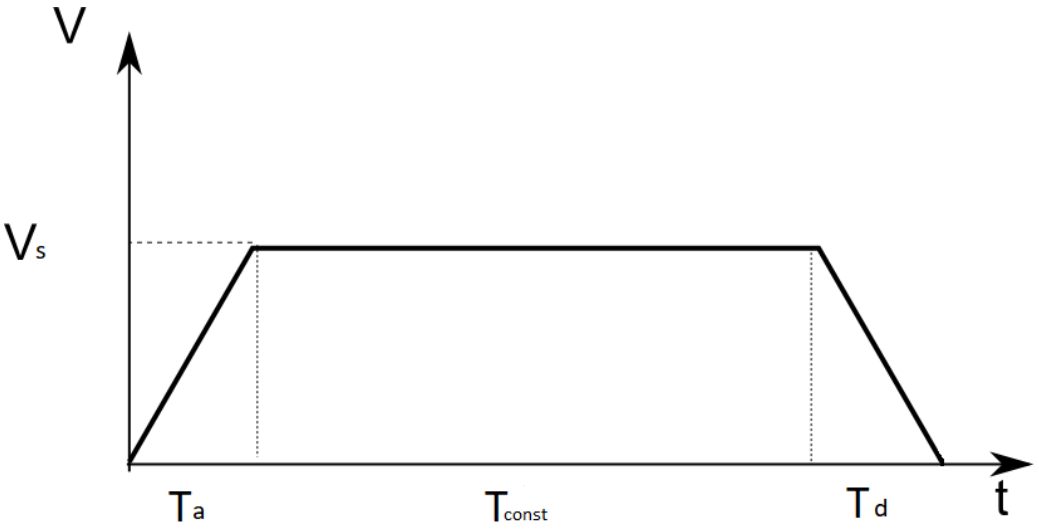

Figure 7.2: Shape of velocity control used. t_a and t_d are the acceleration and deceleration time.

chosen to characterize this transient, for it is the easiest way to define the acceleration between null and constant velocity, and also because is the law of motion that takes full advantage of the acceleration limits of the motor.

The velocity control profile can thereby be defined as

$$v(t) = \begin{cases} 0, & \text{if } t \leq 0 \\ at, & \text{if } 0 < t < \frac{V_s}{a} \\ V_s, & \text{if } t \geq \frac{V_s}{a} \end{cases} \tag{7.1}$$

where V_s is the operating speed and a the acceleration, and the command button is pressed at $t = 0$. When the button is released, the cart decelerates until it stops. The profile described by (7.1), with the addition of the deceleration part just described, is shown in Figure 7.2.

Equation (7.1) has been expressed in ST code in Automation Studio as a function, requiring as parameters acceleration a, final velocity V_s and time t and returning the value $v(t)$.

For the implementation of the five input shaping techniques seen five different Function Blocks have been built. Since IS techniques require the scaling and delaying of the input signal, an internal circular buffer in the form of a vector of floats has been initialized inside every Function Block used.

Care must be taken in the dimension of the vector. In fact, every element of the vector memorize a sample of the signal. Given the sampling time (in our case corresponding to the cycle time of the main task), the dimension of the buffer has to be enough to memorize at least a number of samples corresponding to half of the period of the system for *ZV*, a whole period for *ZVD* and *EI* techniques and a period and a half for *ZVDD* and *EI two hump*.

Every Function Block requires as input parameters a natural frequency, correspondent damping coefficient and the sample of the input signal to be shaped. Inside the Function Block the parameter K is calculated using (3.12) and then used to calculate the amplitudes of the impulses to be convolved with the input signal. For *ZV* the amplitudes are given by (3.13), for *ZVD* by (3.15) and for *ZVDD* by (3.16). For *EI* and *EI two hump* the coefficients are calculated as reported in [33], choosing a maximum residual oscillation of $V_{tol} = 5\%$.

The input signal sample is stored inside the circular buffer and the counter is updated. The output of the function is updated multiplying the current sample for A_1, the sample corresponding to t_2 taken from the circular buffer for A_2 and so on. If the system has two or more natural frequencies, two IS Function blocks can be connected in series, with the same structure used in simulation (see Figure 5.4).

When a command button inside the section marked with 1 in Figure 7.1 is pushed, the state machine goes from the state `STEP_WAIT_COMMAND` to the state in Figure 6.15 that manages the corresponding techniques. Actually, four different states for every techniques have been created. Two states coordinates the movement in one direction, one for the acceleration and the constant velocity movement and one for the deceleration, and other two coordinates the movement in the other direction. For example, when the button for velocity control in left direction with *ZV* filter is pushed, the machine goes to state `STEP_LEFT_IS_ZV`, which, keeping track of the time, calls the ramp function in order to generate a setpoint corresponding to (7.1). The two *ZV* function blocks are then called, giving the current value of the ramp as input of the first block, and the output of the first block as input to the second block. The output of the second block is then set as reference to ACOPOS servo driver.

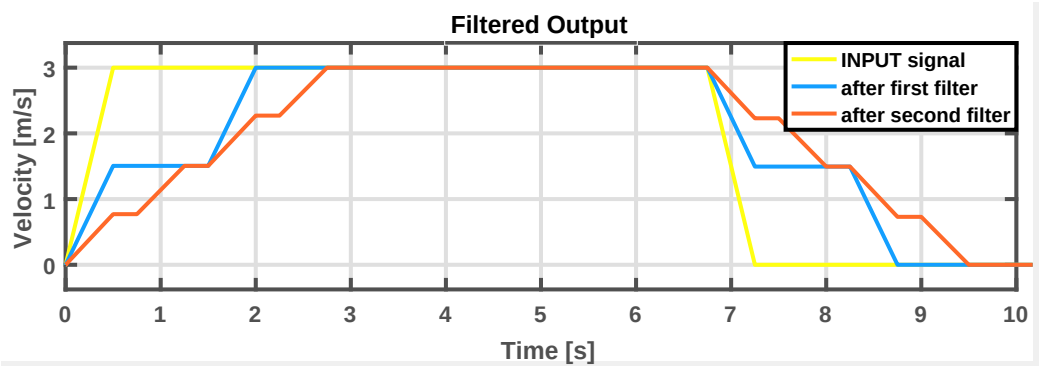

Figure 7.3: Example of velocity control.

When the button is released, the machine goes to a state that coordinates the deceleration. In the case of ZV, the machine goes to state `STEP_DEC_LEFT_IS_ZV`. The setpoint of the velocity loop is a negative ramp, going from V_s to zero with the desired deceleration, filtered through two ZV Function Blocks.

Every time the machine enters a state in which input shaping Function Blocks are used, the circular buffer of the corresponding Function Blocks must be re-initialized to zero.

In Figure 7.3 an example of velocity control is shown. For this example, the system periods have been set to $T_1 = 3s$ and $T_2 = 1.5s$ At time $t = 0s$ the user pushes the button, and the ramp function generates the velocity profile corresponding to the yellow line. At time $t = 6.75s$ the button is released and the velocity returns to zero following the same ramp profile. The yellow line is first filtered with ZV technique with a period of T_1, generating the blue profile. This blue profile is the input of the second filter, which filter with period T_2, and the output, corresponding to the orange line, is the velocity reference for the physical system.

7.1.2 Position control

As already said, input shaping techniques can be used also in the case of position control.

First, a reference trajectory must be defined. Even if many choices are possible, a trapezoidal motion results convenient, as it is characterized by

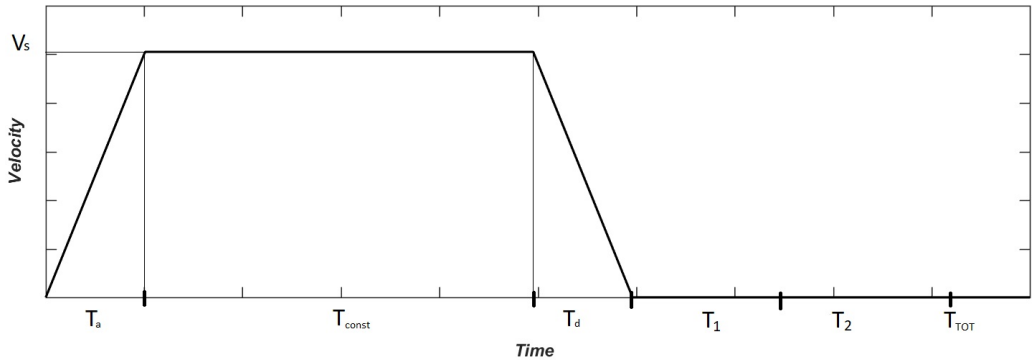

Figure 7.4: Trapezoidal velocity profile used in position control. T_1 and T_2 are the delays due to the shapers.

the same shape in velocity as the on used in the previous chapter (see Figure 7.2). In fact, the total displacement corresponds to the integral of the curve.

For the position the setpoint is absolute, and set on the Power Panel, where the total movement time is also defined. When the button in the section marked with 2 in Figure 7.1 is pushed,the actual position of the cart is read, a relative position setpoint is calculated and the machine goes to state `STEP_CYCLIC_POSITION_IS`. Here a Function Block is used to calculate the setpoint for every instant of time.

Lets take a look to Figure 7.4. In order to complete the movement of the cart in the desired time, the input trajectory has to take into account the delay introduced by the shapers. In particular the input trajectory has to end at time $T_{tot} - T_1 - T_2$, where T_{tot} is the total time of the movement setted, and T_1 and T_2 the delays introduced by the shapers. T_1 and T_2 depends on the technique used. As already seen, for ZV the delay correspond to half the damped period, for ZVD and EI to a whole damped period and for $ZVDD$ and *EI two hump* to a period and a half.

Given the accelerations (assume for simplicity that acceleration and deceleration have the same value a), the acceleration time is given by

$$T_a = T_d = \frac{V_s}{a} \tag{7.2}$$

where V_s is now unknown. The velocity can be found by equalizing the integral of the trapezoid in Figure 7.4 to the displacement x corresponding

to the difference between final and initial position, that is by solving

$$\frac{V_s(T_a + T_d)}{2} + V_s(T_{tot} - T_1 - T_2 - T_a - T_d) = x \tag{7.3}$$

and, by replacing (7.2) in (7.3),

$$-\frac{1}{a}V_s^2 + V_s(T_{tot} - T_1 - T_2) - x = 0 \tag{7.4}$$

Solving (7.4) leads to

$$V_{s_{1,2}} = \frac{a}{2}(T_{tot} - T_1 - T_2) \pm \sqrt{(T_{tot} - T_1 - T_2)^2 - 4\frac{x}{a}} \tag{7.5}$$

which makes sense only with the minus. In fact, with the plus a null displacement would lead to a positive velocity.

Now that V_s is known, the velocity pattern in Figure 7.4 can be described as

$$v(t) = \begin{cases} 0, & \text{if } t \leq 0 \\ at, & \text{if } 0 < t \leq \frac{V_s}{a} \\ V_s, & \text{if } \frac{V_s}{a} < t \leq (T_{tot} - T_1 - T_2 - \frac{V_s}{a}) \\ V_s - at, & \text{if } (T_{tot} - T_1 - T_2 - \frac{V_s}{a}) < t < (T_{tot} - T_1 - T_2) \\ 0, & \text{if } t \geq (T_{tot} - T_1 - T_2) \end{cases} \tag{7.6}$$

A velocity profile like (7.6) can be easily implemented in a function using conditional statements like `if/elseif`, and could be given as setpoint to the velocity control loop of the ACOPOS. However, in this way the position control loop would be open, and there would be no certainty of the cart to have reached the desired position, because the velocity tracking error would not be compensated.

A solution to this problem is to integrate analytically (7.6) obtaining the corresponding trajectory, plotted in Figure 7.5, and then to close the position control loop with the trajectory found. If possible, equation (7.6) can be used as a feedforward velocity signal.

By integrating (7.6) the trajectory is described by

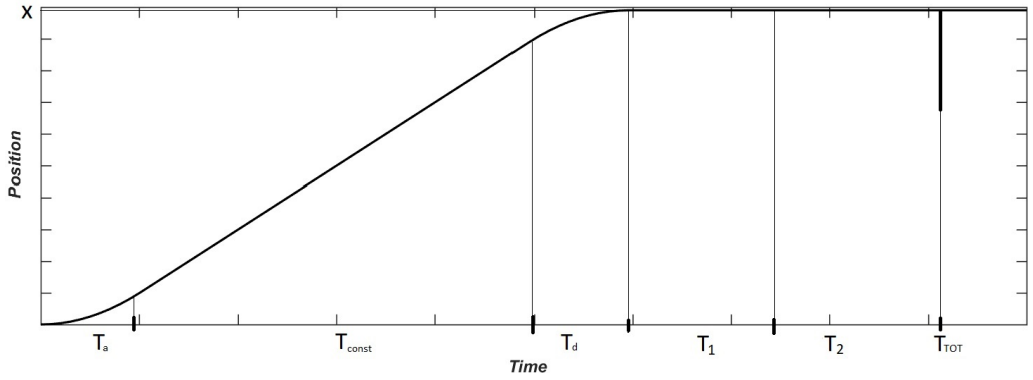

Figure 7.5: Trajectory obtained by integrating the trapezoidal velocity profile in Figure 7.4. T_1 and T_2 are the delays due to the shapers.

$$x(t) = \begin{cases} 0, & \text{if } t \leq 0 \\ \frac{1}{2}at^2, & \text{if } 0 < t \leq \frac{V_s}{a} \\ \frac{1}{2}aT_a^2 + V_s(t - T_a), & \text{if } \frac{V_s}{a} < t \leq (T_{tot} - T_1 - T_2 - \frac{V_s}{a}) \\ \frac{1}{2}aT_a^2 + V_s(T_{const}) & \text{if } (T_{tot} - T_1 - T_2 - \frac{V_s}{a}) < \\ + V_s(t - T_{const} - T_a) - \frac{1}{2}a(t - T_{const} - T_a)^2, & t < (T_{tot} - T_1 - T_2) \\ x, & \text{if } t \geq (T_{tot} - T_1 - T_2) \end{cases} \tag{7.7}$$

where $T_{const} = T_{tot} - T_1 - T_2 - 2T_a$.

The trajectory defined by (7.7) is implemented in a Function that receives the total displacement x, the acceleration value a, the total time of the movement T_{tot}, the entity of the delays caused by the shapers T_1 and T_2 and the time t and returns the value of the position corresponding to the trajectory in Figure 7.5 at time t. This function is cyclically called in `STEP_CYCLIC_POSITION_IS` and the output is given as input to a Function Block implementing one of the input shaping techniques seen, accordingly to T_1 and T_2 values setted. For the application ZV technique has been chosen, as it is the one that leads to the smallest delay, thereby allowing the set of small total time T_{tot}. The output of the first IS Function Block is set as input to the second IS Function Block, following the scheme in Figure 5.4, and the

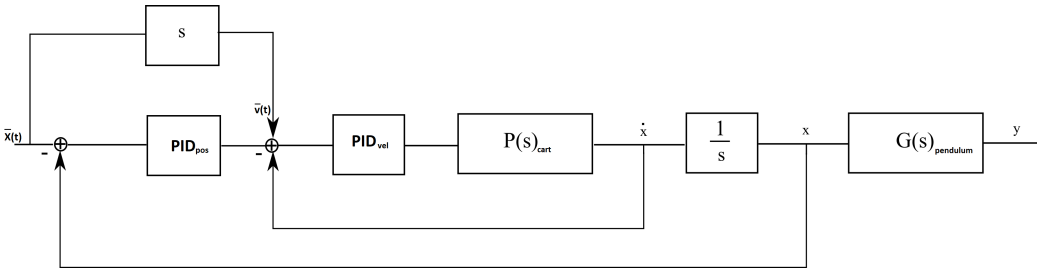

Figure 7.6: Position control scheme, with velocity feedforward signal.

output of the this second FB is set as reference trajectory to the external position control loop. By deriving the shaped output, or by using 7.6 filtered by other 2 FBs, the shaped velocity can be used as a feedforward signal for the internal velocity loop control, as shown in Figure 7.6.

7.2 Input-output inversion

The second technique implemented is the input-output inversion. As seen in Chapter 4, it consists in finding a mathematical model of the system in the form of a transfer function, defining a desired trajectory of the output and then inverting the model, in order to find the corresponding input trajectory. The dynamics inversion of the crane has already been treated in Chapter 4.2, so this section will focus on its implementation on industrial components.

In particular, the implementation will regard only the dynamics inversion of a the crane modelled with a double pendulum for a series of reasons. First, the implementation of simple pendulum input-output inversion has already been treated in [26] on the same experimental set-up. Moreover, a simple pendulum model would not be appropriate for the description of the system, because the payload has been modified with respect to the set-up used in [26] and is now distributed, therefore it cannot be approximated as a mass point. As shown in Chapter 5.6, the approximation of the system as a simple pendulum model would lead increased residual oscillations. The values of m_1, m_2 and l_2 are reported in (6.1).

As in the case of input shaping, both velocity and position control will be implemented.

7.2.1 Velocity control

In order to control the velocity of the payload, the user has to push a button on the panel, one of the two contained inside the section marked with 3 (for velocity control loop only) and 4 (for velocity control loop plus torque feedforward) in Figure 7.1, and the machine goes from state `STEP_WAIT_COMMAND` to what corresponds to `STEP_DYN_INV` in Figure 6.15. In analogy with what seen with the implementation of input shaping control, `STEP_DYN_INV` is composed by two different states, one for the acceleration and the constant velocity movement and one for deceleration.

The velocity profile of the cart is implemented inside a Function Block. It receives as input final required velocity q (in the form of the difference between initial and desired velocity), transient time τ, the parameters that define the model (m_1, m_2, l_1, l_2) and finally the time t. The polynomial (4.24) that gives the velocity of the cart at time t is calculated and returned as output.

Optionally, also the force to be applied to the cart can be calculated with (4.25). It can then converted in torque and scaled according with the transmission and given as feed forward signal to the inner torque control loop.

Every cycle time the Function Block is called inside state `STEP_DYN_INV` with a time t incremented of $0.8[ms]$, corresponding to the cycle time of the task, and the output of the function block is set as setpoint to the velocity control loop and, if available, as feedback to the inner torque control loop.

When time t exceed transient time τ, the polynomial has finished the transient, and the FB returns the final value for the velocity for every $t > \tau$.

When the button is released, the FB is called with different values for initial and final velocity, and a the polynomial is built in order to have a final velocity equal to zero. The feedforward torque signal is also calculated. An interval of time equal to τ after the button has been released, that is when the cart is still, the machine return to state `STEP_WAIT_COMMAND`.

An example of the velocity profile during a movement in velocity mode is shown in Figure 7.7.

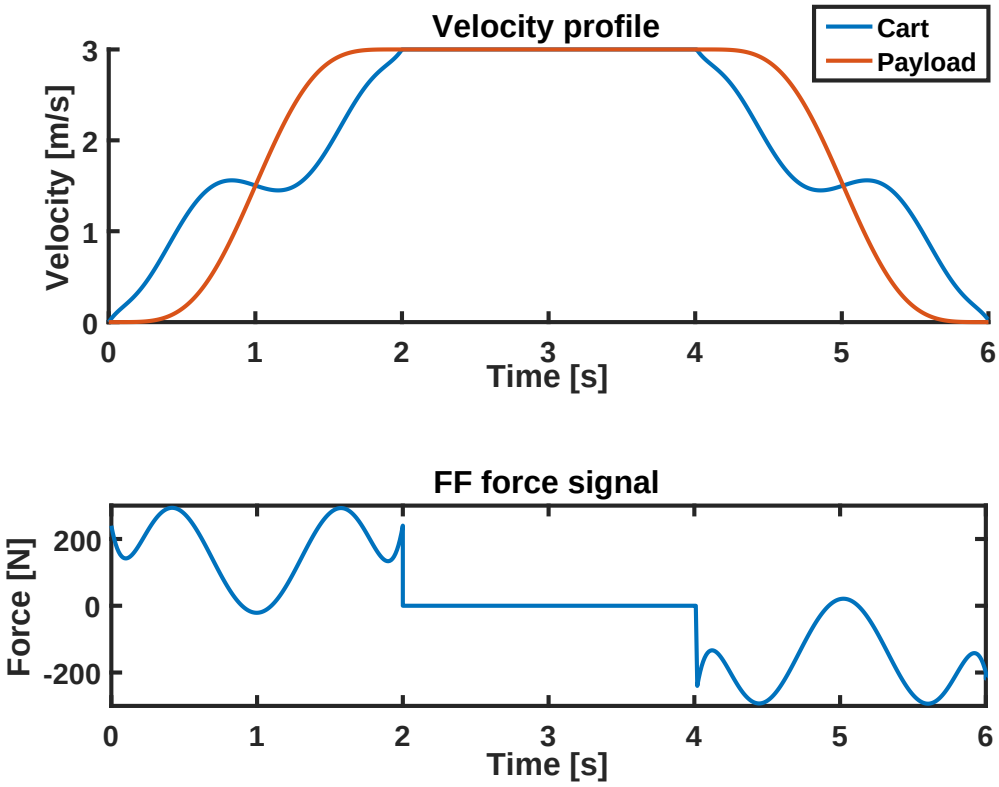

Figure 7.7: Velocity profile of the cart compared with the velocity profile of the payload. At time $t = 0$ the button is pressed, and at time $t = 2$ the operating speed is reached. At time $t = 4$ the button is released, and the payload decelerate till it reaches $v = 0$.

7.2.2 Position control

Input-output inversion technique can be exploited also in the case of position control. A setpoint position is given, along with the total time for the movement; a trajectory for the cart is found so that the payload moves from initial to final position with a polynomial trajectory and zero residual oscillation.

In section 5 of Figure 7.1 both movement time and absolute final position can be set. When the button is pushed, the machine goes from `STEP_WAIT_COMMAND` to state `STEP_DYN_INV_POS`. Here a Function Block is cyclically called, receiving as input the parameters of the model $(m_1, m_2, l_1, l_2...)$, initial and final position, total time for the movement τ, and actual time t. The Function Block returns the position and torque feedforward signal of the cart corresponding to time t. The FB is executed cyclically and time t is increased every time by the cycle time equal to 0.8 $[ms]$.

When time t exceeds τ the cart and payload have both reached the setpoint position, and the machine returns to state `STEP_WAIT_COMMAND`.

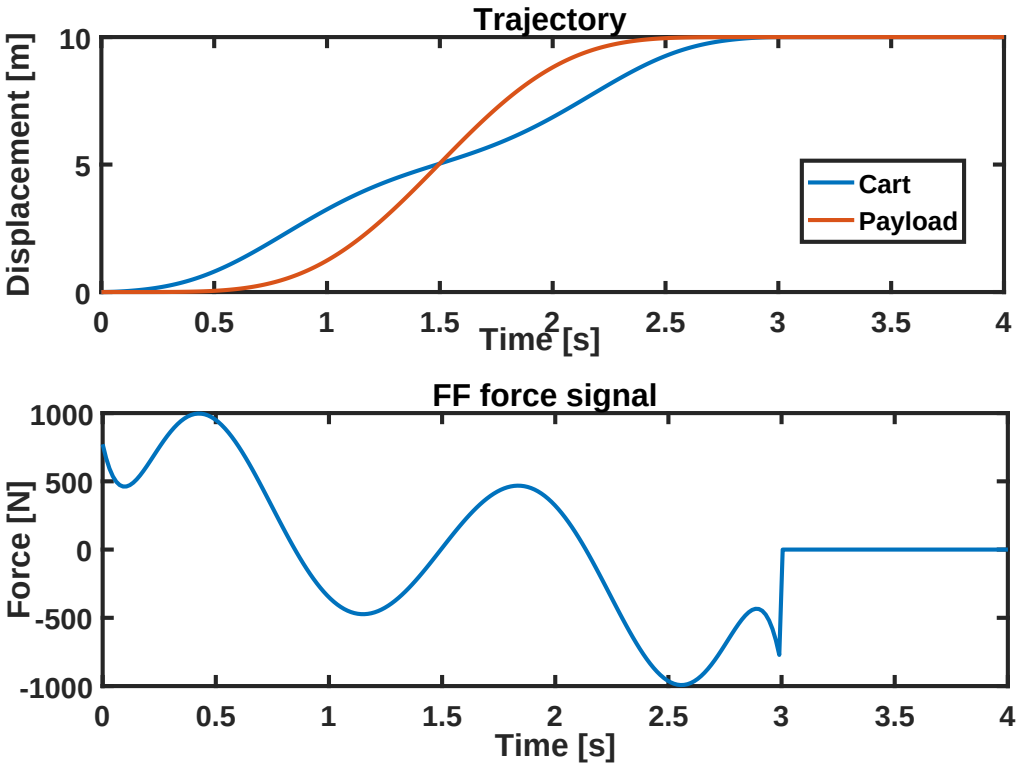

Figure 7.8: Example of trajectory of the payload and cart for a displacement of 10 meters in 3 seconds. Below, the corresponding feedforward force signal.

Chapter 8

Experimental results

In order to validate the applicability of Input-Shaping and Input-Output inversion techniques to industrial systems, the results obtained controlling the system described in Chapter 6 are here reported.

The techniques tested on the system are the input-output inversion ant the *ZV* input shaping. As reported in Chapter 7, also *ZVD*, *ZVDD*, *EI* and *EI two-hump* have been implemented on the control system, but the results are not reported as they are well represented by the results shown in Chapter 5.

Firstly, it will be shown how the measures have been taken. Secondly, Both position and velocity control will be analized by reporting the residual oscillations of the system, for both the case of distributed payload and the case of hook and payload.

8.1 Measuring system

In [26] a potentiometer has been used to collect the value of the angle θ_1 with reference to a simple pendulum model. In this thesis, which focuses in the possible advantages of the use of a double pendulum model, a simple potentiometer is not enough to fully describe the kinematic of the system. In fact, it is necessary to measure both angles θ_2 and θ_1 in Figure 2.2 to have all the information needed about the residual oscillation of the payload.

In order to do so, image processing has been used. A reflex camera has

been used to record the oscillation of the payload after a movement, along with a reference picture of the payload taken when the payload is still.

Two different markers, constituted by black painted dots, have been applied at the extremities of the payload. The reference picture and the video frames have been analized with Matlab. By binaryzing the grayscaled frames accordingly to a threshold level, the two regions of pixels corresponding to the markers have been isolated and labeled. By finding the mean of all the pixels inside the region of a marker, the center of the marker is found.

A third point corresponding to the center of rotation of angle θ_1 is calculated by extending the segment identified by the center of the two markers by a value of pixels corresponding to the number of pixel of the segment itself multiplied by the ratio of the length l_1 and l_2 in the physical system, with reference to Figure 2.2.

This third point is fixed, as the residual oscillations are measured when the cart finishes its movement.

The video recording the residual oscillation is then analized frame by frame. Once the center of the markers is found, the segments linking the two markers and the upper marker with the fixed point calculated during calibration are confronted with the segments found during calibration. Function $atan2()$ gives the values of angles θ_1 and θ_2.

In Figure 8.1 two frames are shown, one from calibration and one from the recorded oscillation.

The scripts used for image processing of the acquisitions are reported in Appendix B.

8.2 Distributed payload

For position control, the benchmark test for the techniques is a movement of 1.2 $[m]$ in a time τ. In order to show the increased performance when using one of the techniques implemented with respect of a non-controlled movement, the payload has been moved also without any kind of residual oscillation reduction technique and its oscillation measured.

For the control, both inverse dynamics and input shaping techniques have been used. In particular, the applied techniques have been used based on

(a) Frame for calibration. (b) Frame from oscillation record.

Figure 8.1: Two different frames that show 8.1a the initial calibration from a frame with steady payload and 8.1b a frame taken from a video recording the oscillation of the payload, compared with the position at the steady state (yellow line).

both simple and double pendulum model, in order to compare the differences in results and advantages of using one model or the other.

The movement has been executed for $\tau = 4$ and $\tau = 3$ seconds using input-output inversion technique, and with $\tau = 4$ $[s]$ using input shaping techniques. The reason why input shaping has not been used with $\tau = 3$ $[s]$ is that input shaping techniques require a motion time greater than the sum of the two semiperiods.

The graphs show the angle θ_1, which is a good indicator of the entity of the main vibration mode of the system, and the difference $\theta_2 - \theta_1$, which is a good indicator of the second mode, and the displacement of the second marker from the equilibrium position.

The graphs on the left side include the data from the movement without the use of anti residual oscillations techniques, while the graphs on the right shows the particular of the results using input shaping and input-output inversion techniques.

Figure 8.2 shows the residual oscillation after a movement with a transient time of $\tau = 4$ $[s]$. By the graphs on the left it can be seen that all the techniques provide much smaller residual oscillations with respect to the movement without the use of advanced control techniques.

By comparing the graphs on the right, input shaping and input-output inversion appear to be comparable in the term of residual oscillation. The input-output inversion technique based on the double pendulum model does not improve the performance with respect to the simple pendulum model based one. Regarding for input shaping techniques, the technique that explicitly takes into consideration the second frequency of the system decreases the oscillations with respect to the one that just consider the main natural frequency.

In Figure 8.3 the results for the movement of 1.2 $[m]$ with a transient time of $\tau = 3$ $[s]$ are shown. The absence of input shaping technique is due to the fact that the transient time $\tau = 3$ $[s]$ is smaller than the sum of the periods of the system, therefore input shaping cannot be implemented. The graphs show that there is an efficient reduction of the residual oscillations with respect to the uncontrolled case. Moreover, the double pendulum model case increases the performance with respect to the simple pendulum model

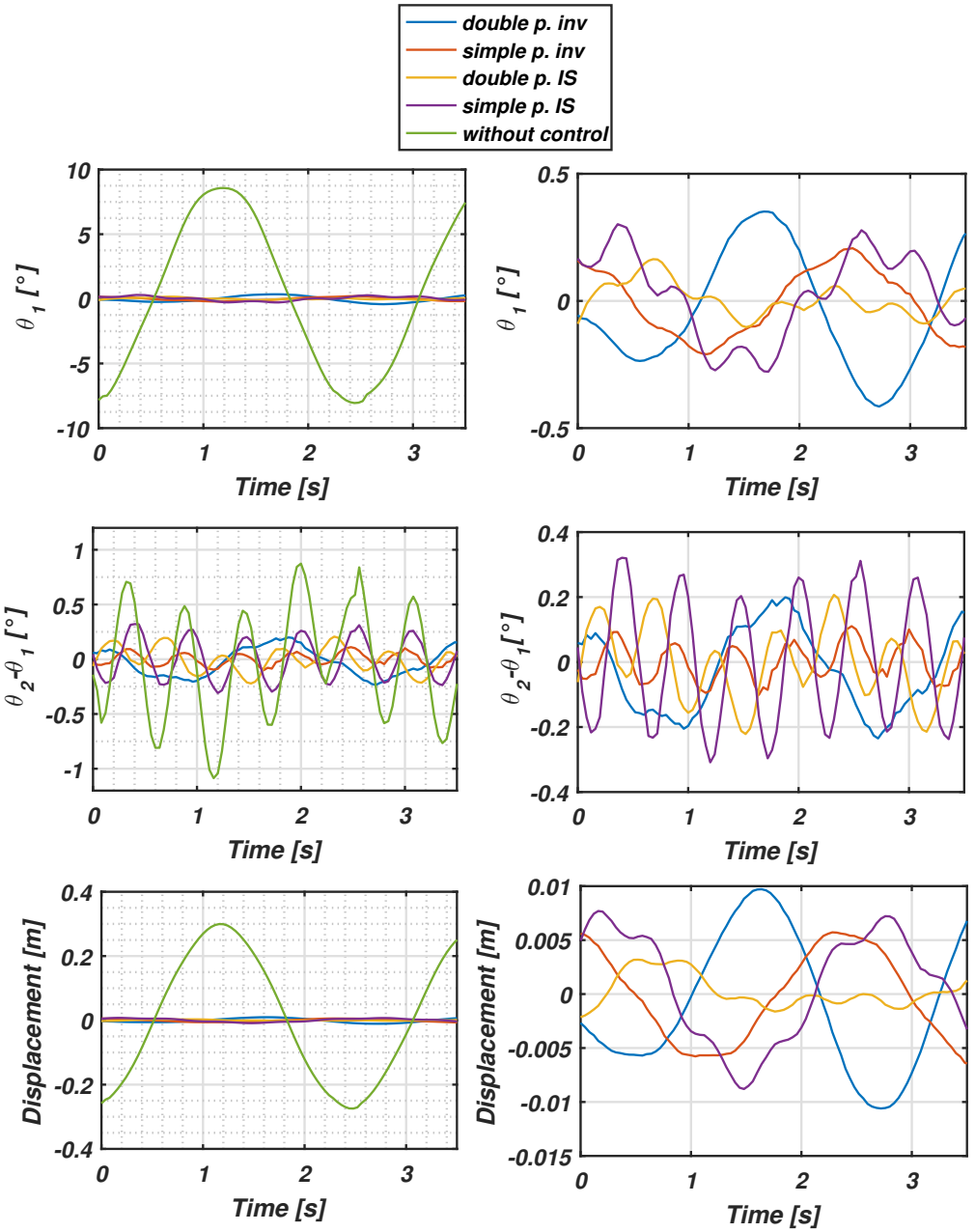

Figure 8.2: Residual oscillations after a displacement of 1.2 $[m]$ in a time of $\tau = 4\ [s]$ with the distributed payload. On the left, the results obtained with residual oscillation reduction techniques are compared with the oscillation introduced by the movement without the use of advanced techniques. On the left, the results using those techniques are compared.

based one. The increasing in performance that comes with using the double pendulum model is enhanced when the movement is rapid, as the energy is concentrated at higher frequencies and the contribute of the second way of vibrating is more significant.

For the velocity control, a movement at a velocity of $q = 500$ $[mm/s]$ is used to test the techniques. The value of the acceleration is set to $a = 3000$ $[mm/s^2]$ when using the input shaping technique, obtaining the most rapid movement possible with this setup with IS techniques, corresponding to $\tau = 1.79$ $[s]$. A input-output inversion technique allows also faster transient with respect to IS, as it does not depend on the periods of the system, a transient time of $\tau = 1.2$ $[s]$ has also been tested.

The movements are executed by bringing the velocity of the payload to the set velocity q with and without the techniques discussed in a time corresponding to τ. Then, when the set velocity has been reached, the payload is decelerated using the same technique used for the acceleration until it stops. The residual oscillations are then measured as exposed in Chapter 8.1.

It has to be noted that this is not the most efficient way of measuring residual oscillation for velocity control. In fact, after the first phase of acceleration, residual oscillations are already present on the system, and those are the oscillations that should be measured, as done in Chapter 5. The oscillations after the deceleration depends on both the oscillation introduced by acceleration and deceleration, and in particular on the phase between those two oscillations. The total residual oscillation, being a sum depending on the phase of the two oscillations introduced by velocity control transients, could be greater or smaller depending on the time the deceleration command is given. A measure with the moving cart like the one in Chapter 5 is not possible with the actual setup.

In Figure 8.4 the results for velocity control with a transient time of $\tau = 1.79$ $[s]$ are shown. From the graphs on the left it can be seen that the use of input shaping and input-output inversion techniques reduces the residual oscillation with respect to the case where no advanced technique is used. By analizing the graphs on the right the results show a reduction of the second way of oscillating with the use of the double pendulum model using input shaping with respect to the simple pendulum case, leading to a

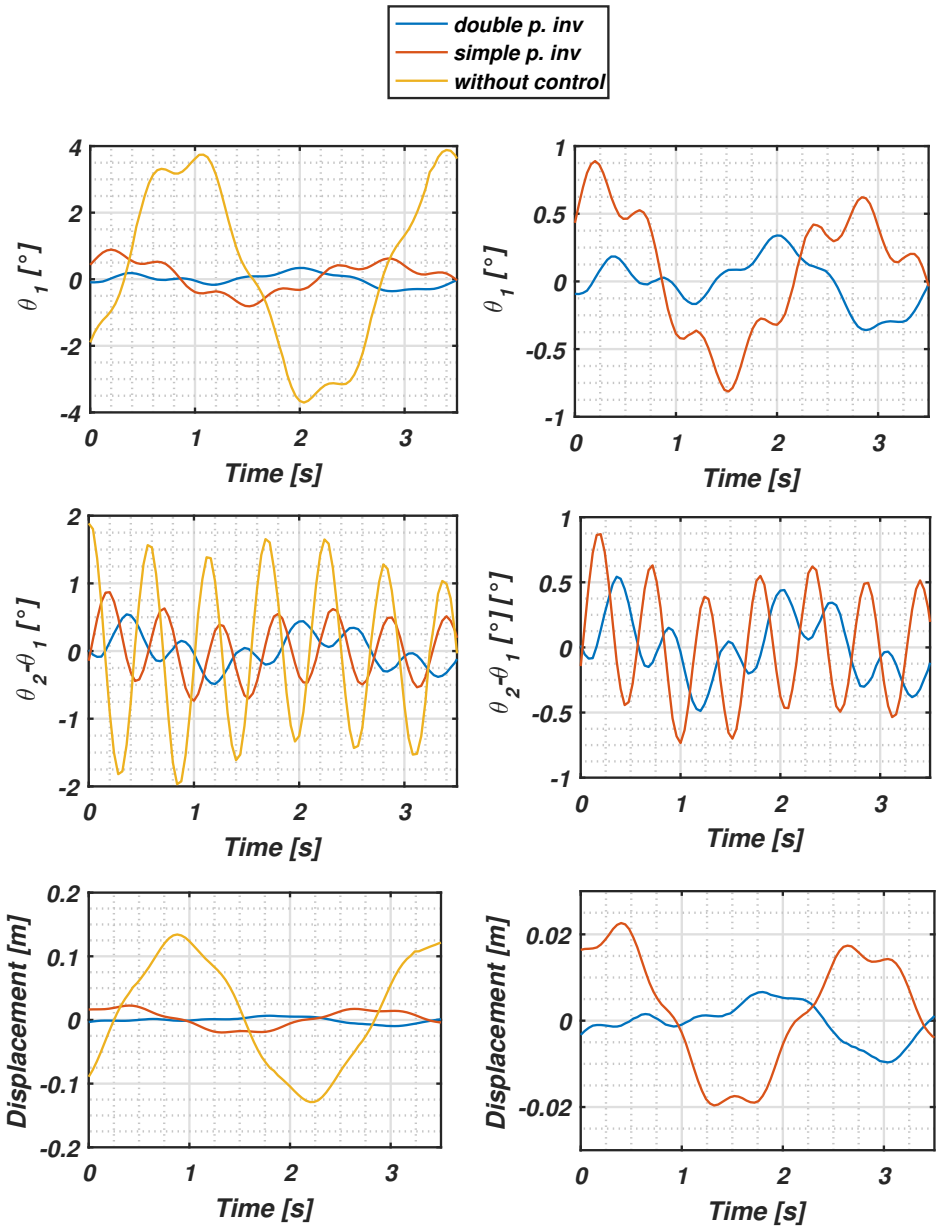

Figure 8.3: Residual oscillations after a displacement of 1.2 $[m]$ in a time of $\tau = 3\ [s]$ with the distributed payload. On the left, the results obtained with residual oscillation reduction techniques are compared with the oscillation introduced by the movement without the use of advanced techniques. On the left, the results using those techniques are compared.

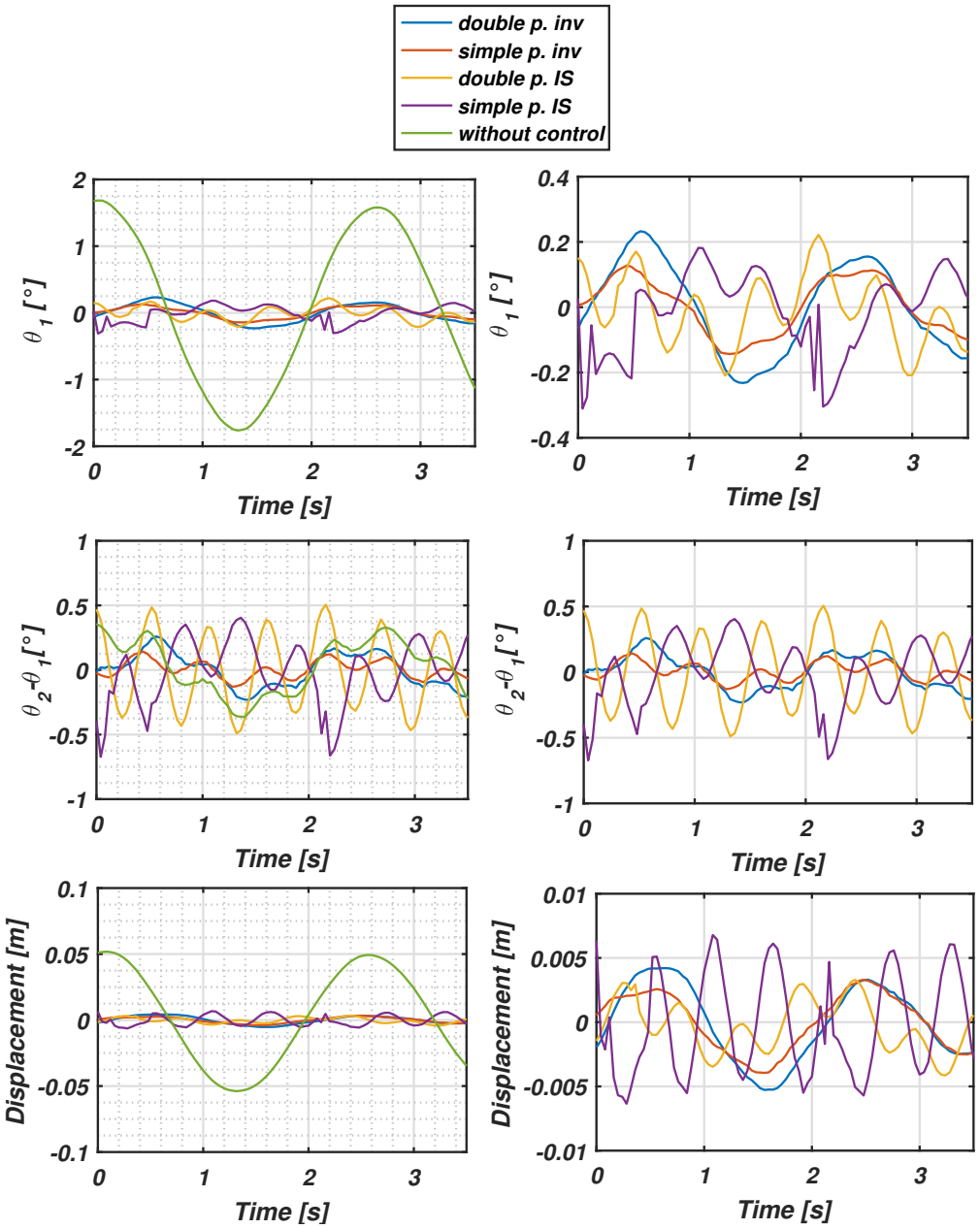

Figure 8.4: Residual oscillations after a movement at velocity $q = 500$ $[m/s]$ in a time of $\tau = 1.79$ $[s]$ with the distributed payload. On the left, the results obtained with residual oscillation reduction techniques are compared with the oscillation introduced by the movement without the use of advanced techniques. On the left, the results using those techniques are compared.

reduction of the residual oscillations. For input-output inversion, the results are comparable.

In Figure 8.5 the results for velocity control with a transient time of $\tau = 1.20$ $[s]$ are shown. For this case only input-output inversion is implementable, as the total transient time is smaller than the sum of the semiperiods of the system. As expected, residual oscillation are reduced considerably with the use of techniques discussed. The reduction of the oscillations is not as visible as in the case of $\tau = 1.79$ $[s]$, due to the fact that the faster the movement is, the greater the acceleration become, leading to bigger angles, and the approximation introduced for the linear model are less accurate. Observing the graphs on the right, the double pendulum model based input-output inversion decreases the oscillations due to the second way of vibrating, but the residual oscillations are comparable. This is due to a third way of oscillating of the crane. In fact in this test the payload oscillate around the vertical axis. Even if the oscillation of the center of mass of the payload is reduced, the position of the marker rotates around the it.

8.3 Hook and masspoint payload

Here the discussed techniques for residual oscillations reduction will be applied on the system that simulates the case of an hook of not-negligible mass and a payload that can be modelized as a masspoint. The fact that the mass of the hook used is even greater than the mass of the payload lead to an increased importance of the second way of oscillating in the residual oscillation. For this reason, the performance of double pendulum based techniques should be notably better than with the simple pendulum model ones.

In Figure 8.6 the residual oscillations after a movement of 1.2 $[m]$ with a transient time of $\tau = 4$ $[s]$ are shown. As expected, the residual oscillations are reduced when input shaping and input-output inversion are used. Moreover, from the graphs on the right, it can be seen how the use of a double pendulum model and the explicit compensation of the second way of vibrating of the system lead to enhanced performance. For both double pendulum model based IS and input-output inversion residual oscillations are considerably decreased with respect to the results in the case of the use

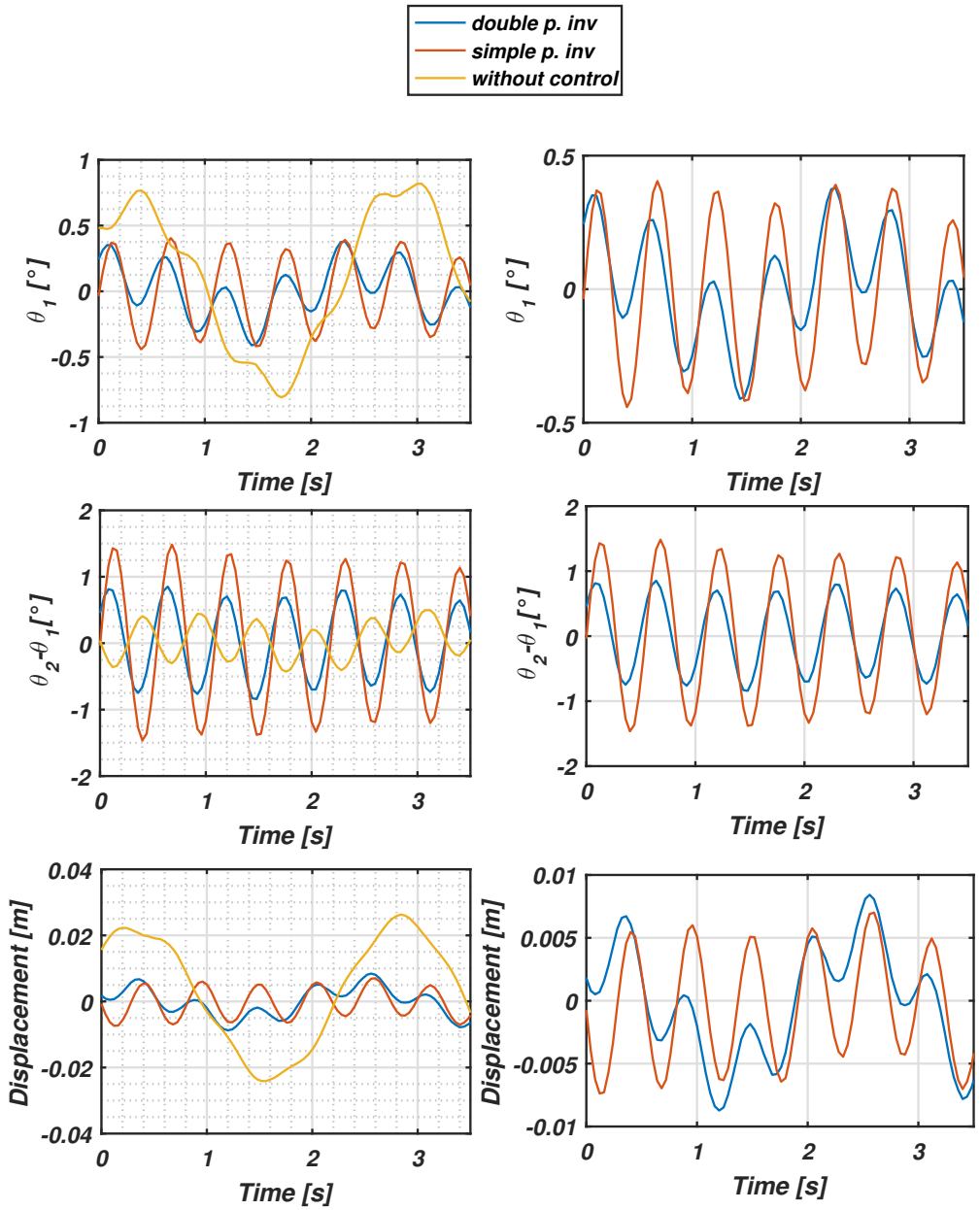

Figure 8.5: Residual oscillations after a movement at velocity $q = 500$ $[m/s]$ in a time of $\tau = 1.20$ $[s]$ with the distributed payload. On the left, the results obtained with residual oscillation reduction techniques are compared with the oscillation introduced by the movement without the use of advanced techniques. On the left, the results using those techniques are compared.

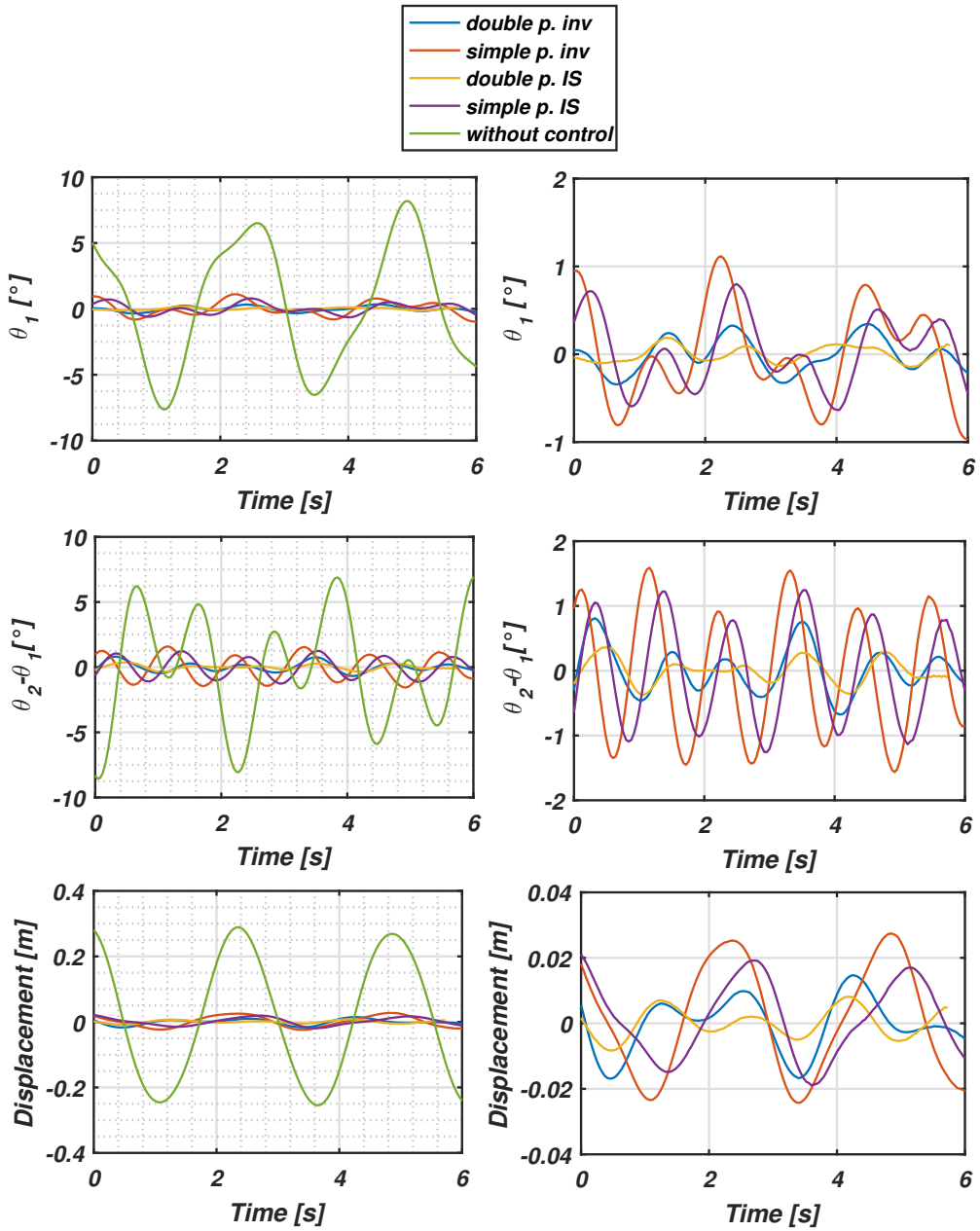

Figure 8.6: Residual oscillations after a displacement of 1.2 $[m]$ in a time of $\tau = 4$ $[s]$ with the system composed by hook and payload. On the left, the results obtained with residual oscillation reduction techniques are compared with the oscillation introduced by the movement without the use of advanced techniques. On the left, the results using those techniques are compared.

of simple pendulum models.

In Figure 8.7 the residual oscillations after a movement of 1.2 $[m]$ with a transient time of $\tau = 3$ $[s]$ are shown. The input shaping technique has not been implemented because the time τ is smaller than the sum of the two periods. As expected, the residual oscillations is reduced when using input-output inversion techniques with respect to the uncontrolled case. The graphs on the right show that the improvement in performance introduced by the use of a double pendulum model is significant.

In Figure 8.4 the results for velocity control with a transient time of $\tau = 1.81$ $[s]$ are shown. $\tau = 1.81$ $[s]$ is the minimum time for the input shaping technique to be implementable, given a set velocity of 500 $[m]$ and an acceleration of 3000 $[mm/s^2]$. From the graphs on the left it can be seen that the use of input shaping and input-output inversion techniques reduces the residual oscillation with respect to the case where no advanced technique is used. By analizing the graphs on the right, the high frequency of the system is better compensated with the double pendulum model based techniques, which have better performances in residual oscillation reduction.

In Figure 8.5 the results for velocity control with a transient time of $\tau = 1.20$ $[s]$ are shown. With $\tau = 1.20$ $[s]$ input shaping technique is no longer implementable. Again, the use of input-output inversion techniques significantly decreases the residual oscillations. By comparing the results shown on the right side graphs, the improvements using a double pendulum model are visible.

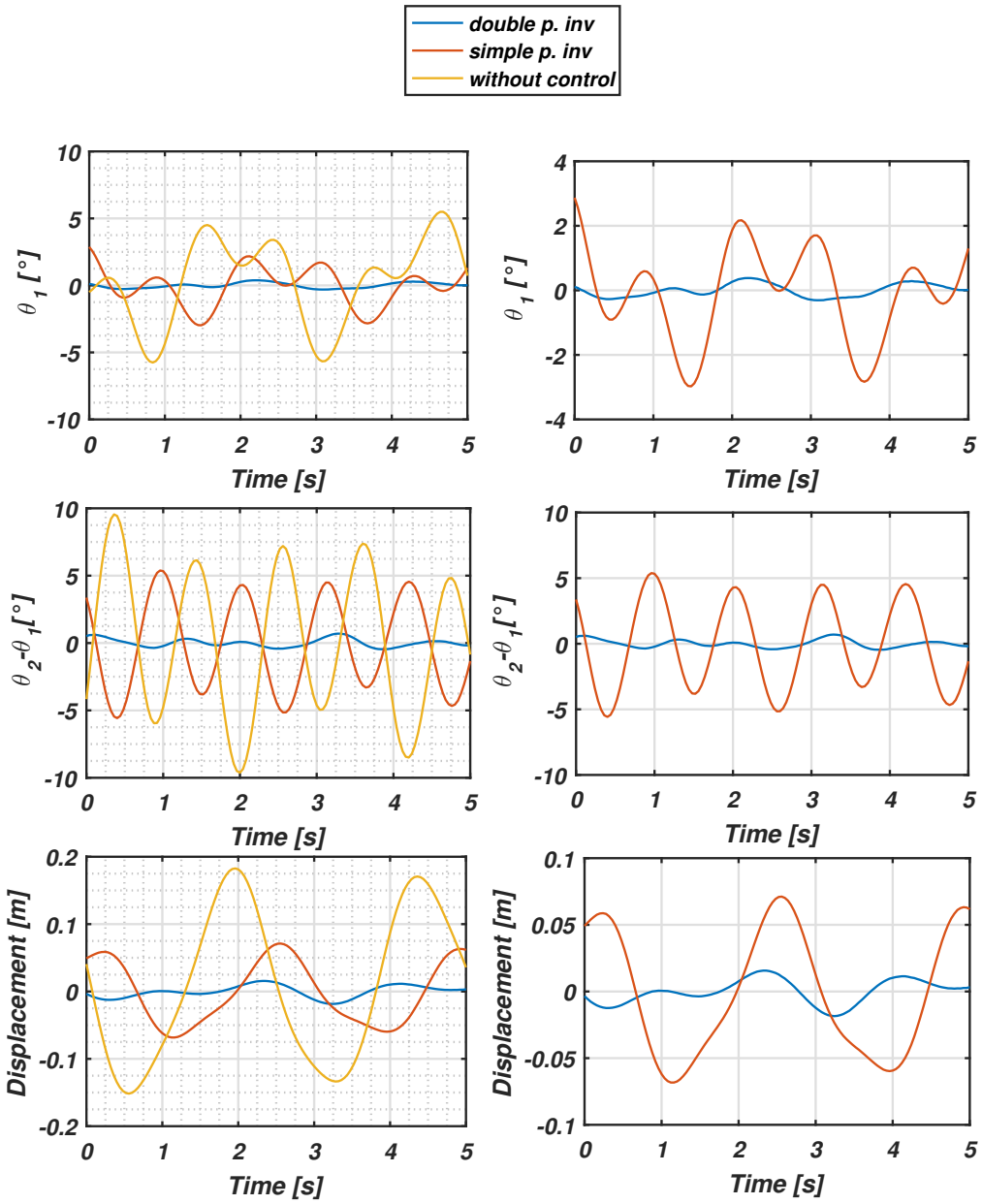

Figure 8.7: Residual oscillations after a displacement of 1.2 $[m]$ in a time of $\tau = 3$ $[s]$ with the system composed by hook and payload. On the left, the results obtained with residual oscillation reduction techniques are compared with the oscillation introduced by the movement without the use of advanced techniques. On the left, the results using those techniques are compared.

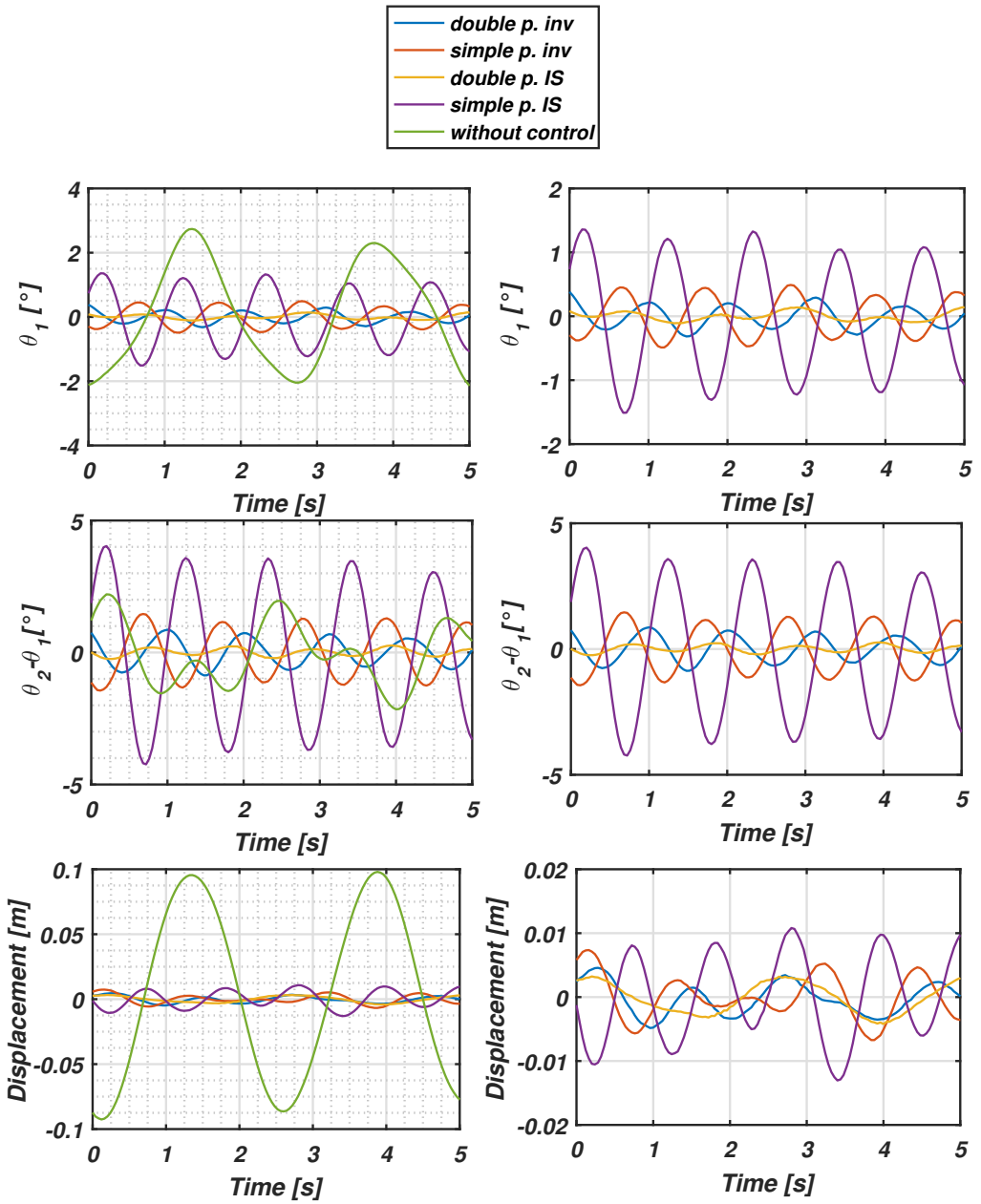

Figure 8.8: Residual oscillations after a movement at velocity $q = 500$ $[m/s]$ in a time of $\tau = 1.81$ $[s]$ with the system composed by hook and payload. On the left, the results obtained with residual oscillation reduction techniques are compared with the oscillation introduced by the movement without the use of advanced techniques. On the left, the results using those techniques are compared.

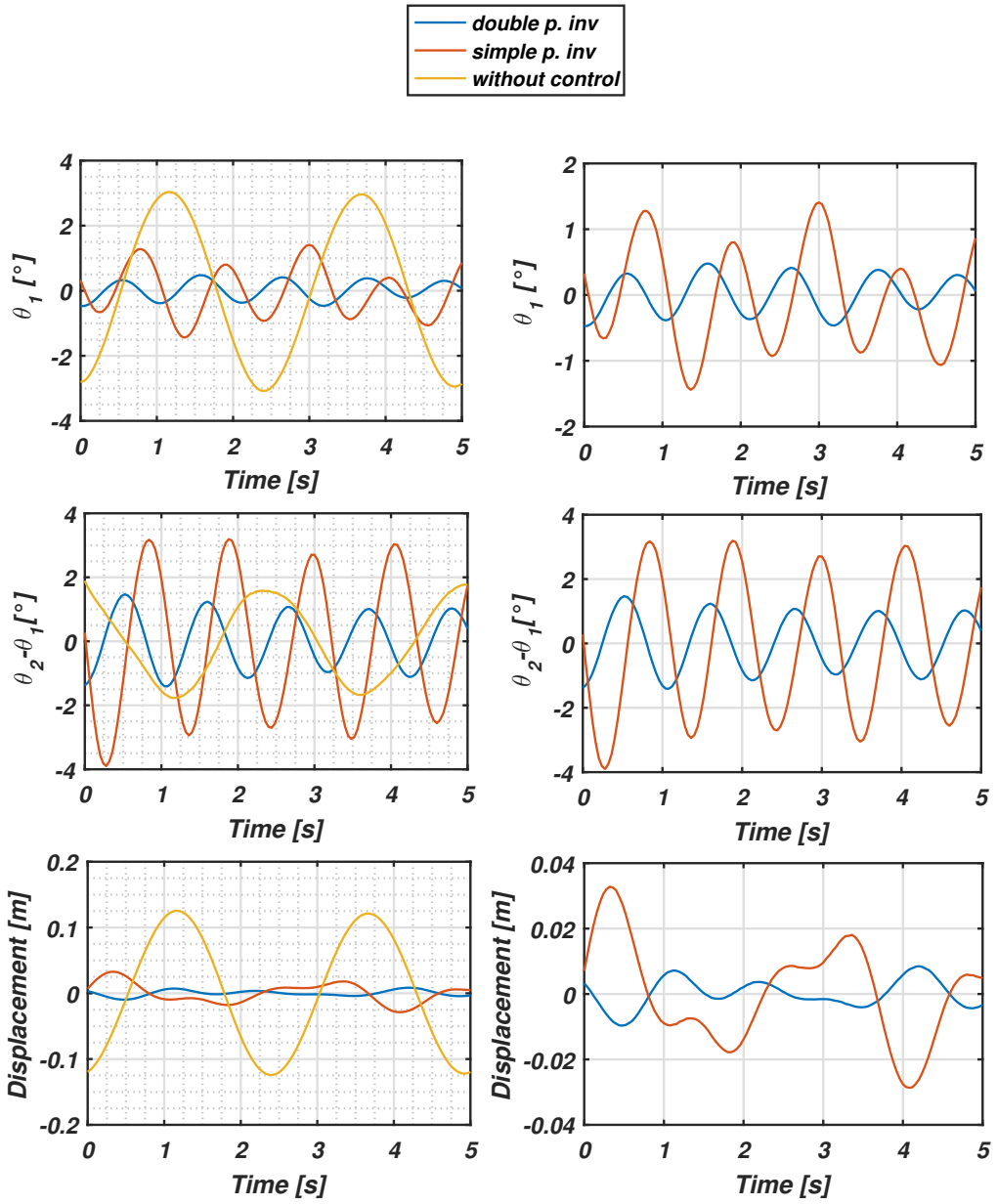

Figure 8.9: Residual oscillations after a movement at velocity $q = 500\ [m/s]$ in a time of $\tau = 1.20\ [s]$ with the system composed by hook and payload. On the left, the results obtained with residual oscillation reduction techniques are compared with the oscillation introduced by the movement without the use of advanced techniques. On the left, the results using those techniques are compared.

Conclusions

In this work the available strategies for the anti-swing control of overhead cranes have been investigated, with a particular focus on input shaping and input-output inversion techniques. Moreover, a new control strategy, consisting in the double pendulum model-based input-output inversion, and the advantages it brings in efficiently reducing residual oscillations have been investigated. The simple and double pendulum models of an overhead crane have been developed, and input shaping and input-output inversion techniques have presented. The techniques have been implemented on the models of simple and double pendulum cranes, and the robustness of the techniques has been tested by means of mathematical simulations, along with the improvement introduced with the use of the double pendulum model. The techniques developed have been implemented with off-the-shelf components in order to prove the feasibility of the use of those techniques in industrial processes. The physical system on which the techniques have been tested has been presented and modelled, and the results obtained with the use of different techniques are compared in the graphs of Chapter 8. In this chapter a brief comparison between the two open-loop techniques used is exposed and enriched by the results obtained. The improvements due to the use of a more complex model are also addressed. Finally, future possible developments of the project are presented.

Input shaping and input-output inversion are two of the most promising techniques for the open-loop control of overhead cranes. The other open-loop that has been presented in Chapter , that is optimal control, is rarely used, due to its computational requirements and the difficulty to set *a priori* the weights of the cost function. The strong advantage of input shaping techniques is represented by the simplicity of its implementation in industrial

off-the-shelf components and by the basic model required, that is nominally the knowledge of natural frequencies and damping ratios. While input shaping is by far the most widely diffused in the industrial field, it still presents some insurmountable limitations. The use of input shaping introduces a delay in the command signal that depends on the period of the system. In particular, as reported in Chapter 3, ZV techniques introduce a delay of half the period of the system, while more robust techniques like ZVD, ZVDD, and EI introduce delays up to one period and a half. This delay represents a serious issue in the anti-swing control of overhead cranes, in particular for small displacements where the operator cannot wait for a period of the system (that can easily be in the order of seconds for industrial overhead cranes) to see the results of its actions. Input-output inversion, on the other side, does not have limits on the transient time τ. Moreover, limits can be added in order to minimize motion time τ under the respect of actuators limits [23].

With this work, the validity of input-output inversion as an efficient technique for anti-swing control of overhead cranes has been proven. The comparison between the robustness of input shaping and input-output inversion techniques shows that input-output inversion has the same robustness of ZV techniques when the motion time of the two techniques are set to be equal, with the advantage that input-output inversion τ can be easily increased, obtaining an increased robustness, almost comparable to robust input shaping techniques. Moreover the transient time τ can also be decreased under the limits of input shaping, providing the possibility to obtain a more aggressive control technique.

With the possibility of choosing the aggressiveness of the control by changing a single parameter, input-output inversion is a valid alternative to input shaping for the control of the crane.

Moreover, it has been shown that both input shaping and input-output inversion techniques can be implemented in off-the-shelf industrial components. The disadvantage of the input-output inversion technique, that is the complexity of modelling the system, has been overcome by presenting the mathematical model and obtaining a single polynomial function that describe the trajectory of the cart with system parameters that can be easily measured (lengths of the cables, masses of payload and hooks and damp-

enings). In particular these functions are: (4.16) for velocity control of the simple pendulum crane, (4.20) for the position control of the simple pendulum crane, (4.24) for the velocity control of the double pendulum crane and (4.28) for the position control of the double pendulum crane.

The effectiveness of the techniques presented has been proven by means of both simulations and physical experiments. In particular, the use of the presented techniques has been shown to be effective in the reduction of residual oscillations in all the cases. By comparing the results obtained in Chapter 8, the use of a double pendulum model has been advantageous particularly in the case of the presence of a prevalent mass positioned in the hook, and it has been more efficient in the cases of rapid movements (see Figure 8.7). The use of the double pendulum model is therefore justified particularly in the case of rapid movements with small payloads. In all the other cases the small improvements in performance could not justify the use of a more complex model, and particularly in the case of input shaping, where the presence of a second natural period increase the delay introduced in the control signal.

Even if the techniques tested with this thesis have proved to be effective, some problems remain unsolved.

One of the main characteristic of an industrial crane is the ability of hoisting the payload, ability that is very important in particular in the case of clustered workspaces, where the hoisting is used to avoid obstacles along the path. The open-loop techniques tested in this thesis are based on a model of the crane with a fixed length of the hoisting cable. Being open-loop techniques, the hoisting of the payload during the trajectory would lead to residual oscillations. Depending on the velocity of the hoisting and on the motion time, a solution is to use ZVD, ZVDD or EI techniques, that have been shown to be very robust with respect to changes in the length of the cable (see the figures in Chapter 5). In some cases, more robust techniques could not be implementable or sufficiently efficient, because more robustness also means increased motion times and therefore increased operative costs.

A future development of this thesis could be the study of a time-variant model of the crane, where the parameter l_1 is considered as a function of time. Once the model has been obtained, following the guidelines of the input-output inversion, a techniques should be developed to permit the hoisting of

the payload during the trajectory.

Another possible extension of this thesis is the implementation of closed-loop techniques. As presented in Chapter , many closed-lopp techniques have peen proposed in literature for the anti-swing control of overhead cranes. Closed-loop techniques are more robust to changes in model parameters with respect to open-loop ones, and the hoisting of the payload can be explicitly taken into account (e.g. with a gain-scheduling approach). The reason why closed-loop techniques are not the standard for the control of overhead cranes is the lack of sensors for the feedback of the states (position of the payload, or oscillation angle) in industrial off-the-shelf overhead cranes.

A future, possible study is the integration between image processing and feedback control techniques. In this thesis, image processing has been used only to get the oscillations data from the experiments. The increasing computational power of CPUs has made possible the real-time processing of frames, that means that information from cameras can now provide a feedback to systems with relatively fast dynamics. In the last years a growing interest has born in the field of vision feedback control of overhead cranes [12].

Appendices

Appendix A

Dynamic Inversion Script

The script used for the inversion of double pendulum dynamics in the case of position control is reported here. The script can be easily changed in order to use it for velocity control.

```
%% Script for dynamic inversion
q_r=10;          %Total displacemente
tau_r=5;         %Total time for the movemend
syms m1 m2 g mC l1 l2 Cc C1 C2 s real

Matrici_SS_con_smorzamento %building A and B, SS matrices of the
    system
C=[1 0 0 0 0 0; 0 0 1 0 0 0; 0 0 0 0 1 0];
I=eye(6);
transfer=C*inv(I*s-A)*B;
X2_U=simplify(transfer(1)+transfer(2)*l1+transfer(3)*l2); %TF
   between
% force applied to the cart and position of the payload

%% TF between force applied to the cart and its velocity.
C=[0 1 0 0 0 0];
Vc_U=simplify(C*inv(I*s-A)*B);

%% TF between position of the cart and position of the payload
G=simplify(X2_U*inv(Vc_U)*s);
[N,D]=numden(G);
N=collect(N,'s');
```

```
N=coeffs(N,s,'all');
G=simplify(N(end)/D);
G_inv=collect(inv(G),s);

%%  m2 symbolic polynomial trajectory
n=5;
syms t tau q real
aux=0;
for r=0:n
    aux=aux+((-1)^(n-r)*tau^r*t^(2*n-r+1)/...
        (factorial(r)*factorial(n-r)*(2*n-r+1)));
end
x_2= q*factorial(2*n+1)/(factorial(n)*tau^(2*n+1))*aux;
x_2=collect(x_2,t);

%% derivatives of order alpha of the trajectoy
syms alpha real
aux=0;
for r=0:n
    aux=aux+((-1)^(n-r)*tau^r*t^(2*n-r+1-alpha)*factorial(2*n-r
       +1)...
        /(factorial(r)*factorial(n-r)*(2*n-r+1)*factorial(2*n-r
           +1-alpha)));
end
deriv_x_2=q*factorial(2*n+1)/(factorial(n)*tau^(2*n+1))*aux;

%% polynomial of cart position after inversion
coeff_inv=coeffs(G_inv,s,'all');
derivative_order=length(coeff_inv)-1:-1:0;
derivatives_vector=subs(deriv_x_2,alpha,derivative_order);
x_c=simplify(sum(coeff_inv.*derivatives_vector)); % parametric
   cart position

%% Substitution of model's paramenters inside symbolic cart
   trajectory
dati_sistema;                   % defining the parameters of the
    model
t_r=linspace(0,tau_r,200);
x_c=subs(x_c,[m1 m2 l1 l2 mC g q tau Cc C1 C2],...
    [m1_r m2_r l1_r l2_r mC_r g_r q_r tau_r Cc_r C1_r C2_r]);
x_c=subs(x_c,t,t_r);
```

```
x_c=double(x_c);
t_r=linspace(0,3*tau_r,600);
x_c=[t_r;x_c q_r*ones(1,400)]'; % explicit cart trajectory

%% Substitution of model's paramenters inside symbolic payload
   trajectory
t_r=linspace(0,tau_r,200);
x_2=subs(x_2,[m1 m2 l1 l2 mC g q tau],...
    [m1_r m2_r l1_r l2_r mC_r g_r q_r tau_r]);
x_2=subs(x_2,t,t_r);
x_2=double(x_2);
t_r=linspace(0,3*tau_r,600);
x_2=[t_r;x_2 q_r*ones(1,200) q_r*ones(1,200)]';

%% Inversion between payload trajectory and force for
   feedforward
[N,D]=numden(X2_U);
N=collect(N,'s');
N=coeffs(N,s,'all');
X2_U=simplify(N(end)/D);
X2_U_inv=collect(inv(X2_U),s);

coeff_inv=coeffs(X2_U_inv,s,'all');
derivative_order=length(coeff_inv)-1:-1:0;
derivatives_vector=subs(deriv_x_2,alpha,derivative_order);

U_FF=simplify(sum(coeff_inv.*derivatives_vector));  %
   feedforward force

%% Substitution of model's paramenters inside symbolic force
   signal
t_r=linspace(0,tau_r,200);
U_FF=subs(U_FF,[m1 m2 l1 l2 mC g q tau Cc C1 C2],...
    [m1_r m2_r l1_r l2_r mC_r g_r q_r tau_r Cc_r C1_r C2_r]);
U_FF=subs(U_FF,t,t_r);
U_FF=double(U_FF);
t_r=linspace(0,3*tau_r,600);
U_FF=[t_r; U_FF zeros(1,400)]';     %explicit force feedforward
   signal
```

Appendix B

Image processing for experimental results

In order to calculate angles θ_1 and θ_2 image processing has been used, as reported in Chapter 8.1.

B.1 process_oscillations(filename_calib, filename_data)

The main function is *process_oscillations(filename_calib, filename_data)*. It receives the location of the videos for calibration and with the actual oscillations. It has a first part of calibration, where the fixed point corresponding to the position of the cart is also found. Then the data video is analized, and for every frame the markers are found and the angles calculated.

```
1  function []=process_oscillations(filename_calib, filename_data)
2  close all
3  clc
4  warning off
5
6  vlimits=[1 1080];
7  hlimits=[1 1920];
8  n_punti=2;
9  soglia_livello_bw=0.07;
10 i=1;
11
```

```
12 %% CALIBRATION
13 v_calib=VideoReader(strcat(filename_calib,'.MOV'));
14 v_calib.CurrentTime=v_calib.Duration/2;
15 A=readFrame(v_calib);
16 %FINDING MARKERS
17 points=find_npoints(A,vlimits,hlimits,n_punti,soglia_livello_bw)
18 points_calib=points;
19 %SHOWING IMAGE
20 A=rgb2gray(A);
21 A=insertMarker(A,round(points(:,:)),'circle','size',19);
22 A=insertShape(A,'Line',round([points(1,:),points(2,:)]),'
       LineWidth',5);
23 imshow(permute(A,[2,1,3]));
24 pause(0.001)
25 %% FINDING FIXED POINT
26 distance=1180/790;
27 fixed_point=points(1,:)+(points(1,:)-points(2,:))*distance;
28 verticale=fixed_point-points(1,:);
29
30 %% Analizing data video
31 v = VideoReader(strcat(filename_data,'.MOV'));
32 load(strcat(filename_data,'_init'));
33 v.CurrentTime=init_time;
34 while hasFrame(v)
35     video(:,:,:,i) = readFrame(v);
36     frame_time(i)=v.CurrentTime;
37     i=i+1
38 end
39 i=1;
40 for i=1:length(frame_time)
41 %while frame_time(i)<=5.56
42     aux=video(:,:,:,i);
43     points(:,:)=find_npoints(aux,vlimits,hlimits,n_punti,
           soglia_livello_bw);
44
45     A=video(:,:,:,i);
46     A=insertMarker(A,round(points(:,:)),'circle','size',19,'
           color','r');
47     A=insertShape(A,'Line',round([points(1,:),points(2,:)]),'
           LineWidth',5,'color','r');
48     imshow(permute(A,[2,1,3]));
```

```
49
50      % finding angles
51      a=fixed_point-points(1,:);
52      x1=a(1);
53      y1=a(2);
54      b=points(1,:)-points(2,:);
55      x2=b(1);
56      y2=b(2);
57
58      angle_1(i) = wrapTo360(atan2d(a(1)*verticale(2)-a(2)*
            verticale(1),a(1)*verticale(1)+a(2)*verticale(2)));
59      angle_2(i) = wrapTo360(atan2d(b(1)*verticale(2)-b(2)*
            verticale(1),b(1)*verticale(1)+b(2)*verticale(2)));
60
61      % angle conditioning to have continuous signals
62      if angle_1(i)>180
63          angle_1(i)=angle_1(i)-360;
64      end
65
66      if angle_2(i)>300
67          angle_2(i)=angle_2(i)-360;
68      end
69
70       if angle_2(i)>150
71          angle_2(i)=angle_2(i)-180;
72      end
73
74      pause(0.001)
75
76  end
77
78  save(strcat(filename_data,'_angoli'),'angle_1','angle_2','
        frame_time')
79  end
```

B.2 find_npoints(A,vlimits,hlimits,n_poits,threshold)

process_oscillations(filename_calib, filename_data) uses function *find_npoints(A,vlimits,hlimits,n_poits,threshold)* to find the center of the

markers. This function convert to black&white a region of the picture A determined by the limits *vlimits* and *hlimits* accordingly to a threshold. Then it labels all the regions of connected points, isolates the n largest ones (two in the case of two markers) and calculate the center of those regions.

```
1  function [punti] = find_npoints(A,vlimits,hlimits,n_poits,
       threshold)
2   h1=vlimits(1);
3   h2=vlimits(2);
4   w1=hlimits(1);
5   w2=hlimits(2);
6
7   % transform the desired region of the frame in B&W with a
       treshold and filling holes
8   Abw=im2bw(A(h1:h2,w1:w2,:), threshold);
9   Abw=imcomplement(Abw);
10  Abw= imfill(Abw,'holes');
11
12  % find all teh connected regions of points
13  [L,n]= bwlabel(Abw,8);
14
15  % get only the n largest regions
16  vect=zeros(n,2);
17  for m=1:n
18     vect(m,1)=length(find(L==m));
19     vect(m,2)=m;
20  end
21
22  [values, order] = sort(vect(:,1),'descend');
23  vect = vect(order,:);
24  %fin the center of the regions
25            for l=1:n_poits
26
27                [r,c]=find(L==vect(l,2));
28                r=mean(r);
29                c=mean(c);
30                punti(l,:)=[c+hlimits(1)-1,r+vlimits(1)-1];
31            end
32  end
```

Bibliography

[1] `https://www.br-automation.com`, accessed: 2017-08-25.

[2] E. M. Abdel-Rahman, A. H. Nayfeh, and Z. N. Masoud. Dynamics and control of cranes: A review. *Modal Analysis*, 9(7):863–908, 2003.

[3] J. Ackermann. Parameter space design of robust control systems. *IEEE Transactions on Automatic Control*, 25(6):1058–1072, 1980.

[4] A. Al-Garni, K. Moustafa, and S. J. Nizami. Optimal control of overhead cranes. *Control Engineering Practice*, 3(9):1277–1284, 1995.

[5] J. W. Beeston. Closed-loop time optimatial control of a suspended payload-a design study. In *Proc. 4th IFAC World Congress*, pages 85–99, 1969.

[6] J. Calvert and D. Gimpel. Method and apparatus for control of system output in response to system input. 1957. US Patent 2,801,351.

[7] S. Cappa. Progettazione e controllo di un sistema a carroponte con due gradi di libertà. Master's thesis, Università degli Studi di Brescia, 2017.

[8] J. A. Field. The optimization of the performance of an ore bridge. *Transactions of the Engineering Institute of Canada*, 5(3):163–169, 1961.

[9] H. Goldstein, C. Poole, and J. Safko. *Classical Mechanics*. Addison-Wesley, jun 2001.

[10] S. Gurleyuk, O. Bahadir, Y. Turkkan, and H. Usenti. Improved three-step input shaping control of crane system. *WTOS*, 7(6):652–661, June 2008.

[11] C. Huygens. *Horologium oscillatorium: sive de motu pendulorum ad horologia aptato demonstrationes geometricae*. F. Muguet, 1966.

[12] P. Hyla. The crane control systems: A survey. In *Methods and Models in Automation and Robotics (MMAR), 2012 17th International Conference on*, pages 505–509. IEEE, 2012.

[13] B. Käpernick and K. Graichen. Model predictive control of an overhead crane using constraint substitution. In *American Control Conference (ACC), 2013*, pages 3973–3978. IEEE, 2013.

[14] G. Lallement and D. J. Inman. A tutorial on complex eigenvalues. page 490–495, 1995. Nashville, TN.

[15] H. Lee, S. Cho, and J. Cho. A new anti-swing control of overhead cranes. *IFAC Proceedings Volumes*, 30(13):115–120, 1997.

[16] G. Marro. *Controlli automatici*. Zanichelli, 1978.

[17] A. Marttinen. Pole-placement control of a pilot gantry. In *American Control Conference, 1989*, pages 2824–2826. IEEE, 1989.

[18] E. Ohnishi, I. Tsuboi, T. Egusa, and M. Uesugi. Automatic control of an overhead crane. *IFAC Proceedings Volumes*, 14(2):1885–1890, 1981.

[19] H. Oshima, S. Yasunobu, and S. Sekino. Automatic train operation system based on predictive fuzzy control. In *Artificial Intelligence for Industrial Applications, 1988. IEEE AI'88., Proceedings of the International Workshop on*, pages 485–489. IEEE, 1988.

[20] F. Padula, A. Visioli, D. Facchinetti, and A. Saleri. A dynamic inversion approach for oscillation-free control of overhead cranes. In *IEEE International Conference on Emerging Technologies and Factory Automation*, Luxembourg, 2015. IEEE.

[21] A. Piazzi and A. Visioli. Minimum-time system-inversion-based motion planning for residual vibration reduction. *IEEE/ASME transactions on mechatronics*, 5(1):12–22, 2000.

[22] A. Piazzi and A. Visioli. Optimal noncausal set-point regulation of scalar systems. *Automatica*, 37(1):121 – 127, 2001.

[23] A. Piazzi and A. Visioli. Optimal dynamic-inversion-based control of an overhead crane. *IEE Proceedings-Control Theory and Applications*, 149(5):405–411, 2002.

[24] D. Qian and J. Yi. *Hierarchical sliding control for under-actuated cranes*. Springer, 2015.

[25] D. Qian and J. Yi. *Hierarchical Sliding Mode Control for Under-actuated Cranes*. Springer-Verlag Berlin Heidelberg, 2015.

[26] A. Saleri and D. Facchinetti. Progettazione meccatronico di un sistema di movimentazione carichi. Master's thesis, Università degli Studi di Brescia, 2014.

[27] R. Salminen, A. Marttinen, and J. Virkkunen. Adaptive pole placement control of a pilot crane. *IFAC Proceedings Volumes*, 23(8):313–318, 1990.

[28] D. Schindele and H. Aschemann. Fast nonlinear mpc for an overhead travelling crane. *IFAC Proceedings Volumes*, 44(1):7963–7968, 2011.

[29] N. C. Singer and W. P. Seering. Preshaping command inputs to reduce system vibration. *Journal of Dynamic Systems, Measurement, and Control*, 112(1):76–82, March 1990.

[30] W. E. Singhose, D. Kim, and M. Kenison. Input shaping control of double-pendulum bridge crane oscillations. *Journal of Dynamic Systems, Measurement, and Control*, 130(3):034504, 2008.

[31] W. E. Singhose, W. P. Seering, and N. C. Singer. Shaping inputs to reduce vibration: a vector diagram approach. In *Proceedings., IEEE International Conference on Robotics and Automation*, pages 922–927 vol.2, May 1990.

[32] O. Smith. Posicast control of damped oscillatory systems. *Proceedings of the IRE*, 45(9):1249–1255, Sept 1957.

[33] J. Vaughan, A. Yano, and W. E. Singhose. Comparison of robust input shapers. *Journal of Sound and Vibration*, 315(4–5):797 – 815, 2008.

[34] J. M. Virkkunen and A. T. Marttinen. Computer control of a loading bridge. In *Control, 1988. CONTROL 88., International Conference on*, pages 484–488. IET, 1988.

[35] M. Vukov, W. Van Loock, B. Houska, H. J. Ferreau, J. Swevers, and M. Diehl. Experimental validation of nonlinear mpc on an overhead crane using automatic code generation. In *American Control Conference (ACC), 2012*, pages 6264–6269. IEEE, 2012.

[36] S. Yasunobu and T. Hasegawa. Evaluation of an automatic container crane operation system based on predictive fuzzy control. *Control-theory and advanced technology*, 2(3):419–432, 1986.

[37] S. Yasunobu and T. Hasegawa. Predictive fuzzy control and its application for automatic container crane operation system. In *Proc. 2nd. IFSA Congress, Tokyo, Japan, Julie*, 1987.

UNIVERSIDAD DE ALMERÍA

Resumen/Abstract

One of the main problem when facing motion control, and in control in general, is the presence of undesired oscillations. These oscillations, which characterize every mechanical system, leads to problems like error in positioning and difficulty in controlling the sway.
In this thesis, the problem of oscillations is addressed using a very diffused industrial system for which oscillations are the leading problem: the overhead crane.
This system, presenting the same configuration of a pendulum, is characterized by oscillations with very low damping ratios. The presence of this persistent oscillation during and after the movement makes difficult the manual control, decreases the accuracy and increases the overall positioning time. Moreover, considering the fact that most of the payloads moved by gantry cranes are heavy, a safety hazard is posed by payload oscillation, in particular in cluttered workspaces.
Various advanced control techniques have been proposed to reduce the presence of residual oscillations on industrial cranes, and most of them can be applied to general oscillating systems.
The aim of this thesis is to devise new techniques and to discuss their applicability with industrial off-the-shelf components, focusing in particular on input-output inversion-based techniques and comparing them with the well known input-shaping ones, also investigating their applicability in industrial processes. The importance of an accurate model is also addressed, comparing the results obtained with a simple pendulum model of the overhead crane and with a more complex double pendulum model.
The technique of dynamic inversion for industrial crane based on a double pendulum model is here presented for the first time.